LABORATORY AND NUMERICAL INVESTIGATION OF INTERFACE DEBONDING OF BONDED CONCRETE OVERLAY OF ASPHALT AND ITS EFFECT ON THE CRITICAL STRESS IN THE OVERLAY

by

Feng Mu

BS, Tsinghua University, 2004

MPhil, The University of Hong Kong, 2007

Submitted to the Graduate Faculty of

Swanson School of Engineering in partial fulfillment

of the requirements for the degree of

Doctor of Philosophy

University of Pittsburgh

2014

UNIVERSITY OF PITTSBURGH

SWANSON SCHOOL OF ENGINEERING

This dissertation was presented

by

Feng Mu

It was defended on

December 9, 2013

and approved by

Donald J. Janssen, PhD, Associate Professor, Department of Civil and Environmental

Engineering, University of Washington

Jeen-Shang Lin, ScD, Associate Professor, Department of Civil and Environmental

Engineering, University of Pittsburgh

John C. Brigham, PhD, Assistant Professor, Department of Civil and Environmental

Engineering and Bioengineering, University of Pittsburgh

Dissertation Director: Julie M. Vandenbossche, Assistant Professor, Department of Civil and

Environmental Engineering, University of Pittsburgh

LABORATORY AND NUMERICAL INVESTIGATION OF INTERFACE DEBONDING OF BONDED CONCRETE OVERLAY OF ASPHALT AND ITS EFFECT ON THE CRITICAL STRESS IN THE OVERLAY

Feng Mu, PhD

University of Pittsburgh 2014

Bonded concrete overlay of asphalt (BCOA) is a viable technique for rehabilitating distressed asphalt pavements by bounding a Portland cement concrete overlay to the asphalt pavement. BCOAs are more durable solutions especially for highways and major city intersections where the constant maintenance using bituminous materials is not desirable. They also have advantages over the unbonded concrete overlays in terms of lower cost and lesser concern of the overhead clearance. As a result, BCOA has gained increasing popularity over the past two decades. Up to 2010, over 300 projects have been recorded in more than 35 states, totaling over 7.5 million m^2.

The key to a successful BCOA is to maintain the concrete-asphalt bond. When the bond is effective, the neutral axis of the overlay is shifted lower resulting in smaller tensile stress in the concrete and thereby allowing the thin overlay to carry large amounts of traffic. However, the bond degrades due to fatigue and the loss of the bond results in premature failure of the BCOA. Because of the lack of understanding of the interface debonding mechanism, the current BCOA design procedures still employ constant adjustment factors developed based on limited projects to account for the increase in the overlay stress due to partial bonding. The use of such empirical constants can lead to very unreliable design. Therefore, a quantitative framework that can predict the growth of interface debonding as a function of the fatigue loading is a key to improving the current design procedures.

A fracture mechanics based framework has been developed to determine the growth of debonding area as a function of the number of fatigue loads and the fracture energy subjected by each individual load. Wedge splitting tests were first performed to understand the interface fracture and investigate the debonding resistance of the interface under mode I loading. Accelerated loading tests were then conducted on BCOA slabs to simulate the fatigue of the interface bond. In addition, a transient-wave based nondestructive method was developed to detect the growth of the interface debonding and a cohesive zone model was established to calculate the fracture energy.

TABLE OF CONTENTS

LIST OF TABLES

LIST OF FIGURES

PREFACE

I would like to first express my gratitude to my advisor Professor Julie M. Vandenbossche for her educational and financial support through my PhD study. My thanks also go to the other faculty members on my committee Professors Donald J. Janssen, Jeen-Shang Lin, and John C. Brigham as well as Professor Piervincenzo Rizzo in the Department of Civil and Environmental Engineering for their generosity in lending me time, advice, and/or equipment. Without the inspiration, encouragement, and guidance from these professors, it would not been possible for me to accomplish this dissertation.

I am grateful to Mr. Charles C. Hager for his great tips both in the laboratory and my personal life, Mr. Ming Liu for the inspirational discussion on machine learning, programming and control, and Dr. Xianglei Ni as well as Mr. Kaiyuan Li for their help on nondestructive testing. I also would like to extend my appreciation to my other fellow graduate students and undergraduate students who devoted their time in helping conduct the laboratory experiment, i.e. Ms. Nicole Dufalla, Mr. Steven Sachs, Mr. Kevin Alland, Mr. Zichang Li, Mr. Oliver Green, Mr. James Kerins, Mr. Alexander Vuotto, and Mr. Joseph Santorine.

I owe the most to my parents and friends, Ms. Jingming Chen, Mr. Hsiang-Kai Lin, and Mr. Matthew Geary. They are always there to show me their love, patience and understanding, which helps me go through all the hard times during the journey of pursuing the truth.

Last, but not least, I would like to acknowledge the staff in PennDOT District 12, Swank Construction company and Frank Bryan Inc. for helping extract the asphalt specimens and donating the concrete.

1.0   INTRODUCTION

1.1   BACKGROUND AND MOTIVATION

Bonded concrete overlay of asphalt (BCOA) is a rehabilitation technique for distressed hot mix asphalt (HMA) pavements by bounding a thin or ultra-thin Portland cement concrete (PCC) overlay to the HMA. Thin BCOA refers to an overlay between 100 mm and 150 mm thick and ultra-thin BCOA represents an overlay 100 mm or thinner. The practice of constructing BCOA has gained increasing popularity since the early 1990s.

One of the keys in designing a BCOA as compared to the conventional concrete overlays that are 7 in or thicker is to ensure a good bond between the PCC overlay and the existing HMA is achieved. A strong bond increases the effective stiffness of the composite structure, thereby reducing the tensile stress in the overlay and thus making it possible for the thin overlay to carry the design traffic. However, this bond can fail due to repeated traffic and environmental loading either at the PCC-HMA interface or between the HMA lifts (Vandenbossche and Fagerness, 2002, Chabot et al., 2008). The delamination between the asphalt lifts mostly occurs when the milling depth of the HMA is poorly chosen so that there is a very thin asphalt surface course left after milling. Cracking then initiates between the remaining surface course and the base course. Therefore, this type of debonding can be prevented by carefully selecting the milling depth. On the other hand, the debonding at the PCC-HMA interface is less avoidable, as of result of which

1

the effective stiffness of the overlay is greatly reduced leading to the premature failure of the overlay.

The development of the PCC-HMA interface debonding is inadequately understood, which is reflected in the current BCOA design procedures. In these procedures (Tarr et al. 1998, Gucunski, 1998, Wu et al. 1999 and Roesler et al. 2008), the design thickness of a BCOA is calculated based on the fatigue damage in the overlay. In order to determine the fatigue damage, the design stress in the overlay is first predicted based on finite element (FE) analysis. A fully bonded condition is always assumed in the FE analysis due to the lack of understanding of the interface debonding. In order to consider the effect of debonding, an adjustment factor is applied to the FE predicted stress to calculate the design stress. The percent of adjustment is constant over the design life and is usually established by comparing the FE predicted strain with the measured strains from a limited number of in-situ projects. Tarr et al. (1998) recommended that the adjustment factor should be 1.67 times for thin BCOA. Wu et al. (1998) suggested the design stress for ultra-thin BCOA should be 1.36 times that of the FE predicted stress under fully bonded condition.

1.2   RESEARCH OBJECTIVE AND OUTLINE

The objective of this study is to achieve a better understanding of the interface debonding mechanism for BCOA, quantify the growth of the debonding as a function of the fatigue loads, and thus provide a more mechanistic framework to predict the fatigue of the BCOA.

Chapter 2 introduces a laboratory test, i.e. wedge splitting test (WST), to determine the resistance of the PCC-HMA interface to mode-I dominant fractures in terms of the critical energy

2

release rate. Customized BCOA small-scale block specimens were loaded to fail at the interface in order to obtain the relationship between the splitting load and the crack mouth opening. An analytical model was developed based on visco-elasticity and beam theory to analyze the relationship in order to determine the fracture energy release rate. The fracture energy release rate was established as a function of the initial notch depth, moisture, temperature, and roughness of the interface.

In Chapter 3, a cohesive zone model (CZM) was developed in the finite element environment to simulate the interface fracture of the BCOA. BCOA specimens fractured in the WST were first examined and four primary modes of failure were identified, namely the failure of concrete adhesion to asphalt matrix, the failure of concrete adhesion to exposed/crushed aggregate, aggregate breakage/pullout and asphalt fracturing. Five root CZMs were then proposed to represent the four types of failure enabling the simulation of the complicated interface fracture through simply superimposing the root CZMs. The fracture properties of the root CZMs were obtained based on an inverse analysis of the wedge splitting test results. The properties are material dependent yet independent from the composition of the interface, i.e. the milling effect, so that they can be used to model the debonding of BCOA slabs.

In Chapter 4, the theory and development of a non-destructive test (NDT) to detect the area of interface debonding for BCOA slabs is introduced. In the NDT method, stress waves were excited by impact loads and monitored after propagating and reflecting in the tested BCOA specimens. The development of the debonded area could then be predicted by comparing the monitored waves at different loading repetitions to the initial wave corresponding to a baseline (zero damage) condition. The prediction of this method was compared with the prediction of

another NDT method that was based on the deflections under quasi-static loading and a good agreement was observed.

In Chapter 5, the interface debonding under fatigue loading was recreated in the laboratory by conducting accelerated loading tests of BCOA slabs. The NDT method developed in Chapter 4 was used to detect the degree of interface debonding along the fatigue progress. Meanwhile, a finite element model was developed using the CZMs obtained in Chapter 3 to analyze the fracture energy subjected to the BCOA slabs at different stages of the fatigue test. As a result, the growth rate of the interface debonding could be established as a function of the fracture energy. Furthermore, a framework was proposed to update the critical stress in the overlay as the interface debonding progressively developed.

In the last chapter, all the findings from this study are summarized and recommendations for future research are made.

2.0   QUANTIFYING THE MODE I ENERGY RELEASE RATE FOR INTERFACE FRACTURE OF PORTLAND CEMENT CONCRETE BONDED TO HOT MIX ASPHALT

2.1   INTRODUCTION

Bonded concrete overlay of asphalt (BCOA) is a rehabilitation technique in which a thin (100-150 mm) or ultra-thin (100 mm or thinner) Portland cement concrete (PCC) overlay is placed to rehabilitate a distressed hot mix asphalt (HMA) pavement. The practice of BCOA has been in existence in the U.S. for more than 80 years, with the first documented project constructed in Indiana in 1918 (ACPA, 2012). BCOA constructed early on were not intentionally bonded to the underlying HMA and thus the overlay had to be relatively thick (200 mm or thicker) to survive the traffic and environmental loads. The success of the first bonded ultra-thin BCOA constructed in Louisville, Kentucky lead others to try this technology (Cole and Mohsen, 1993). It has been determined that BCOA can be constructed much thinner, provided an effective bond is available for increasing the composite stiffness of the structure, thereby reducing the tensile stress in the overlay. This emerging technology, i.e. BCOA with short (3 m or smaller) joint spacing, quickly gained popularity. From 1992 to 2001 approximately 300 BCOAs were paved in 35 states and during the 1990s over 50% of the states had constructed BCOA projects (Rasmussen and Rozycki, 2004). Part of this insurgence can be attributed to the development of procedures for designing these overlays in the mid to late 1990s. Test sections were constructed and instrumented in the mid to late 1990s in Minnesota, Iowa, Colorado and a number of other states (Rasmussen and Rozycki, 2004) to gain a better understanding of the failure mechanisms for these BCOAs. Now with over

10 years of performance data collected from these sections, the failure mechanism and design procedures for BCOA are being re-evaluated. As one component of such an effort, this study introduces a framework that quantifies the fracture energy release rate of the PCC-HMA interface to facilitate the incorporation of the mechanism of interface debonding into the design process of BCOA.

One of the most significant differences in the performance of BCOA, when compared to conventional concrete overlays, is the bond at the interface. Currently, interface debonding is taken into account by increasing the design stress in the overlay by a constant percentage based on engineering experience or limited dynamic strain measurements (Mu and Vandenbossche, 2011), which is very empirical and unreliable. However, this bond can fail due to repeated traffic and environmental loadings (Vandenbossche and Fagerness, 2002; Chabot et al., 2008) resulting in the premature failure of BCOA.

Interface debonding occurs when the facture energy release rate exceeds a critical value. The failure can be further broken down into mode I (tensile) and mode II (shear) depending on the nature of the stress contributing to the fracture at the interface. Stress contributing to mode I debonding develops when differential deflections occur across the joint between the loaded and unloaded slabs. Differential deflections across the joint can be significant for BOCAs considering that they are typically undoweled and the reduced thickness considering the relative increase in the depth at which the joints are sawed for bonded overlays provide little aggregate interlock to contribute in load transfer. As the loaded side of the joint deflects downward independently from the unloaded side, the asphalt on the unloaded side is peeled away from the concrete overlay. Stress contributing to mode I debonding can also develop due to the curling/warping of the overlay slabs as a result of temperature/moisture gradients. When the slabs curl/warp up, the continuous asphalt

tends to stay flat and thus debonding stresses are induced at the PCC-HMA interface. As a first step in quantitatively modeling the interface debonding, this study focuses on establishing a critical fracture energy release rate for these mechanisms only contributing to a mode I failure. This study will also evaluate the effect of multiple parameters especially the surface texture of the asphalt on the bond strength.

One key factor contributing to the strength of the bond is the surface texture of the asphalt prior to placing the overlay. The fact that milling the HMA prior to the placement of the overlay contributes to higher bond strengths between the HMA and the overlay was first quantified for test sections in Iowa (Grove et al., 1996). Milling the HMA creates a macrotexture that resulted in higher bond strengths, as measured using the Iowa shear test. The results from a study funded by the Colorado Department of Transportation provided similar results (Tarr et al., 1998). In this study, strain measurements were made on in-service pavements. It was found that the dynamic strains measured for overlays placed on milled HMA were 25% lower than for the unmilled smoother HMA surfaces. Chabot et al. (2008) also found a much rougher failure surface for debonded interfaces when the HMA was shot blasted prior to the overlay. In their research, the BCOA was constructed on a test track and cores from the test section revealed that it was tougher to fracture an interface with increased texture.

In this study, a description of the test procedure and test specimens developed to characterize the mode I failure at the PCC-HMA interface is first provided. Then, an analytical model developed to predict the response of the loaded specimen is introduced. Finally, the model is validated and the effect of the HMA surface texture on the bond is quantified.

2.2   WEDGE SPLITTING TEST

The wedge splitting test (WST) (Brühwiler & Wittmann, 1990) was employed to produce a mode I dominant failure at the interface of the BCOA specimens. The specimens consist of a block with one half constructed of HMA and the other of PCC cast onto the HMA, as shown in Figure 2.1. A small square of material is removed from the central portion of the specimen where the clip gage resides for monitoring the crack mouth opening. A notch is cut in the central portion of this region at the interface of the two materials to establish the location where the crack will propagate. Furthermore, a guide notch of approximately 6 mm deep was also made both sides of the specimen to ensure the crack propagates along the interface. The characteristics of all the tested WST specimens can be found in Appendix A.
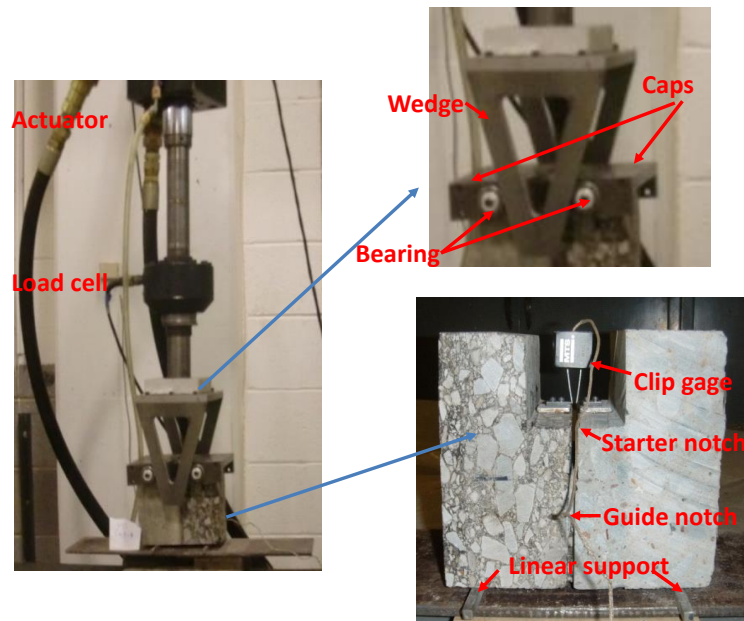
Figure 2.1. WST configuration (left) and the wedge and the specimen (right).

2.2.1 Experiment configuration

The setup of the WST is illustrated in Figure 2.1. A steel cap is placed on each half of the specimen of which round bearings rest. These bearings, together with the wedge, transform the axial load from the actuator to horizontal splitting forces onto the specimen. The transformation is defined by Equation (2.1). The WST specimen rests on two linear supports, which are aligned with the bearings as well as the center of gravity of each half specimen. This alignment minimizes the moment induced by the vertical force relative to the interface. A clip gage is instrumented at the mouth of the starter notch to monitor the crack mouth opening displacement (CMOD). The WST specimen is loaded to failure, with a constant rate of CMOD.

$$F_H = \frac{F_V + P_{wedge}}{2tan\theta}$$

(2.1)

where

F_H=splitting force,

F_V=axial load by the actuator,

P_{wedge}=0.05 kN, the weight of the wedge used in this study and

θ=15°, the wedge angle used in this study.

2.2.2 Specimen preparation

Each half of the specimen has a geometry of approximately 150 mm (L) ×150 mm (W) ×90-110 mm (T). The HMA was obtained from Route 50 in Bridgeville, PA, which was an in-service pavement being reconstructed. Prior to the removal of the HMA pavement, portions of the HMA

surface were milled while other areas were left unmilled. The thickness of the HMA was approximately 90 mm for the milled sections and 110 mm for the unmilled sections.

A sand patch test (ASTM-E965-96) was carried out on both the milled and unmilled HMA specimens to obtain a characteristic depth that correlates to the surface roughness. The difference in the roughness between the milled and unmilled HMA surfaces can clearly be seen in Figure 2.2.

(a)   (b)

Figure 2.2. Surface of (a) milled and (b) unmilled HMA specimen

The composite specimens were made by casting concrete onto the HMA. These specimens were wet cured for 28 days. The HMA portion of the composite specimen was wrapped with duct tape prior to placing it in the curing room for waterproofing, thereby minimizing the degradation of the HMA due to moisture. After curing, all the specimens were air dried under room temperature before testing.

2.2.3 Material properties

The concrete used to construct the specimens was cast in two separate batches. The material properties for both mixtures were measured immediately after the WST was performed and the results are presented in Table 2.1. Although concrete from Batch 2 appears to be stiffer and

stronger than that from Batch 1, they both present a much higher stiffness than the asphalt used in the study.

A power function is used to express the relaxation modulus for a viscous material, as shown in Equation (2.2).

Table 2.1. PCC material properties.

		Number of samples	Average	Standard deviation
Elastic modulus, GPa	Batch 1	3	28.3	0.2
	Batch 2	3	26.8	1.0
Poisson's ratio	Batch 1	3	0.21	0.01
	Batch 2	3	0.19	0.01
Compressive strength, MPa	Batch 1	3	28.8	0.4
	Batch 2	3	23.0	3.1
Specimen age, days	Batch 1	3	28	
	Batch 2	3	161	

$$E(t) = E_{ref}t^{-m} \tag{2.2}$$

where

E_{ref}= reference modulus,

t= time and

m=relaxation factor that characterizes the viscosity of the material.

For an elastic material, m in Equation (2.2) should be zero. For the HMA mixture used in this study, the relaxation modulus was measured using cylindrical specimens of 150 mm in diameter and 250-300 mm in height under an unconfined uniaxial compression. Stress was applied to the specimen and maintained until a strain of approximately 1% was achieved. This was performed under two stress levels (0.35 MPa and 0.6 MPa) and at a temperature of 20 ℃. The m

value as well as E_{ref} were then determined and are presented in Table 2.2. Although the compressive response of the HMA does not exactly represent its flexural response, one can still conclude, based on the m values in Table 2.2, that the HMA mixture has a relatively elastic response. This is probably due to the temperature at which the test was performed and the aging of the asphalt, which was in-service for many years.

Table 2.2. m and E_{ref} measured for the HMA.

Specimen	Stress level, MPa	Final strain, %	E_{ref}, MPa	m
1	0.3	0.9	65	0.09
2	0.4	1.0	60	0.05
3	0.6	1.1	90	0.06

2.2.4 Loading rate

As previously mentioned, the rate of loading was dictated by the CMOD rate. The CMOD rate was carefully selected, since the performance of HMA, and most likely the interface as well, is highly dependent on the displacement rate due to the viscous properties of the asphalt binder. A few of the specimens, as shown in Table 2.3, were loaded with only the weight of the wedge.

Table 2.3. CMOD rates due to the weight of the loading head.

Specimen	Size (H×W), mm	Normalized notch depth*, %	R_{Wedge}, mm/min
1	150×100	37	0.033
2	150×100	12	0.008
3	150×150	31	0.033
4	150×150	10	0.0008
5	200×150	35	0.0030
6	200×150	9	0.003

* normalized by the nominal contact area

It was noticed that the CMOD began to increase even without receiving the external load from the actuator. The increase is more significant when the notch at the interface is deeper. Therefore, it was determined that the CMOD rate used during testing should be set relatively high so the increase in CMOD resulting from the weight of the loading apparatus was negligible. On the other hand, the CMOD rate should not be so high that abrupt failure occurs, making the collection of post-crack behavior impossible. Based on this, a CMOD rate of 0.5 mm/min was adopted in this study.

2.3   WST RESULTS

The WST was performed on specimens cast using milled and unmilled asphalt. The relationship between the splitting force and the CMOD consists of two general forms, as shown in Figure 2.3. For both milled and unmilled specimens, some of the load-displacement curves presented a distinct peak within a couple of seconds after loading began. Other specimens exhibited a plateau before the splitting forces began to decline. After careful examination of the test data, it is found that the peak load depicted for specimens "Milled-1" and "Unmilled-1" is not the point at which interface debonding begins.
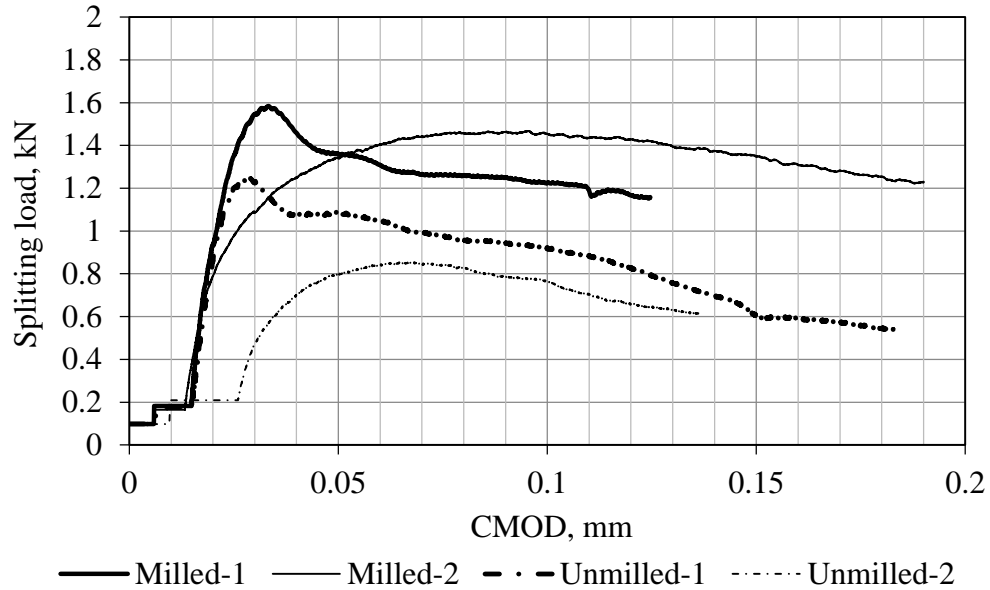
Figure 2.3. Load-displacement curve tested at room temperature and a displacement rate=0.5

mm/min.

The decline in the splitting force can most likely be attributed to the actuator finally achieving the desired CMOD rate after falling behind during the first two to three seconds. Evidence supporting this hypothesis can be found by examining the CMOD-time history. The CMOD-time history for the "Milled-1" specimen from Figure 2.3 is presented in Figure 2.4. The peak for the "Milled-1" curve in Figure 2.3 occurs at a CMOD of approximately 0.03 mm. Figure 2.4 shows the loading rate also converges to the target loading rate of 0.5 mm/min at a CMOD of 0.03 mm. Therefore, for both types of responses, it is difficult to determine the initiation of interface debonding by just investigating the load-displacement relationship.
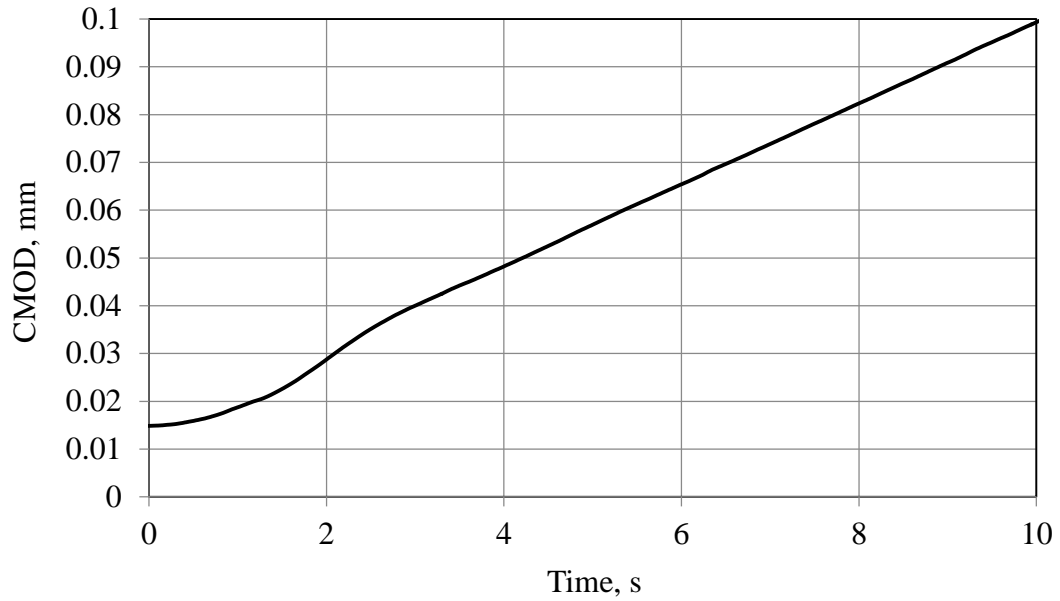
Figure 2.4. CMOD rate for the Milled-1 specimen with time 0 indicating the initial time of

loading by the actuator.

Figure 2.3 does show that the milled specimens required a greater splitting force than the unmilled specimens to achieve the same CMOD. This indicates that milling the asphalt enhances the fracture resistance of the interface. Moreover, it is also found that the notch depth plays an important role in the interface debonding. Figure 2.5 presents the load-displacement curves for three unmilled specimens. These specimens have the same interface roughness and only vary in that the notch depth is different. The notch depths considered include 13%, 27% and 45% of the depth of the specimen. It is apparent that the fracture toughness for the specimen with the smallest notch is the largest.
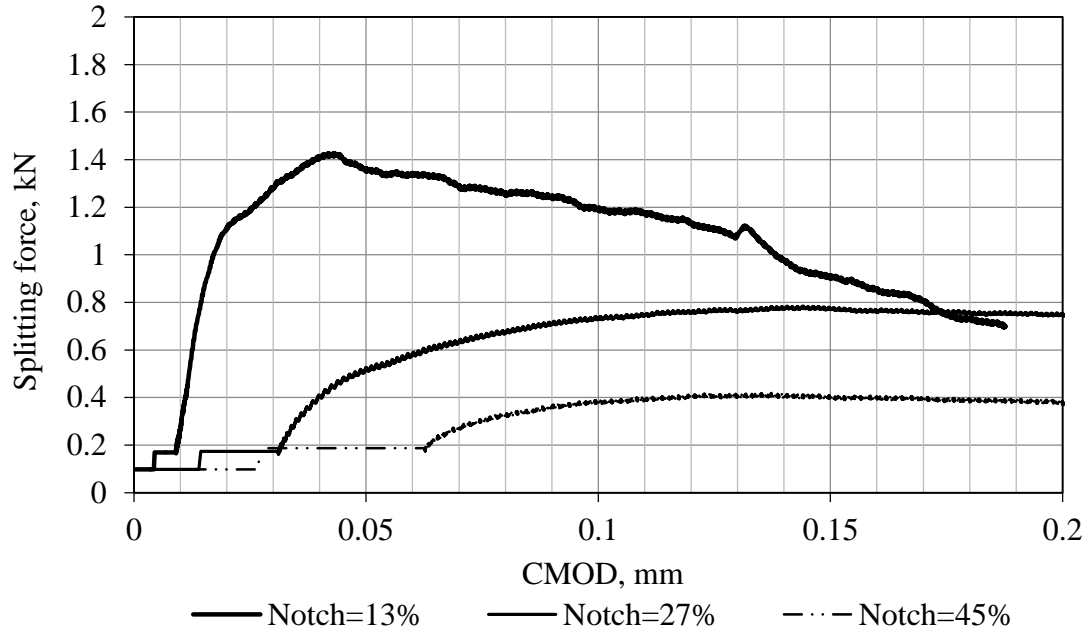
Figure 2.5. Load-displacement curve for unmilled specimens with different notch depths, tested

at room temperature and displacement rate=0.5 mm/min.

2.4   MODEL FOR DETERMINING THE ENERGY RELEASE RATE USING THE

WST TEST

2.4.1   Model development

It can be seen in Figure 2.6, that the configuration for the WST resembles the geometry of two

cantilever beams. Therefore, the CMOD monitored by the clip gage can be estimated by

determining the bending of two WST beams, where the splitting forces are acting on the extension

of the WST beams. The deflection at the end of the WST beams (the CMOD) can be related to the

splitting forces by assuming that the WST beams are under steady-state equilibrium during the

bending, as presented in Equation (2.3).

16
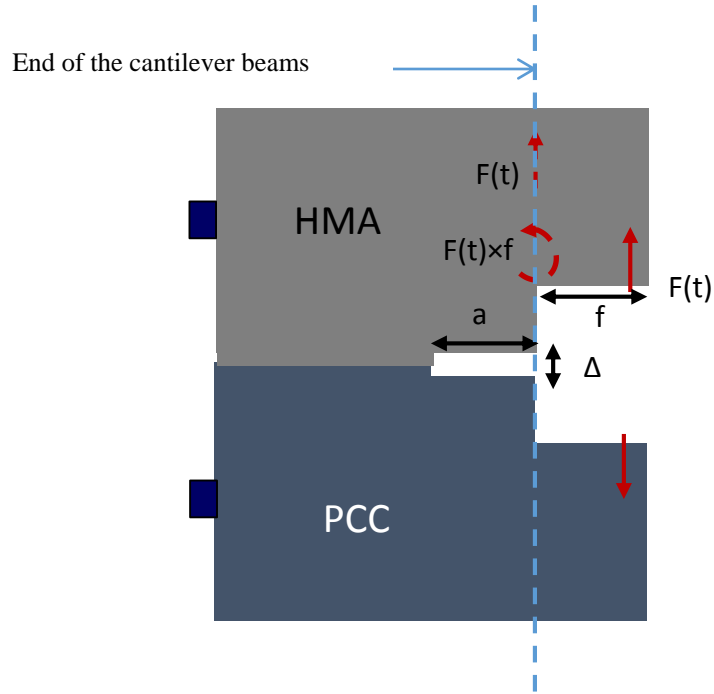
Figure 2.6. Analogy between the WST and cantilever beams.

$$\Delta = \Delta_{Load} + \Delta_{Moment} = \frac{Fa^3}{3EI} + \frac{Ma^2}{2EI} = \frac{F}{EI}\left(\frac{a^3}{3} + \frac{fa^2}{2}\right) \tag{2.3}$$

where

Δ=CMOD, mm,

F=splitting force acting on the bearings, kN,

a=length of the WST beam, mm,

E=stiffness of the WST beam, GPa,

I=moment of inertia of the WST beam, mm^4 and

f=distance between the bearing and the mouth of the notch as shown in Figure 2.6, mm.

For a HMA beam with visco-elastic responses, Equation (2.3) becomes Equation (2.4).

$$F(t) = \frac{6I_{HMA}}{2a(t)^3 + 3fa(t)^2} \int_0^t E(t-\tau)\frac{d\Delta_{HMA}(\tau)}{d\tau}d\tau \tag{2.4}$$

where

17

$a(t)$=crack length as a function of time, mm,

I_{HMA}=moment of inertia of the HMA beam, mm^4.

$E(t)$ =relaxation modulus of the HMA, GPa and

$\Delta_{HMA}(t,\tau)$=CMOD due to the bending of the HMA half of the WST specimen, as a function of time t or τ.

It is reasonable to assume that $\Delta = \Delta_{HMA}$, because the stiffness of the HMA corresponding to the temperature and loading rate used in the WST is substantially lower than that of the PCC. Moreover, this difference increases as creep occurs in the HMA with time. Therefore, Equation (2.5) can be derived after introducing Equation (2.2) into Equation (2.4) and assuming $\Delta=\Delta_{HMA}$.

$$F(t) = \frac{6I_{HMA}}{2a(t)^3 + 3fa(t)^2} \int_0^t E_{ref} t^{-m} \frac{d\Delta_{Total}(\tau)}{d\tau} d\tau \qquad (2.5)$$

The discrete expression of Equation (2.5) is derived and presented in Equation (2.6). This derivation facilitates the analysis of the test data that was collected at equal increments in time, i.e. $F(t)$ and Δ_{Total}(t).

$$F(x) = \frac{6I_{HMA}}{2a(x)^3 + 3fa(x)^2} \sum_0^{y=x} E_{ref} (x-y)^{-m} \cdot \delta\Delta_{Total}(x) \qquad (2.6)$$

where $\delta\Delta_{Total}(x) = \Delta_{Total}(x+1) - \Delta_{Total}(x)$, the increment of the CMOD between two adjacent sampling points, mm.

Knowing the splitting force as well as the CMOD, the energy release rate can be determined as the energy required to progress the crack a unit length, as in Equation (2.7).

$$G \equiv \frac{W(t)}{Bda(t)} = \frac{F(t)d\Delta_{Total}(t) + F(t)fd\theta_{Total}(t)}{Bda(t)} \qquad (2.7)$$

where

18

G=energy release rate, N·m/m^2,

$\Delta_{Total}(t)$=total CMOD, mm,

$\theta_{Total}(t)$=total angular displacement at the crack mouth, radian,

B=width of the specimen, mm and

$a(t)$=crack length, mm and $a(0)$ is the initial notch depth.

Based on the elastic beam theory, the relationship between Δ_{Total} and θ_{Total}, can be obtained as shown in Equation (2.8).

$$\theta_{Total} = \frac{3\Delta_{Load}}{2a} + \frac{2\Delta_{Moment}}{a} = \frac{3(a + 2f)}{a(2a + 3f)}\Delta_{Total} \qquad (2.8)$$

Therefore, the energy release rate in Equation (2.7) can be simplified to Equation (2.9).

$$G = \frac{F(t)d\Delta_{Total}(t)}{Bda(t)}C(t) \qquad (2.9)$$

where $C(t)$ is a function of the WST geometry as shown in Equation (2.10).

$$C(t) = \frac{2a(t)^2 + 6fa(t) + 6f^2}{2a(t)^2 + 3fa(t)} \qquad (2.10)$$

2.4.2 Model employment

The history of the splitting force $F(t)$ can be estimated based on the measured $\Delta_{Total}(t)$ using Equation (2.6). When there is no crack initiation during the relatively linear growth of $F(t)$, the crack depth is equal to the notch depth, i.e. $a(t)= a(0)$. Therefore, the coefficients, m and E_{ref} in Equation (2.6) can be estimated by matching the predicted and measured $F(t)$ during the initial loading period. An example of this process is presented in Figure 2.7. The curve 'Prediction with constant crack length' presents the prediction of $F(t)$ based on m =0.8, E_{ref} =9.7 MPa at

$a(t) = a(0)$. There is good agreement between the predicted and measured F(t) up to a CMOD of approximately 0.04 mm, when interface debonding began to develop.

The difference between the predicted and measured F(t) when the CMOD is greater than 0.04 mm can be minimized by allowing the crack to grow, i.e. increasing the crack depth $a(t)$ incrementally until the two curves overlap. In Figure 2.7, an example of such an operation is presented and it can be seen that the consideration of the growth of crack results in an improved estimation of the loading history.
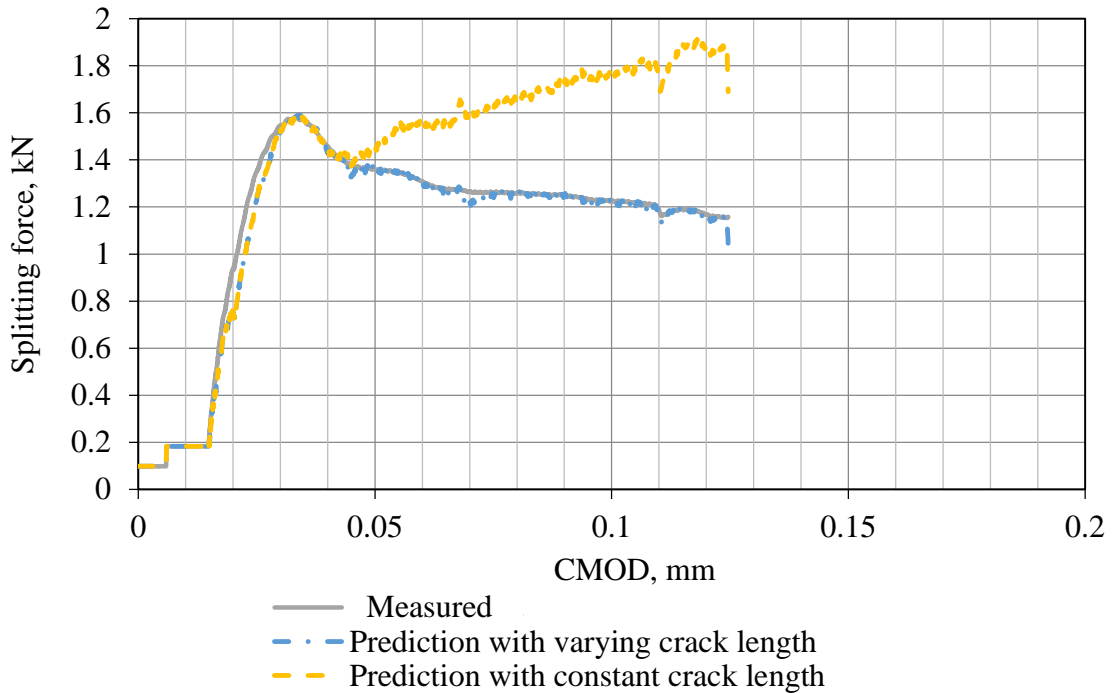
Figure 2.7. Measured and predicted load-CMOD curves for the 'Milled-1' specimen in Figure 2.3.

It has been discussed that the quick peak load that that occurs right after the start of the loading is the result of an unstable CMOD rate, while not an indication of interface failure. For most of the specimens that presented a stable constant CMOD rate, similar to the results shown in Figure 2.8, the initiation of the crack usually occurred at 60% -90% of the peak load.
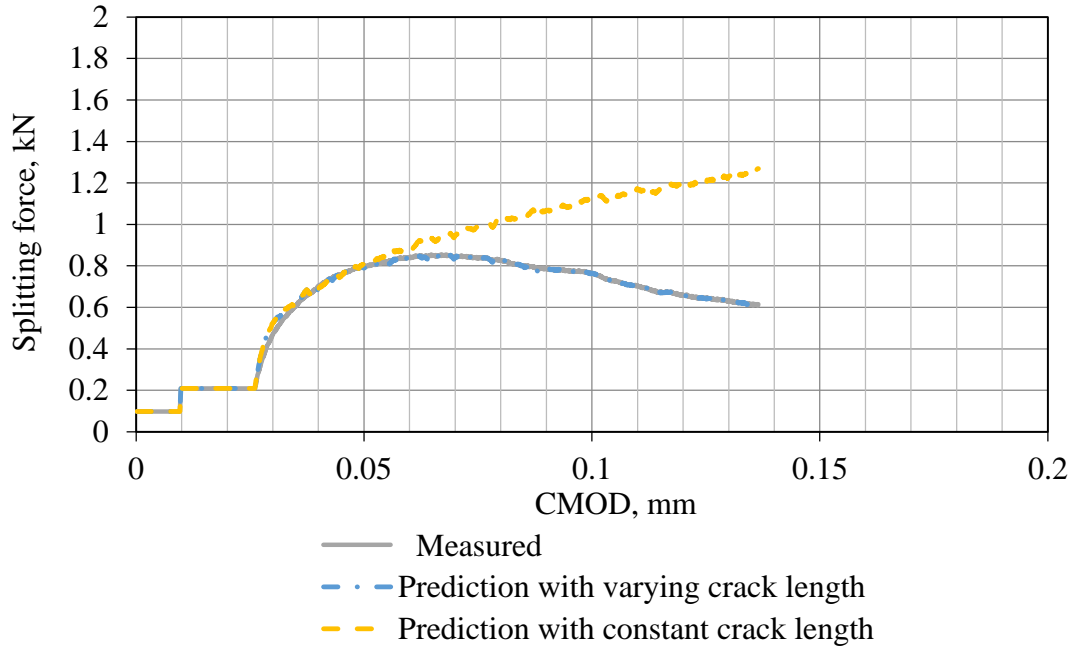
Figure 2.8. Measured and predicted load-CMOD curves for the 'Unmilled-2' specimen in Figure 2.3.

The wedge splitting test was carried out under different moisture and temperature conditions to study the effect of moisture and temperature on the interface fracture. The test results for specimens tested at 1. dry and room-temperature conditions, 2. wet and room-temperature conditions, and 3. dry and freeze conditions are summarized in Appendices B, C and D, respectively. In these appendices, the load-CMOD curves were also predicted using the model developed in Section 2.4.1 and showed a good agreement with the measured values.

The parameters in Equation (2.2), i.e. m and E_{ref}, were determined during the application of the model. Their values are presented in Table 2.4. To summarize, m varies between 0.4 and 0.8 and E_{ref} varies between 1400 and 16000 for the milled specimens at room temperature. For the unmilled specimens tested at room-temperature, m varies between 0.5 and 0.7 and E_{ref} varies between 800 and 7700. With respect to the specimens tested in a frozen condition, m varies

21

between 0.16 and 0.25 and E_{ref} varies between 28000 and 84500 for the milled specimens and m varies between 0.2 and 0.3 and E_{ref} varies between 20000 and 42000 for the unmilled specimens.

Table 2.4. m and E_{ref} for all the WST specimens.

Specimen	Testing temperature, °C	Moisture condition	Milled	m	E_{ref}, MPa
2-07	23	Dry	Y	0.8	10
2-08	23	Dry	Y	0.67	12
2-09	23	Dry	Y	0.7	14
2-12	23	Dry	Y	0.5	59
2-13	23	Dry	Y	0.57	52
2-15	23	Dry	Y	0.58	36
S-01	23	Dry	Y	0.4	110
2-01	23	Dry	N	0.69	14
2-02	23	Dry	N	0.65	7
2-03	23	Dry	N	0.7	6
S-10	23	Dry	N	0.55	37
S-11	23	Dry	N	0.48	14
S-13	23	Dry	N	0.55	39
S-15	23	Dry	N	0.55	53
S-04	23	Wet	Y	0.5	69
S-12	23	Wet	N	0.7	11
S-14	23	Wet	N	0.6	26
2-10	-13	Dry	Y	0.16	324
2-11	-13	Dry	Y	0.16	193
2-14	-13	Dry	Y	0.25	583
2-04	-13	Dry	N	0.3	138
2-05	-13	Dry	N	0.25	138
2-06	-13	Dry	N	0.2	290

Three conclusions can be made based on the comparison of the above ranges. First, E_{ref} is generally greater for milled specimens than unmilled specimens. Second, m seems to depend on the temperature not the milling condition. The variation of the m value at the same temperature is believed to be due to the deviation in the initial loading rate and the PCC and HMA material

properties. Finally, the deviation of m and E_{ref} for the milled specimens is larger than that for the unmilled specimens, as expected since the failure surface for the milled specimens is rougher.

A more important function of the model is that the history of the crack propagation is revealed. Since the fracture energy up to any crack depth can be determined by solving the integral of Equation (2.9), the energy release rate can be obtained by calculating the slope of the fracture energy against the crack depth, as shown in Figure 2.9. The energy release rate was calculated for all the specimen and the results were presented in Appendix E.
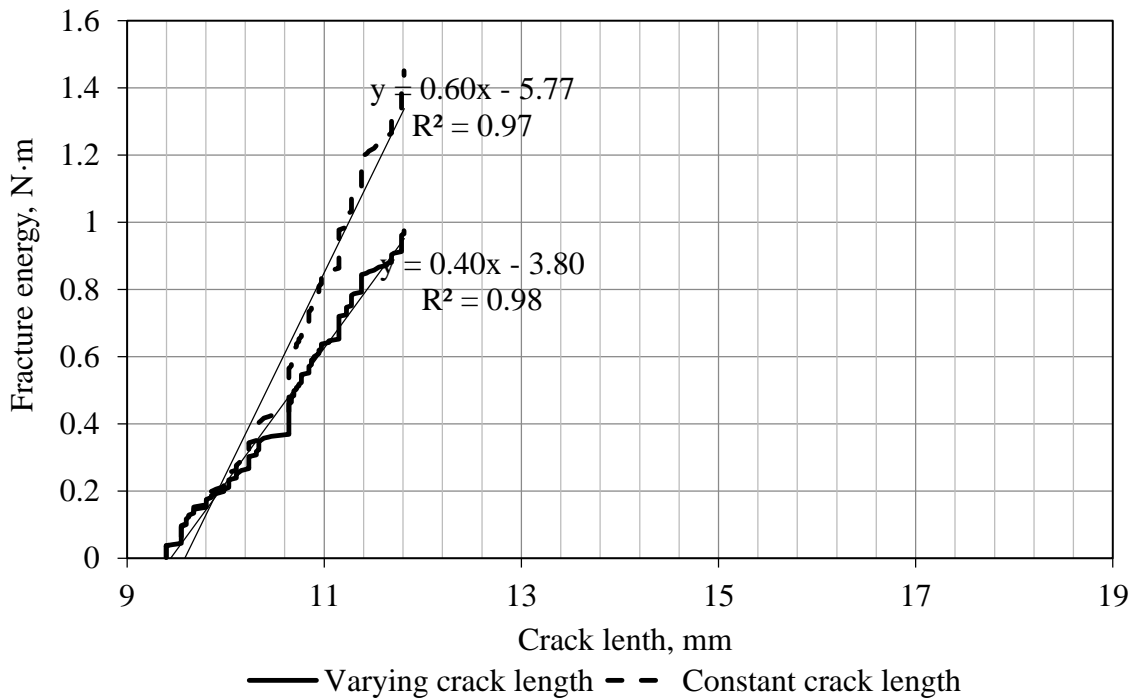
Figure 2.9. Fracture energy release rate for the 'Milled-1' specimen in Figure 2.3.

The determined crack propagation was validated by comparing the predicted crack depth with the measured crack depth at the end of the test. The results of such comparison are presented in Table 2.5, where only the specimens having final crack depth measurements available on both sides and not failing abruptly were included. It should be noted that the average of the two side measurements does not necessarily represent the characteristic depth of the crack. Nevertheless,

the comparison between the averaged side measurements and those predicted at least confirms the ability of the method in differentiating quick and slow crack development.

Table 2.5.Comparision between measured and predicted crack lengths.

Specimen	Measured crack length, mm			Predicted crack length, mm
	Front	Back	Average	
WST-2-7	0	11	6	3
WST-2-12	8	16	12	8

2.5   CONCLUSIONS

A wedge splitting test setup is developed to fracture BCOA specimens at the interface in mode I. The test was carried out under CMOD control and the splitting force and CMOD data was recorded during loading. An analytical model was then established to characterize the response of the specimen. The model is based on beam theory, considers the viscoelasticity of the material and more importantly is able to identify the initiation as well as the growth of the interface crack.

Using the model, the initiation as well as the growth of the interface crack was simulated for both milled and unmilled specimens. The energy release rate was then determined for each specimen. It is found that the interface for BCOA can be modeled as a visco-elastic layer of a defined width. The viscosity of the interface layer appears to be a function of the loading frequency, indicated by the fact that m is a function of the displacement rate. However, m was found not to be sensitive to the surface texture (milling condition) of the asphalt. On the other hand, the stiffness of the interface layer appears to be dependent on the interface roughness, since it was shown that E_{ref} is greater for a milled HMA interface than unmilled HMA interface. A substantially rougher failure surface was also found for the milled HMA interface implying that

24

the failure plane appears to be wider for a milled HMA interface than for an unmilled HMA interface. The increase in the thickness of the failure plane helps explain the increase in stiffness of the interface layer for milled HMA.

3.0 SIMULATING CONCRETE-ASPHALT INTERFACE FRACTURE BY SUPERIMPOSING COHESIVE ZONE MODELS WITH INPUTS ESTABLISHED USING THE WEDGE SPLITTING TEST

3.1 INTRODUCTION

Bonded concrete overlay of asphalt (BCOA) has been widely used to rehabilitate distressed asphalt pavements (Rasmussen and Rozycki, 2004). The key to a successful BCOA project is to maintain an effective bond between the concrete overlay and the asphalt, which would increase the composite stiffness of the structure and thereby reduce the tensile stress in the overlay. Interface debonding has been identified as the primary failure mechanism for BCOA (Nelson and Rasmussen, 2002; Vandenbossche and Fagerness, 2002 and Vandenbossche, 2005).

Interface debonding for BCOA results from the cracking along the interfacial zone (IZ) between the concrete and the asphalt, which is composed of both materials. An important mechanism for the development of debonding is the mode I (opening) crack propagation within the IZ. BCOA slabs are typically undoweled and the reduced contact area between the slab faces at the joint provides little aggregate interlock to contribute to load transfer across the joints. As the traffic load deflects the loaded side of the joint downward independently from the unloaded side, the asphalt on the unloaded side tends to separate from the concrete overlay. The repeated load applications eventually results in the development of a crack within the IZ.

Mu et al. (2013) simulated the concrete/asphalt interface fracture of this opening mode using the wedge splitting test (WST), a laboratory test proposed by Brühwiler and Wittmann (1990) to produce mode I cracking. WST has been employed to simulate the interface fracture of

composite materials and provide laboratory measurements to calibrate or validate interface fracture models. Tschegg and Rotter (1995) performed WST to study the interface fracture between aggregate and cement. Walter et al. (2005) determined the traction-separation law for the steel-concrete interface fracture based on an inverse analysis of WST results. Tschegg and Jamek (2011) studied the fracture between two asphalt mixes in WST under fatigue loading. In modeling the interface fracture of composite materials, such as the previous studies, it is traditional to model the interface as a straight plane where the two dissimilar materials adhere. It is also common to determine the fracture properties of the interface based on the inverse analysis of the WST results. However, this approach is not appropriate for the analysis of interface debonding for BCOA. Physically, BCOA interface consists of an aged asphalt matrix, exposed aggregates and hydrated concrete that adheres to the two substrates at various depths. The depth of concrete penetration depends on the surface texture of the asphalt, which is a function of the age and wear of the asphalt, and any pre-overlay preparation such as milling. The typical asphalt textures before and after milling is illustrated in Figure 3.1. This composition of the BCOA interface is supported by the observation of in-situ BCOA debonding (Vandenbossche and Fagerness, 2002), where interfacial cracks were observed both at the plane of contact between concrete and asphalt and into the asphalt. Therefore, it is more physically sound to assume that the thickness of the IZ should be a function of the HMA texture and the fracture properties of the IZ should be related to the properties of its constituents.
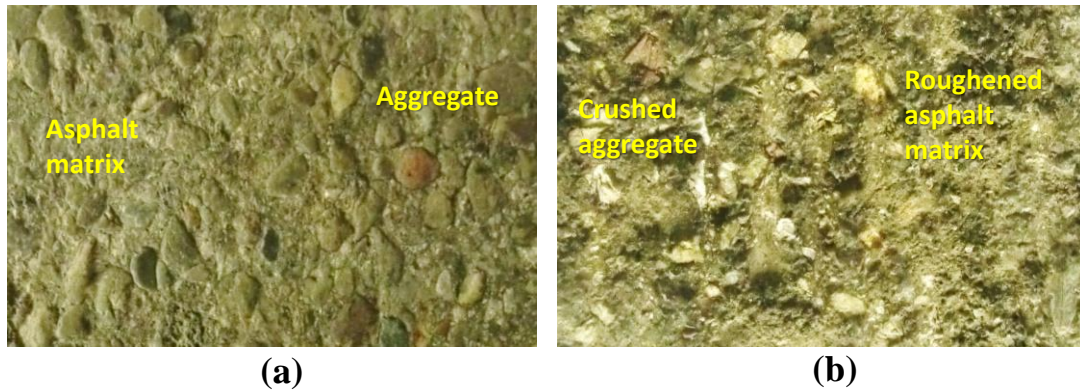
Figure 3.1. Typical asphalt surfaces before casting concrete (a) unmilled and (b) milled.

In this study, the interface fracture of BCOA was modeled using superimposed cohesive zone models (CZM). The interface cracking was first broken down into several types of constitutive failure. Root CZMs were used to represent the constitutive failure types with the model inputs for each root CZM being only material dependent. The inputs for the root models were established based on small-scale laboratory tests, for example WST, and then applied to the analysis for the fracture of a larger structure, such as BCOA slabs. This study employed the WST results presented in Section 2.3 to establish the fracture properties for the BCOA interface based on an inverse analysis. Furthermore, the effect of milling and specimen size on the fracture properties was also investigated.

3.2   COHESIVE ZONE MODEL

CZMs are widely used to simulate the progression of nonlinear cracking. In a CZM, the crack path is represented by two adjacent but separated surfaces whose separation indicates the opening of the crack. Tractions are assumed to exist between the two separating surfaces in order to avoid the

stress singularity at the crack tip in linear elastic fracture mechanics. The constitutive relationship for the CZM is a traction-separation law (TSL). A basic TSL includes three phases. In the first (no-damage opening) phase, traction increases with the separation without any damage caused until the peak traction is reached. The second phase is the softening phase, where the traction decreases with further separation due to the occurrence and accumulation of damage. The last phase is characterized by the cohesive separation exceeding a critical value resulting in zero traction and proceeding cracks. The basic TSL has mutated to various shapes in order to reflect different cracking mechanisms in different materials. The typical TSLs that have been used to model concrete, asphalt or the interface of composites are summarized in Figure 3.2.
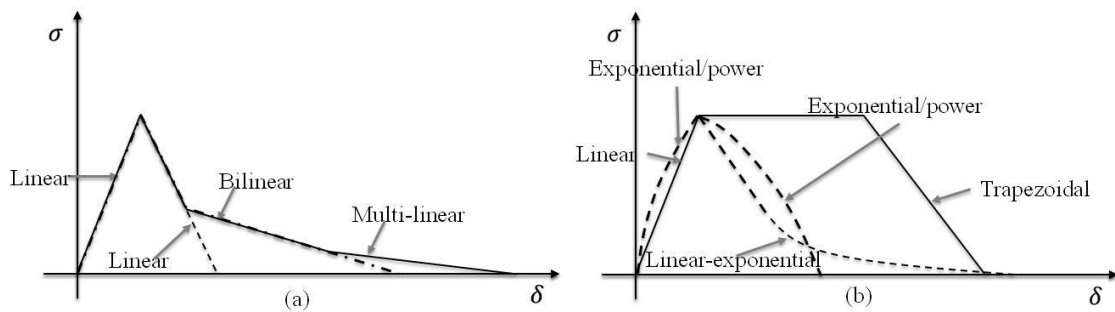
Figure 3.2. Traction-separation laws for (a) concrete and (b) asphalt and interfaces.

3.2.1   CZM for concrete

A CZM with a linear softening phase (i.e. bilinear TSL) was first proposed by Hillerborg et al. (1976) to model the quasi-brittle fracturing of plain concrete. In Figure 3.2 (a), this CZM presents a softening phase, where the traction linearly decreases with increased separation, which reflects the damage accumulation due to plasticity in quasi-brittle materials (Ural et al., 2009). CZMs with a bilinear softening phase are more often used for the modeling of plain concrete fracture (Guinea et al., 1994 and Bazant and Becq-Giraudon 2002). The bilinear softening reflects the aggregate

29

bridging across the crack in addition to the plastic damage accumulation. For the fracture of fiber reinforced concrete, Park et al. (2010) introduced multi-linear softening that presents an additional requirement of fracture energy relative to the bilinear softening to take into account the fiber bridging during fracture.

3.2.2 CZM for asphalt

Kim et al. (2008) employed a CZM with a bilinear TSL to simulate the fracture of asphalt at low temperatures (-10 °C). The linear softening was believed to reflect the damage mechanism due to plastic deformation. Power-law softening was compared with linear softening by Song et al. (2008) and it was concluded that the power law was better in analyzing the fracture of asphalt at low temperatures (-10 °C to -30 °C).

3.2.3 CZM for interface

Mohammed and Liechti (2000) used a bilinear TSL to study the fracture between aluminum and epoxy. The properties of the TSL were inversely determined from third point bending measurements. The model showed good predictability for failures with various initial flaw sizes. Another TSL with bilinear softening law was adopted by Li et al. (2005) to study the fracture of adhesively bonded fiber reinforced composites. It is more popular to model the fracture of adhesively bonded joints using a trapezoidal TSL, as shown in Figure 3.2 (b) (Tvergaard and Hutchinson, 1992; Feraren and Jensen, 2004 and Alfano et al., 2007). The shape of a TSL affects its performance in modeling the interfacial fracture. Alfano et al. (2009) conducted a comparison between the bilinear, linear-exponential and trapezoidal TSLs in modeling the aluminum-epoxy

joint fracture. The three TSLs yield different predictions despite the fact that the cohesive strength as well as the fracture energy is the same among the models.

3.3   CZM FOR BCOA INTERFACE

An examination of the BCOA specimens after failure revealed that the interface fracture is composed of many subcritical failures such as: the concrete/asphalt matrix debonding, concrete/exposed aggregate debonding, aggregate pull-out, aggregate cracking, and asphalt cracking, instead of one critical failure. Figure 3.3 shows a picture of the interface after fracture for both milled and unmilled specimens. Since the fracture of the unmilled specimens is cleaner, Figure 3.3 (a) was first examined. Six failure types could be identified, for which the location and mechanisms are summarized in Table 3.1.

(a)   (b)
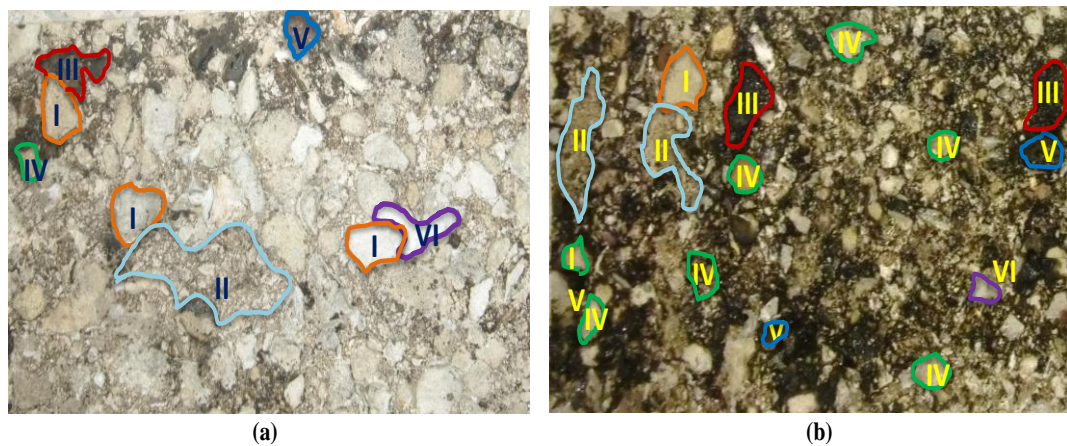
Figure 3.3. Fractured BCOA interface on the concrete side (a) a unmilled specimen and (b) a milled specimen: (I) adhesion failure between concrete and aggregate (II) adhesion failure between concrete and asphalt matrix (III) asphalt failure (IV) aggregate facture (V) aggregate pullout and (VI) voids.

31

Table 3.1. Location and mechanism for subcritical failures.

Failure Type	Location	Mechanism
(I)	Interface between concrete and exposed asphalt aggregates	Adhesion*
(II)	Interface between concrete and asphalt matrix	Adhesion
(III)	Asphalt matrix	Cohesion**
(IV)	Aggregate fracture	Cohesion
(V)	Pullout of aggregates from asphalt matrix	Adhesion
(VI)	Voids at the concrete/asphalt interface	N/A

*Adhesion is the bonding force between two different materials
**Cohesion is the bonding force within the same material

The Type I failure is obvious since the shape of the failures agrees with the shape of the exposed aggregates observed before casting the concrete. The Type II failure is the adhesion failure between the concrete and asphalt matrix, which consists of two mechanisms. After magnification, it is apparent that the failure is actually a mix between an adhesion failure in the cement paste (grey dots within the area) and asphalt adhesion failure (darker dots within the area) but the cement adhesion failure is predominant. The Type III failure is easily detected when the asphalt matrix cracks leaving chunks of asphalt adhered to the concrete side of the failure plane. The Type IV failure is mostly found when there are aggregates of poor quality, such as sandstone. The Type V failure occurs when the concrete adhesion on the exposed aggregates is greater than the asphalt adhesion and Type VI is a void at the interface, where no harden cement is present and thus the interface strength is zero.

Although the fracture of the milled specimen, Figure 3.3 (b), is more difficult to interpret, the same failure types can still be concluded after carefully comparing Figure 3.3 (b) with the asphalt surface before casting the concrete. There are some differences in the fracture between the milled and unmilled specimens. First, the amount of Type I and Type II failures is significantly lower in the milled specimen. This is because the texture of the exposed aggregates and asphalt matrix is roughened by the milling operation resulting in a stronger bond between them and the

fresh concrete. As a result, the cracking path tends to go through the asphalt. More interestingly, a closer examination of the Type II failure reveals that there is nearly no bond at locations where the milling operation created deep grooves. These grooves are approximately 5-25 mm deep, relative to the other post-milling area where there is evenly distributed crushed aggregates/roughened asphalt matrix. Aggregates from the fresh concrete could bridge and shield the grooves preventing the concrete from bonding to the milled asphalt at the bottom of the grooves. Moreover, dust and debris may be deposited there before the concrete placement and behave as a bond breaker, preventing bonding even if fresh concrete was able to enter the grooves. The second difference is that Types III, IV and V failures become predominant, which is also a product of the milling and compliments the decrease of Types I and II failures.

It can be concluded from the above examination that an effective CZM for the interfacial fracture of BCOA should be based on the superimposition of certain root CZMs. Each of the root CZMs should reflect one of the subcritical types of failure. The advantage of using such a superimposition approach is as follows. First, the root CZMs are only dependent on material properties. Therefore, they can be used for modeling at multiple scales. Second, the shape of the overall CZM after superimposition is a function of the interfacial composition. Theoretically, it can be any shape. Such flexibility is desirable when the overall CZM is determined based on an inverse analysis, since it is capable of capturing all of the possible subcritical failure mechanisms. If a fixed shape is pre-selected for the overall TSL, the numbers of failure mechanisms it can represent is fixed beforehand as well.

In this study, the CZMs in Figure 3.4 to Figure 3.7 were proposed to represent the types of failures introduced. Type I and Type IV failures can be simulated using CZM 1 depicted in Figure 3.4. Type I occurs when the concrete adhesion is weaker than both the asphalt adhesion and the

33

aggregate strength, while Type IV is the case when the aggregate strength is the smallest among the three. Regardless, both fractures are quasi-brittle and therefore can be modeled with the bilinear TSL defined in Equation (3.1).

$$T_1 = H(\delta_f - \delta) \cdot T_f \cdot \frac{\delta}{\delta_f} + H(\delta - \delta_f) \cdot T_f \cdot \left[1 - \frac{\delta - \delta_f}{\delta_c - \delta_f}\right] \tag{3.1}$$

where H is the heaveside step function; T_f is the peak traction, psi; δ_f is the separation at the maximum traction and δ_c is the critical separation beyond which the traction is zero.

The IZ also includes an asphalt component, whose deformation is not negligible. Therefore the fracture behavior of asphalt should be considered when establishing the CZM. The fracture of the asphalt during monotonic opening is represented by an exponential TSL in Equation (3.2).

$$T_2 = H(\delta_f - \delta) \cdot T_f \cdot e^{a\left(1 - \frac{\delta}{\delta_f}\right)} \frac{\delta}{\delta_f} + H(\delta - \delta_f) \cdot T_f \cdot \left[1 - e^{b\left(1 - \frac{\delta - \delta_f}{\delta_c - \delta_f}\right)} \frac{\delta - \delta_f}{\delta_c - \delta_f}\right] \tag{3.2}$$

where a and b are the shape factors of the TSL.

Since the asphalt is not fractured in Type I and Type IV failures, it should unload after either the concrete/aggregate interface or the aggregate starts to damage. The loading and unloading paths for the asphalt will not coincide. There should be a difference between the loading and unloading curves induced by the dissipation of energy due to viscous deformation. Therefore, the TSL for unloading should not be described by Equation (3.2). Assuming the initial slope of the unloading curve is the same as the initial slope of the loading curve as shown in Equation (3.3), the TSL for asphalt in a loading-unloading scenario before the peak traction can be defined using Equation (3.4).

$$\frac{dT_2}{d\delta}(\delta = 0) = T_f \cdot \frac{e^a}{\delta_f} \tag{3.3}$$

$$T_3 = H(dT_3) \cdot T_f \cdot e^{a\left(1 - \frac{\delta}{\delta_f}\right)} \frac{\delta}{\delta_f} + H(dT_3) \cdot T_f \cdot e^a \left[e^{-a\frac{\delta_T}{\delta_f}} \frac{\delta_T}{\delta_f} - \frac{\delta - \delta_T}{\delta_f} \right] \qquad (3.4)$$

where δ_T is the separation when the unloading starts and $0 < \delta_T \leq \delta_f$.

Hence, the overall TSL for CZM 1 can be obtained by assembling two root models, namely the bilinear TSL in Equation (3.1) and the loading-unloading curve of asphalt in Equation (3.4), in series, resulting in Equation (3.5).

$$T_{CZM1} = Series(T_1(T_{f1}, \delta_{f1}, \delta_{c1}, \delta), T_3(T_{f3}, \delta_{f3}, T_3'(T_{f1}), a, b, \delta)) \qquad (3.5)$$

where T_3' is the inverse function of T_3, i.e. $\delta = T_3'(T)$ and $T_3'(T_{f1})$.is δ_T in Equation (3.4)
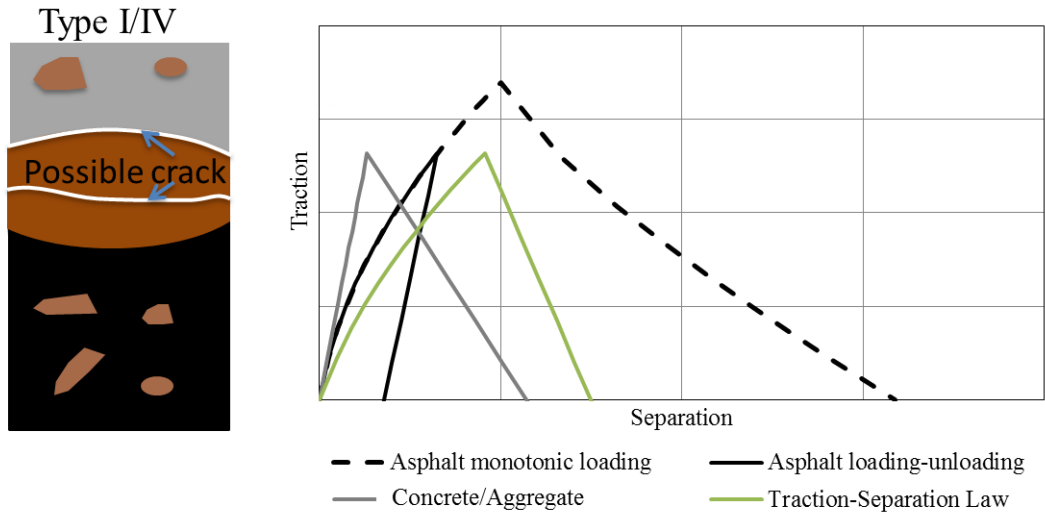
Figure 3.4. Cohesive zone model 1.

Type II failure occurs when the concrete/asphalt matrix adhesion is weaker than the asphalt cohesion. This type of failure is modeled by CZM 2 presented in Figure 3.5. It is assumed that the TSL in Equation (3.2), except with different parameters is also suitable for defining the concrete/asphalt matrix adhesion, considering the adhesion is primarily cementitous in nature. Similar to CZM 1, the overall TSL for CZM 2 is a combination of the concrete/asphalt matrix TSL and the loading-unloading curve of asphalt in series, as defined in Equation (3.6).

$$T_{CZM2} = Series(T_1(T_{f2}, \delta_{f2}, \delta_{c2}, \delta), T_3(T_{f3}, \delta_{f3}, T_3'(T_{f2}), a, b, \delta)) \tag{3.6}$$
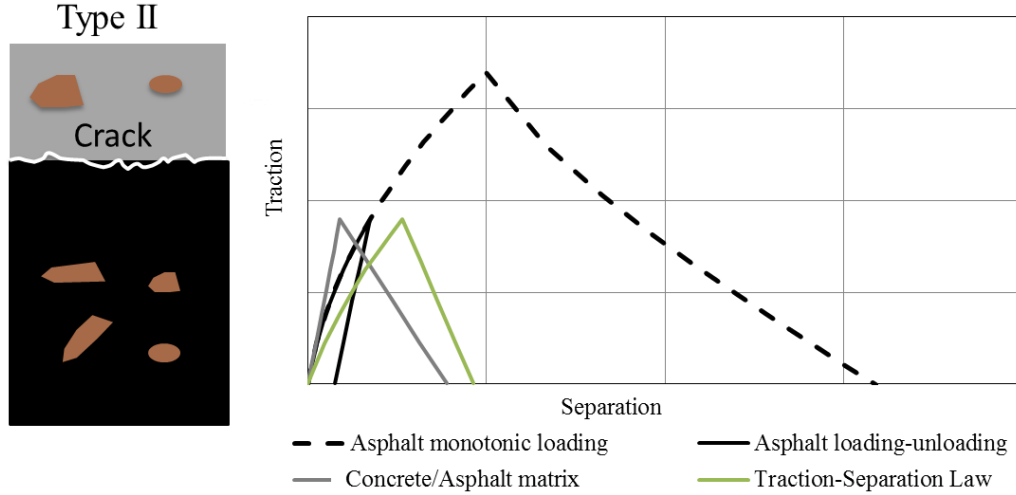
Figure 3.5. Cohesive zone model 2.

CZM 3 shown in Figure 3.6 is used to model Type III and Type V failures. For the IZ in Figure 3.6, cracking will occur in the asphalt when both the concrete-aggregate adhesion and the aggregate cohesion are stronger than the asphalt cohesion. Cracking of the asphalt might occur in the asphalt binder, the aggregates in the asphalt or along the interface between the asphalt binder and the embedded aggregates. However, for simplicity, the same TSL is assumed for all the possible asphalt fractures. Therefore, the overall TSL for CZM 3 can be derived as shown in Equation (3.7), by combining Equation (3.1) that describes the pre-peak loading and unloading behavior of the bilinear TSL and Equation (3.2) that defines the asphalt fracture under monotonic loading.

$$T_{CZM3} = Series(T_1(T_{f4}, \delta_{f4}, \delta), T_2(T_{f3}, \delta_{f3}, \delta_{c3}, a, b, \delta)) \tag{3.7}$$

where δ_c is not an input for T_1 because T_{CZM3} should always be smaller than T_{f4}.
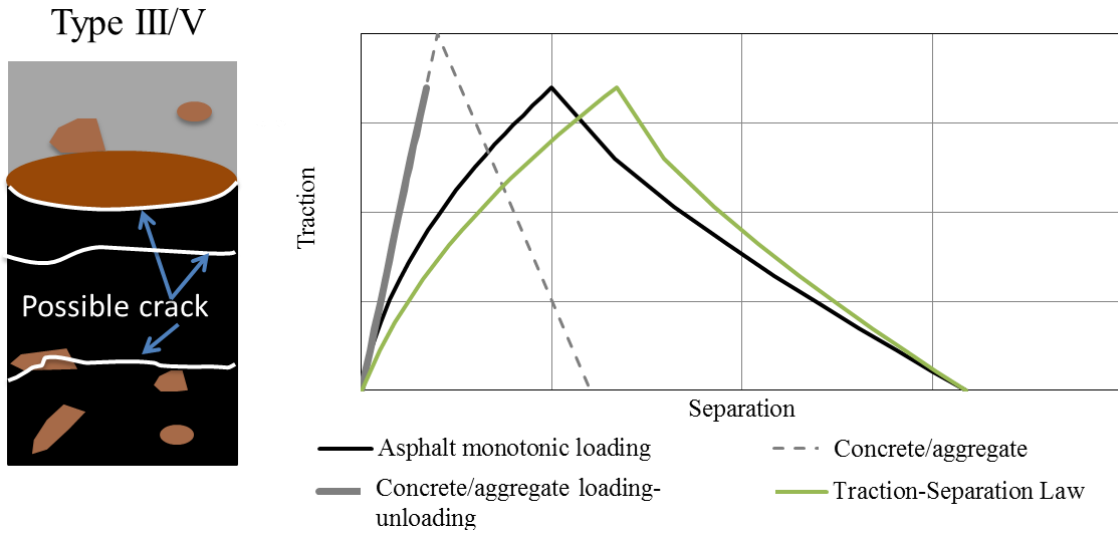
Type III/V

Figure 3.6. Cohesive zone model 3.

CZM 4 in Figure 3.7 also models Type III and Type V failures. Although the IZ in Figure 3.7 is different from that in Figure 3.6 in terms of the composition (similar to CZM 4 there is no aggregate at the concrete/asphalt interface), the two TSLs should present the same shape. The TSL for CZM 4 is defined in Equation (3.8).

$$T_{CZM4} = Series(T_1(T_{f5}, \delta_{f5}, \delta), T_2(T_{f3}, \delta_{f3}, \delta_{c3}, a, b, \delta)) \tag{3.8}$$

Type III/V
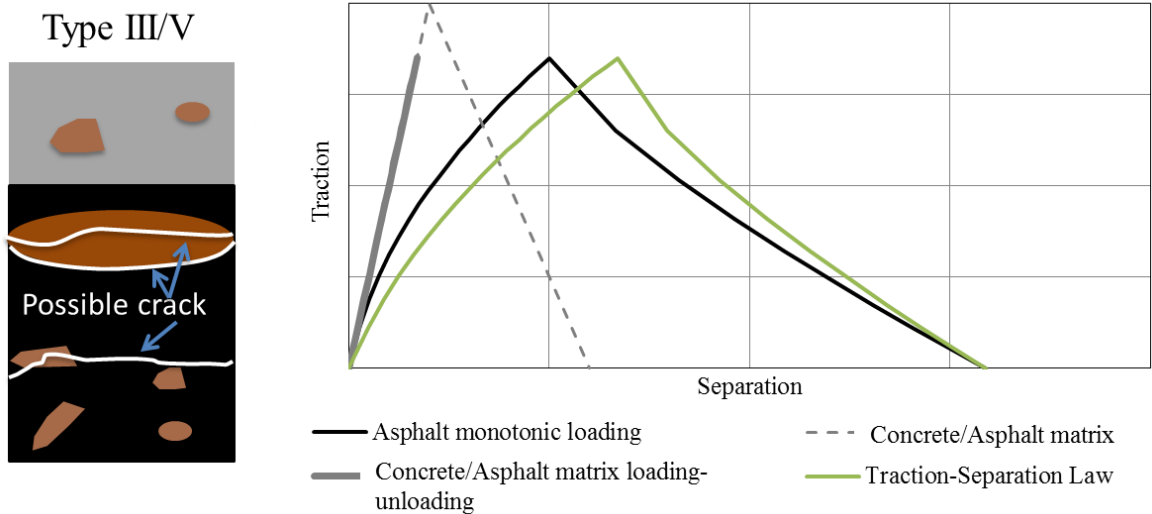
Figure 3.7. Cohesive zone model 4.

The overall traction-separation law for BCOA can be determined, as shown in Equation (3.9), after proportionally combining CZMs 1 to 4 (Equations (3.5) to (3.8)) in parallel.

$$T(T_{fi}, \delta_{fi}, \delta_{cj}, a, b, \delta) = \sum_{k=1}^{4} A_k \cdot T_{CZM\,k} \tag{3.9}$$

where i=1 to 5, j=1 to 3 and A_k is the occupancy of the interface by each failure type, i.e. CZM 1 to CZM 4.

Theoretically, the fifteen fracture parameters in Equation (3.9) could be established based on laboratory fracture tests that target a single root CZM at a time. For example, T_{f2}, δ_{f2} and δ_{c2} can be obtained from a mode I fracture test between aged asphalt matrix and concrete. However, it is nearly impossible to guarantee 100% failure at the interface and furthermore it is extremely difficult to manufacture the specimens, especially at a testable size. In this study, the results from the wedge splitting test are used to determine the fracture properties of the root CZMs. An inverse analysis approach is employed to extract the properties from the complicated WST failure.

3.4 WEDGE SPLITTING TEST SETUP AND RESULTS

The experimental setup for the WST and the BCOA specimen prepared for the WST are presented in Figure 3.8. A small square of material is removed from the central portion of the specimen. The clip gage for monitoring the crack mouth opening displacement (CMOD) is placed in this opening. A notch is cut in the central portion of this region at the interface to establish the location of crack initiation. A guide notch of approximately 6 mm deep is also made on both faces of the specimen to ensure the crack propagates along the interface. Two steel caps with bearings attached are placed on the specimen on each side of the removed region. The axial load applied to the wedge is

transformed to a pair of horizontal splitting forces and a pair of vertical forces at the steel bearings. Since the linear supports were aligned with the steel bearings, the moment causing cracks at the interface is mainly caused by the pair of splitting forces. The recorded results from the WST is the axial load-CMOD curve. The splitting force is related to the axial load as well as the angle of the wedge during quasi-static loading and thus the splitting force-CMOD curve can be derived.
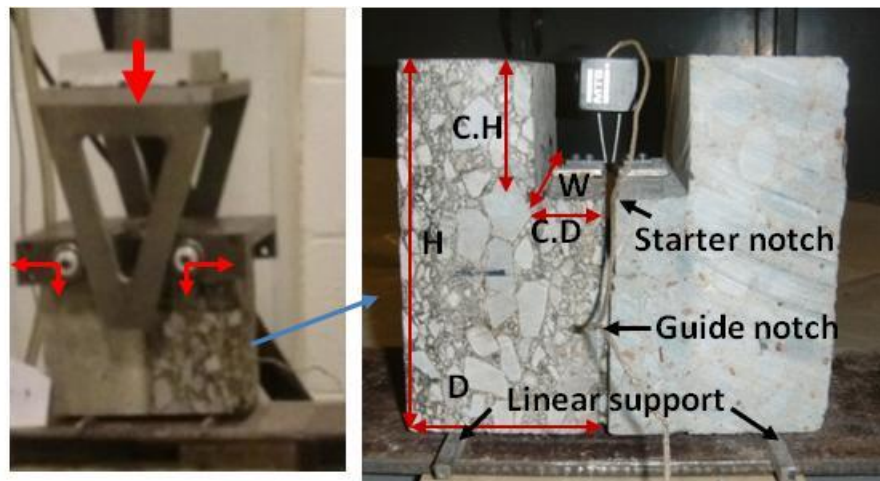
Figure 3.8. Wedge splitting test configuration.

This analysis uses the test results for a dry BCOA specimens tested at room temperature 20 °C. The fracture is induced by a quasi-static loading with a CMOD rate of 0.5 mm/min. The asphalt portion of the specimens were extracted from an in-situ asphalt pavement. A section of the asphalt pavement has milled texture while the rest was unmilled so the effect of asphalt surface texture could be studied. The sand patch test (ASTM-E965-96) was conducted to quantify the asphalt roughness in terms of a characteristic depth. A rougher surface is indicated by a larger value of the characteristic depth. The depth (D in Figure 3.8) of the unmilled HMA specimens is 100-125 mm, as compared to 75-90 mm for the milled specimens. The height and width of the asphalt specimens are both 150 mm. The nominal height and depth of the cut are 50 mm and 25 mm, respectively. A standard depth for the initial notch is 12 mm, with the exception of the

specimens made with different notch depths to study the effect of flaw size on the interfacial fracture. Representative WST results are presented in Figure 3.9.
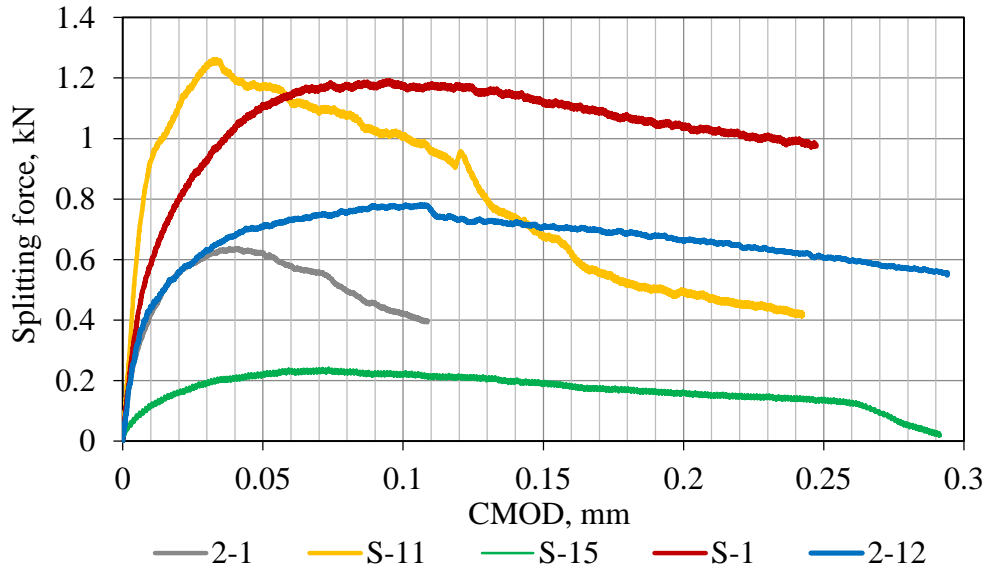
Figure 3.9. Typical splitting force-CMOD curves from the wedge splitting test of BCOA.

Specimens 2-1, S-11 and S-15 are unmilled. S-11 and S-15 share the same dimensions and similar asphalt roughness, as seen in Table 3.2. The difference in load-CMOD behavior between them is because the initial notch depth for S-15 is 44% of the nominal contact length (H-C.H., as defined in Figure 3.8) relative to 11% for S-11. Specimen 2-1 has a surface roughness of only 0.5 mm as compared to 0.8 mm for S-11, which might explain the difference between 2-1 and S-11. For the two milled specimens S-1 and 2-12, S-1 exhibited a much larger proportion of Type III failure (failure of the asphalt matrix), than 2-12. The only apparent difference between them is that the concrete of S-1 is 25% thinner than 2-12.

The dependence of the WST results on the specimen size, i.e. specimen thickness and initial notch depth, implies that the size of the fracture process zone for the interfacial cracks is so large that it is more or less comparable to the specimen size. Therefore, the effect of specimen size

should also be studied in addition to the asphalt roughness, when using the WST results to determine the fracture properties of the cohesive zone models.

Table 3.2. Dimensions of the WST specimens shown in Figure 3.9.

			2-1	S-11	S-15	S-1	2-12
Dimensions as illustrated in Figure 3.8, mm	Asphalt	D	97	100	93	67	65
		H	151	140	139	140	146
		C.D	35	30	28	26	27
		C.H	52	47	45	48	47
		W	145	148	145	150	145
	Concrete	D	110	85	87	58	80
		H	153	141	141	140	145
		C.D	28	23	28	28	29
		C.H	51	48	45	49	45
		W	145	148	145	150	145
Notch depth, mm			14	12	43	18	17
Contact area, mm^2			12,521	11,953	7,595	11,087	12,011
Interface roughness based on sand patch test, mm			0.5	0.8	0.8	1.9	1.7

3.5   FINITE ELEMENT IMPLEMENTATION FOR THE CZM

The finite element package ABAQUS Standard Ver. 6.11 was used to implement the cohesive zone models. A BCOA specimen in the WST setup is modeled and presented in Figure 3.10. Concrete and asphalt were modeled as homogenous materials. Concrete was treated as an elastic material. The elastic modulus and Poisson's ratio for the concrete are 28 GPa and 0.2, which were obtained from laboratory testing complying with ASTM C469. Visco-elastic properties were considered for the asphalt and AASHTO T 342-11 was followed to determine the dynamic modulus of the asphalt specimens at three temperatures and four frequencies. The master curve at a reference temperature of 20 °C was then established and presented in Equation (3.10).

41

$$\log(E^*) = -1.2427 + \frac{2.6173}{1 + \exp(-0.7778 - 0.3749\log(f))} \tag{3.10}$$

where E^* is the dynamic modulus of the asphalt mixture, GPa and f is the loading frequency, Hz.
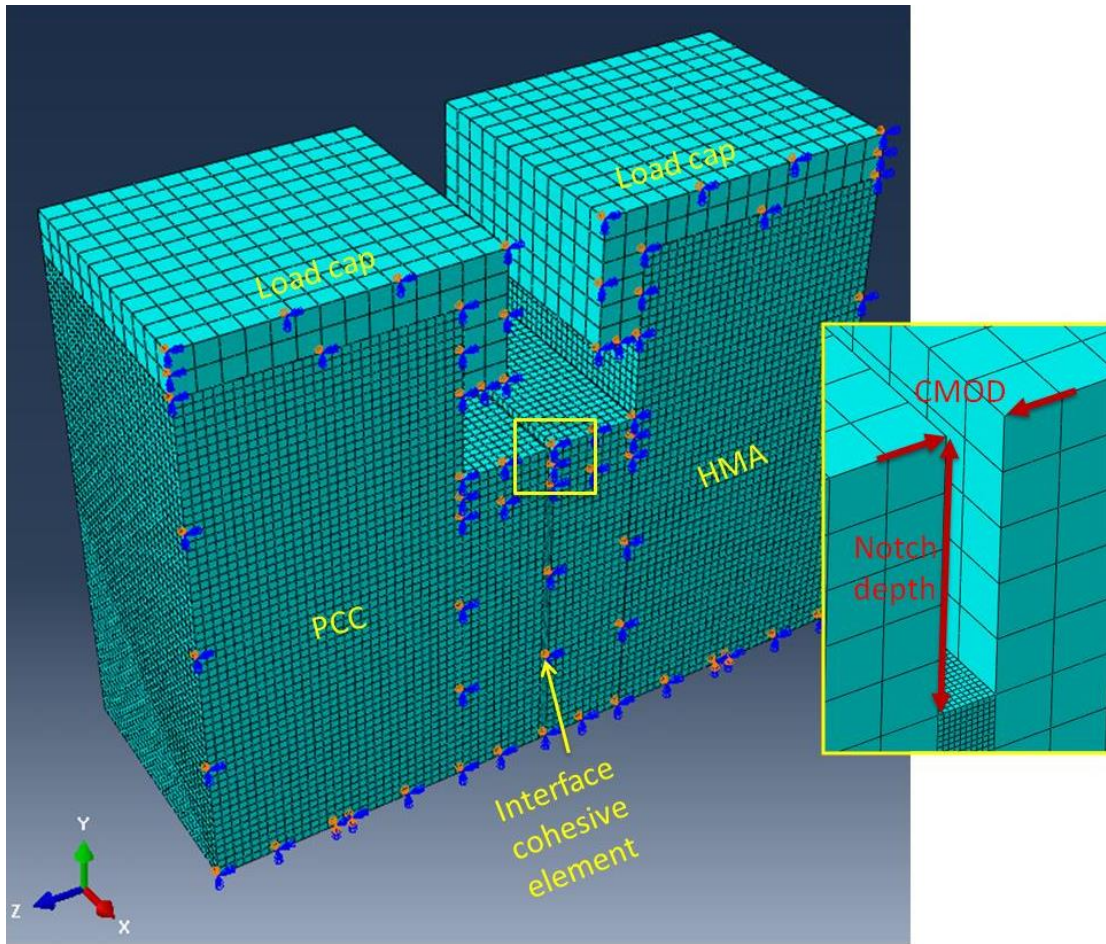
Figure 3.10. Finite element implementation of the cohesive zone model of BCOA in the WST setup.

The interface was modeled with the overall cohesive zone model described by Equation (3.9). In ABAQUS, strain instead of separation is used to define the critical displacement of a CZM. Therefore, the thickness of the cohesive zone is set constant, resulting in a one-one mapping between the required strain and the separation defined in Equation (3.9). Multiple mechanisms are

available in ABAQUS to define the strain softening of a CZM. Employed here is the damage-displacement relation that can be converted from a TSL. The damage variable in such a relation is defined by Equation (3.11), where the stiffness can be obtained by dividing the current tensile stress with the current separation strain.

$$E_{n,s,t} = (1 - D)\bar{E}_{n,s,t} \tag{3.11}$$

where $\bar{E}_{n,s,t}$ are the stiffness components at the normal and shear directions of the interface elements, predicted by the linear traction-separation law without damage, and D is the scalar damage variable.

Only half of the specimen was simulated due to the symmetry. The convergence of the model in terms of both mesh size and time step was validated. Using the model, the splitting force-CMOD curve for a specific specimen can be simulated for a specimen with any given TSL.

3.6 INVERSE ANALYSIS FOR OBTAINING THE CZM PARAMETERS BASED ON WST RESULTS

An inverse analysis was used to determine the parameters of the CZM including the TSL. The inverse analysis can be described by the optimization problem in Equation (3.12). The goal is to minimize the error between the predicted P-CMOD curve and the measured P-CMOD curve. The predicted P-CMOD curve is obtained from the finite element model with CZMs generated according to Equations (3.1) to (3.9).

$$\underset{(T_{fi}, \delta_{fi}, \delta_{cj}, a, b)}{Min} \sum_{n=0}^{N} \left[P\left[T\left(T_{fi}, \delta_{fi}, \delta_{cj}, a, b, A_k \right), CMOD_n \right] - P_{meas}(CMOD_n) \right]^2 \tag{3.12}$$

Subject to (1) $0 < \delta_{fi} < \delta_{cj}$ for $i = 1$ to 3 and $i = j$

(2) $0 < \delta_{fi}$ for $i = 4$ and 5

(3) $0 < T_{fi} < T_{f3} < T_{fi+3}$ for $i = 1$ and 2

(4) $\sum_{k=0}^{4} A_k = 1$

where $P[T, CMOD_n]$ stands for the predicted P-CMOD relationship for a given TSL; $P_{meas}(CMOD)$ is the measured P-CMOD curve from a WST and N is the number of measurements made during the WST.

In Equation (3.12), A_k the percentage of CZM 1 to CZM 4 was quantified from the image analysis of the fractured interface, such as those shown in Figure 3.3. On a grey scale, pixels that are dark, medium and light indicate asphaltic, aggregate and cementitious failures, respectively. The fractured interface can be so sophisticated that pixel-color analysis alone was inadequate. For example, CZM 3 and CZM 4 both include dark pixels and they cannot be distinguished unless the asphalt residue is scratched off to examine the existence of aggregates. Due to the complexity of the fractured interface and the variation in aggregate colors, manual inspection of the specimens was also conducted to aid the image analysis in differentiating the failure types.

Following the above optimization procedure, the genetic algorithm toolbox in MATLAB (MATLAB, 2013) was used to calculate the parameters for each CZM, i.e. $T(T_{fi}, \delta_{fi}, \delta_{cj}, a, b)$. As an example, the parameters for Specimens 2-01 and S-01 in Figure 3.9 were determined and presented in Table 3.3.

In Table 3.3, the peak traction for two of the CZMs, namely T_{f4} and T_{f5} cannot be determined since the asphalt cohesion T_{f3} in Equations (3.7) and (3.8) is weaker and thus more dominant in the two models. As a result, the optimization was not sensitive to T_{f4} and T_{f5} and

therefore they could not be inversely determined. For the same reason, the ultimate displacement

of δ_{c4} and δ_{c5} could not be determined either.

The overall TSLs for 2-01 and S-01 shown in Figure 3.11 were generated using the

parameters from Table 3.3. They resulted in a prediction of the splitting force-CMOD curve that

is in good agreement with the measurements, as is demonstrated in Figure 3.12.

Table 3.3. Parameters for the cohesive zone models.

	S-1	2-1	Mean of unmilled n=6	Mean of milled n=5
T_{f1}, kPa	434	131	241	289
T_{f2}, kPa	262	76	158	145
T_{f3}, kPa	503	214	338	427
T_{f4}, kPa	N/A	N/A	N/A	N/A
T_{f5}, kPa	N/A	N/A	N/A	N/A
δ_{f1}, mm	0.003	0.0015	0.001	0.00275
δ_{f2}, mm	0.04275	0.00825	0.0175	0.02625
δ_{f3}, mm	0.00005	0.00005	0.00025	0.00025
δ_{f4}, mm	0.000125	0.0005	0.0005	0.00025
δ_{f5}, mm	0.0045	0.0001	0.00075	0.00125
δ_{c1}, mm	0.04625	0.05225	0.03625	0.11175
δ_{c2}, mm	0.0575	0.0525	0.05025	0.099
δ_{c3}, mm	0.2425	0.057	0.14525	0.211
δ_{c4}, mm	N/A	N/A	N/A	N/A
δ_{c5}, mm	N/A	N/A	N/A	N/A
a	0.57	0.82	0.91	1.19
b	0.24	0	-0.13	-0.2
A_1	26%	3%	23%	23%
A_2	26%	7%	18%	22%
A_3	42%	22%	43%	24%
A_4	6%	68%	16%	31%
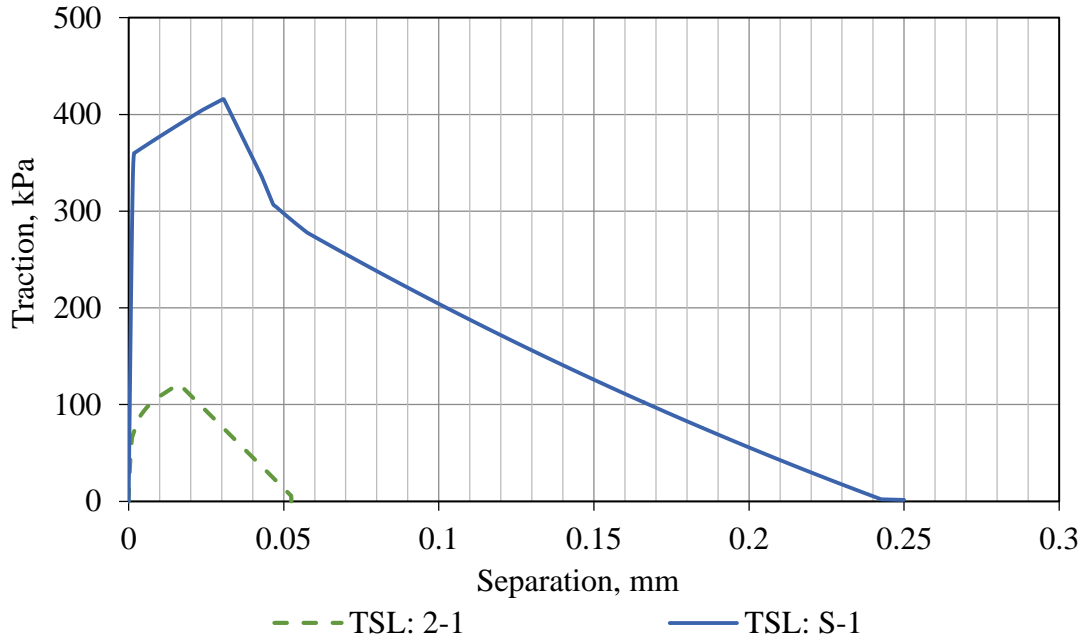
Figure 3.11. Effective traction-separation laws for BCOA specimens 2-01 and S-01.
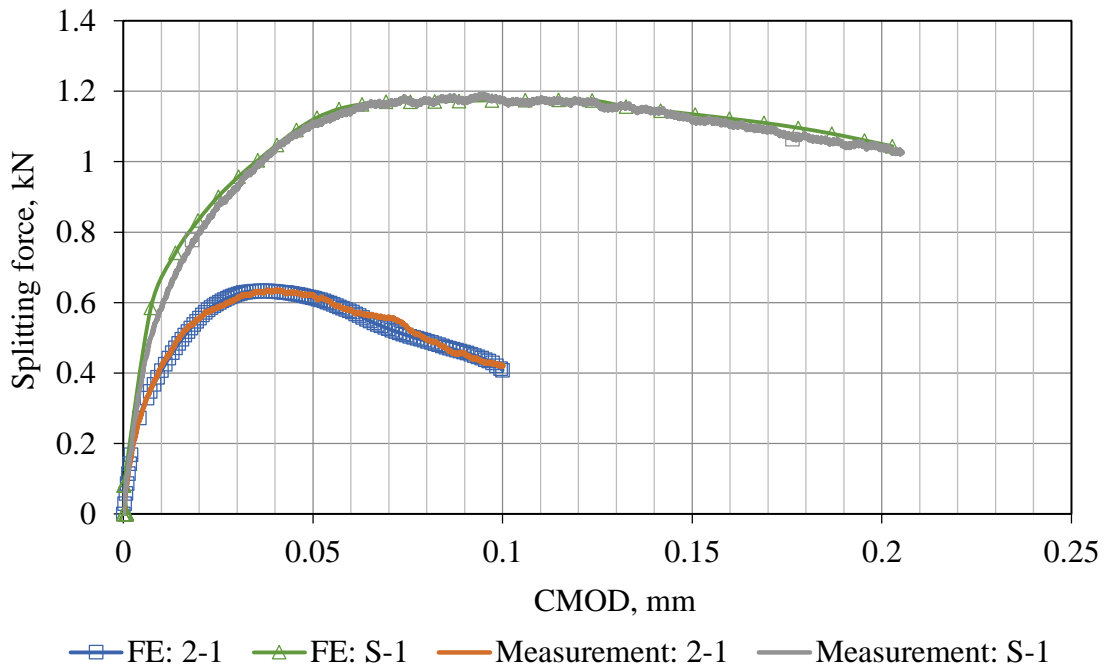
Figure 3.12. Comparison of predicted load-displacement curves from CZM modeling and

laboratory measurements.

46

The same inverse analysis was carried out for the rest of the specimens. The mean values of the parameters were calculated for each root CZM, the result of which is presented in Table 3.3. The peak tractions are comparable between the milled and unmilled specimens but the separation, especially the critical separation, for the milled specimens is 1.5-3 times larger than the separation for unmilled specimens. This is due to the fact that the thickness of the cohesive zone was held constant. Assuming the interface thickness is proportional to the asphalt roughness and considering the roughness for milled specimens (1.5-2.25 mm) is about 2-3 times larger than for the unmilled specimens (0.5-0.75 mm), it can be concluded that the critical strain for each root CZM is similar between milled and unmilled specimens. Although the milling resulted in an increased interfacial bond, the magnitude of the increased bond strength, characterized by T_{f4} and T_{f5}, is not reflected by the interfacial fracture and thus cannot be determined. Instead, the milling forced the fracture into the adjacent asphalt, and as a result the IZ became thicker. Therefore, the increase in bond strength due to milling is not obvious from the fracture tests at room temperature. The milling contributes to the interfacial fracture by creating a thicker IZ and a larger percentage of the failure in asphalt (Type III). In Table 3.3, it shows that the percentage of CZM 3 for milled specimens significantly decreased due to a decreased amount of aggregate pullout and the percentage of CZM 4 significantly increased due to an increased amount of aggregate/asphalt fracture.

The overall CZM for the milled specimen was the result of superimposing the CZMs presented in Figure 3.13. Since CZMs 3 and 4 both represent asphalt failures and they are extremely similar in shape, only CZM 3 is presented. From Figure 3.13, one can learn that the damage/cracking accumulation occurred in five phases. In phase I, no damage occurs. In phase II (before peak traction of the effective overall TSL), damage occurs for the two CZMs with short critical displacements, but the overall traction keeps increasing until the damaging rate of CZM 1

and CZM 2 exceeds the rate of traction gain from CZM 3 and CZM 4. In phase III, the overall

traction drops rapidly as the separation increases as all the CZMs accumulate damage during this

phase. Phase IV is where all the cementious bonds which will break have broken and any further

fracture is dominated by the asphalt fracture. In the last phase, a crack is formed, as indicated by

the zero traction. In Figure 3.13, it is obvious that such a five-phase failure can be approximated

by a trapezoidal TSL with a bilinear softening curve.
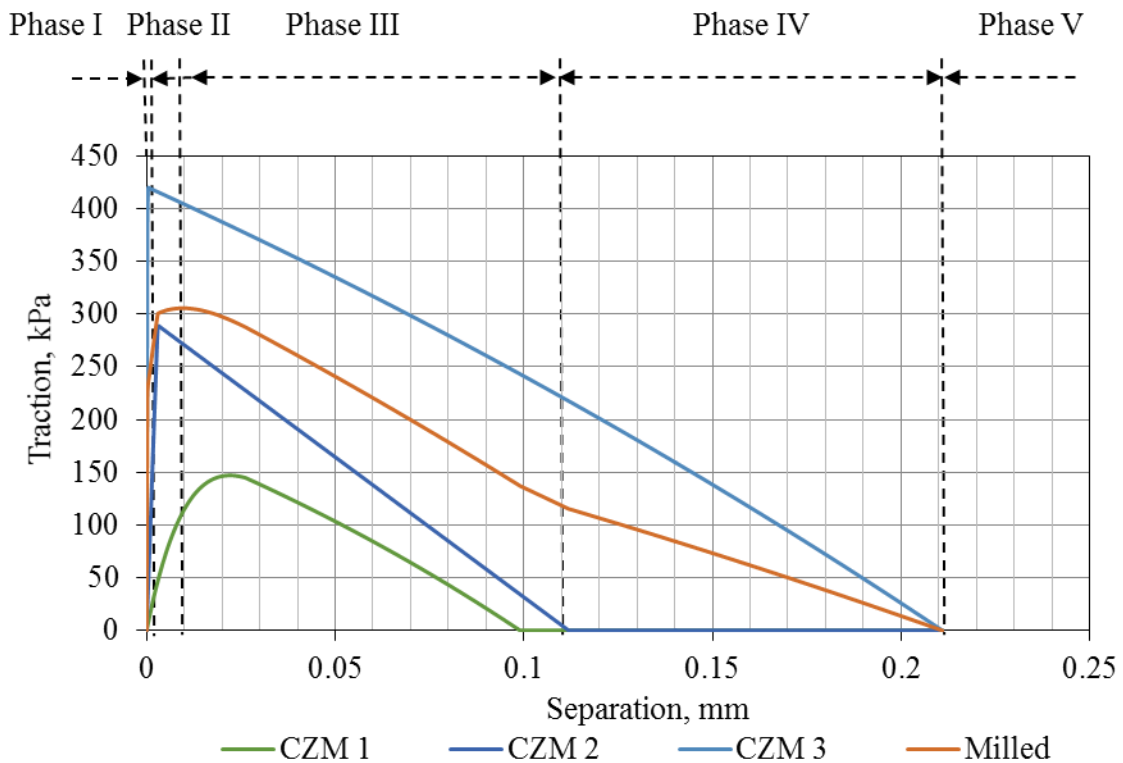
Figure 3.13. Traction-separation law for the cohesive zone models.

The effect of asphalt texture on the peak traction and fracture energy of the effective TSLs

was studied. This was done by plotting the overall fracture energy, i.e. the area under a TSL curve,

as well as the peak traction for each specimen against their asphalt roughness. Figure 3.14 shows

no definite relation between the peak traction and the asphalt roughness. However, the fracture

energy increases with the HMA roughness. This agrees with the previous conclusion based on

Table 3.3 that milling resulted in a thicker IZ shifting the interfacial fracture into the asphalt but not increasing the peak traction. This again implies that the bond strength is not a suitable parameter for evaluating the effectiveness of milling.
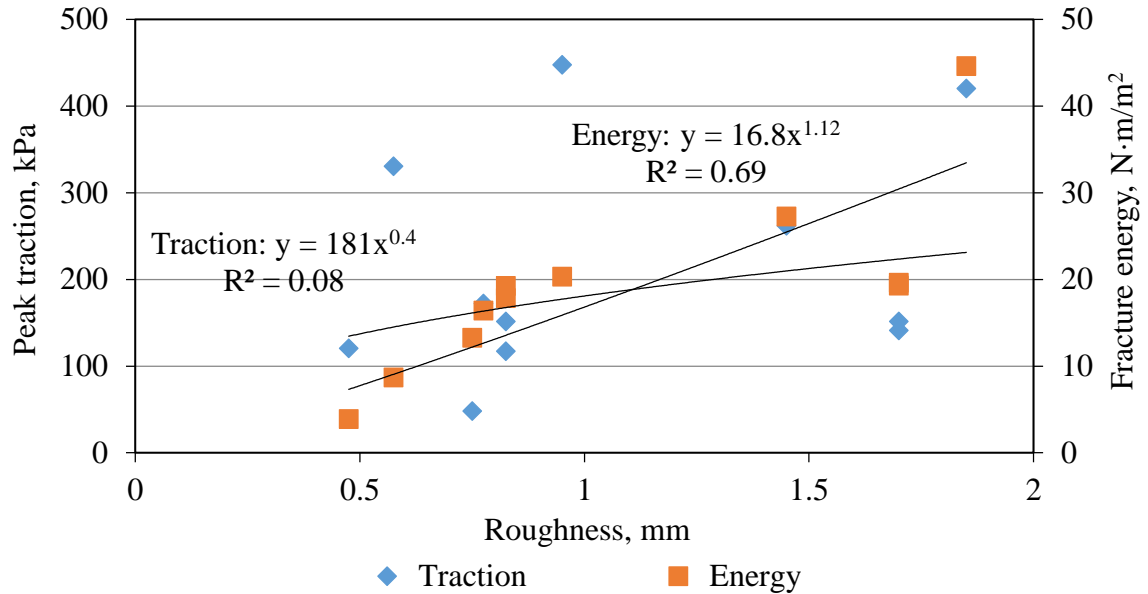
Figure 3.14. Influence of the HMA roughness on the peak traction and fracture energy of the cohesive elements.

The size effect of the WST was also studied. Figure 3.15 shows the relationship between the fracture energy and peak strength with the asphalt depth. For both milled and unmilled specimens, a greater asphalt depth appears to possibly relate to a lower fracture energy. This is because that the interfacial crack process zone is relatively small when the asphalt thickness is large, which results in a more brittle failure with smaller fracture energy. Similarly, there is a relatively large crack process zone when the asphalt is milled or the asphalt is thin, resulting in larger fracture energy. There is no definite correlation between the peak strength and the asphalt depth.
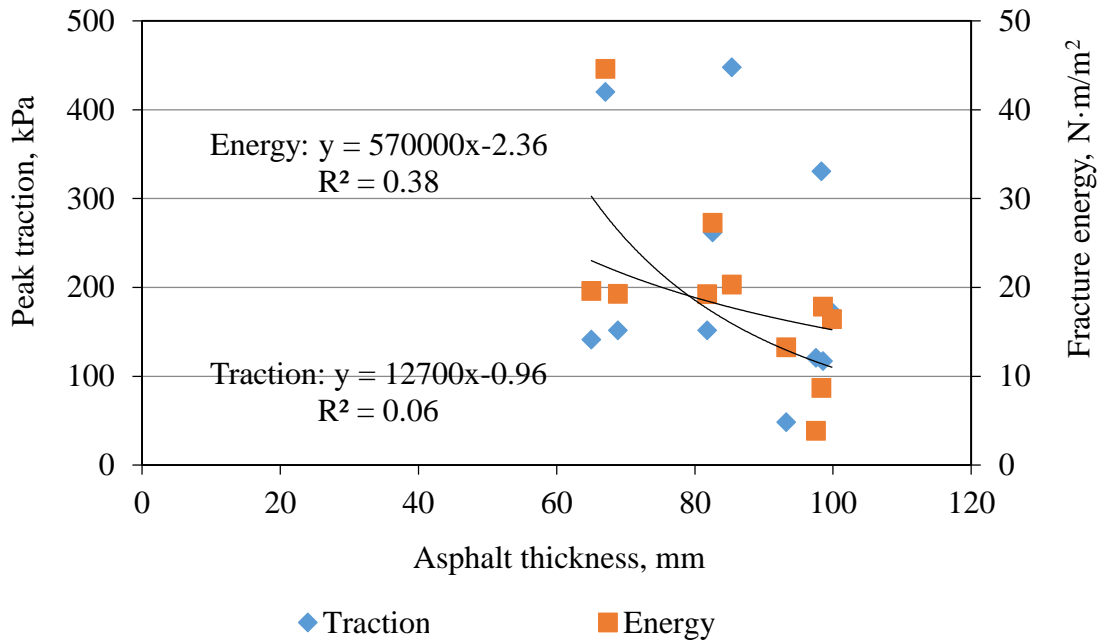
Figure 3.15. Influence of the asphalt depth on the peak traction and fracture energy of the

cohesive elements.

The peak traction as well as the fracture energy was plotted against the flaw size (initial notch depth) in Figure 3.16. There is no clear evidence that the fracture energy is a function of the initial flaw size. However, the peak traction shows an inversely proportional relationship with the flaw size. In WST, the test configuration results in a compression zone at the bottom of the interface. Since damage is unlikely to happen in this compression zone, its upper bound defines the lower bound of the damage developing zone. In the finite element model, it was observed that the size of this compression zone was consistently 15-20% of the nominal contact area at the beginning of the WST and it gradually diminished when the fracture approached the bottom of the interface. Therefore, a deeper initial notch would result in a smaller damage developing zone and thus a smaller peak traction force. On the other hand, the fracture energy is dominated more by the thickness of the IZ besides the depth of the damage developing zone along the interface. In Figure 3.16, it is also noteworthy that the effect of the flaw size almost disappears when the initial notch

depth is less than 10%. Therefore, only the specimens with an initial notch of 10% or less should

be used for the inverse analysis of fracture properties for the CZMs.
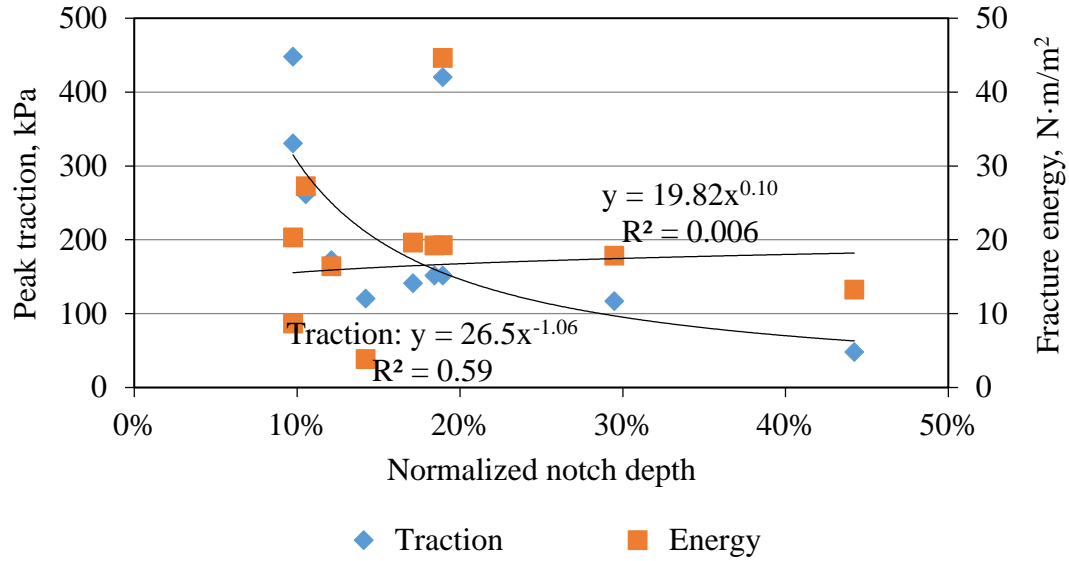
Figure 3.16. Influence of the initial flaw size on the peak traction and fracture energy of

the cohesive elements.

3.7   CONCLUSIONS

In this study, a cohesive zone model based on the superimposition principle was used to model the

interfacial fracture of BCOA. Fractured BCOA specimens were first examined and four major

types of subcritical failure were identified, namely the failure of concrete adhesion to asphalt

matrix, the failure of concrete adhesion to exposed/crushed aggregate, aggregate breakage/pullout

and asphalt fracturing. Four root CZMs were proposed to simulate the subcritical failures. The

complicated overall fracture behavior of the interface can then be simulated by simply

superimposing the root CZMs.

The fracture properties of the root CZMs were obtained based on the inverse analysis of wedge splitting test results. The properties are material dependent and independent from the composition of the interface, i.e. the milling effect, and they can be used to model the debonding of BCOA on different scales.

In general, the overall CZM for BCOA can be approximated by a trapezoidal traction-separation law with bilinear softening. An analysis of the properties for the overall CZM revealed that the peak traction decreases with increased initial notch depth until the initial notch depth dropped to 10% or less of the nominal contact length. The total fracture energy is a function of the asphalt roughness and asphalt thickness. A milled specimen with thin asphalt often presents a relatively thicker interfacial transition zone and thus results in the fracture of the asphalt. Such a type of fracture is less brittle and presents higher fracture energy.

In the experiment, no bond was observed where milling left deep grooves into the asphalt. This is believed due to the relatively large depth/width ratio of the grooves providing a shield against concrete penetration and the deposit of debris and dusts in these grooves breaking the concrete bond. When paving concrete in the field, attention should be paid in order to achieve efficient vibration and thorough cleaning so that the concrete can penetrate into such grooves and form a good bond with the asphalt.

4.0 BASELINE-DEPENDENT TRANSIENT WAVE METHOD FOR QUANTIFYING THE INTERFACE DEBONDING OF BONDED CONCRETE OVERLAY OF ASPHALT UNDER FATIGUE LOADING

4.1 BACKGROUND

Bonded concrete overlay of asphalt (BCOA) is a viable technique for rehabilitating distressed asphalt pavements. It is a more durable solution for highways and city intersections where the constant maintenance for asphalt is less desirable. BCOA, especially ultra-thin BCOA that is 100 mm or thinner, is also less material demanding and can be more cost effective when compared to unbonded concrete overlays, especially when overhead clearance issues are a concern. As a result, BCOA has gained increasing popularity over the past two decades (Cole et al., 1998 and Roesler et al, 2008).

The key to a successful BCOA is the bond between the concrete overlay and the underlying asphalt. When the bond is effective, the neutral axis of the overlay is shifted lower towards the asphalt resulting in lower tensile stress in the concrete and thus making it possible for the thin overlay to carry large amounts of traffic. Over the past decade, researchers observed premature failure of BCOAs from the debonding between the concrete and the asphalt (Vandenbossche and Fagerness, 2002, Nelson and Rasmussen, 2002; Vandenbossche, 2005). The cracking of the overlay was mainly found at the corners or wheelpaths of the overlay slabs, where the interface debonding initiates owing to the structural singularity and develops under repeated traffic loading. As the cracking potential is a function of the shape and size of the debonding, it is critical to

53

understand the growth of the interface debonding under fatigue loading for design and construction purposes.

In this study, BCOA slabs were tested under fatigue loading using the Accelerated Loading Facility (ALF) housed at the University of Pittsburgh to recreate the interface debonding of BCOA due to traffic. One challenge of the experiment is to quantify the size of debonding during the fatigue, without introducing additional damage to the tested slabs. For this purpose, a nondestructive method was developed based on the transient wave analysis. In the following sections, the theoretical basis for the method is first discussed, followed by the numerical analysis and laboratory validation of the method. The method was then applied to detect interface debonding during the ALF testing, the results of which were compared to a deflection-based nondestructive method.

4.2   THEORETICAL BASIS FOR TRANSIENT WAVE ANALYSIS

The transient analysis of a structure refers to exciting it with a short-duration small-amplitude energy and then analyzing the structure's response to the event in order to extract information regarding the inside/underlying defects. It has served as the common basis for various nondestructive evaluation methods, such as the ground penetration radar method (Maierhofer, 2003), the ultrasonic method (In, 2013) and the impact-echo method (Sansalone and Carino, 1989). In this study, the impact-echo setup was employed due to the following benefits. First, the test is relatively cheaper, safer and more mobile to transport to the in-situ test locations compared to the other methods. Second, the test yields acceptable accuracy. The generated transient wave has a

wave length of a few centimeters (Schubert and Köhler, 2008), which is ideal for detecting defects

larger than this dimension while being indifferent to inhomogeneity like aggregates and voids.

4.2.1 Impact-echo method

The impact-echo test gained its popularity in detecting defects in concrete slabs in the late 1980s

(Sansalone and Carino, 1989; Lin et al. 1990; Cheng and Sansalone, 1993). In an impact-echo

setup, a mechanical impact is applied to the surface of concrete by various methods, including

dropping a small weight. A piezoelectric transducer coupled to the concrete close to the impact

senses the deformation and generates electrical charges and a data logger records the voltage signal

in time domain.

The wave form recorded in time domain is often converted to the frequency spectrum

through the Fourier transform, where a peak frequency, according to Sansalone and Carino (1989),

can be determined as a function of the thickness of the concrete slab as shown in Equation (4.1).

$$f_t = \frac{c_p}{2h} \tag{4.1}$$

where f_t is the peak (thickness-mode) frequency, Hz; c_p is the velocity of the longitudinal

wave, m/s and h is the thickness of the concrete slab, m. The velocity of the longitudinal wave can

be estimated using Equation (4.2), knowing the Young's modulus E, Poisson's ratio v, as well as

the density of the concrete ρ.

$$c_p = \sqrt{\frac{E}{(1 - v^2)\rho}} \tag{4.2}$$

The resonance of the concrete slab at this frequency can be understood as the result of the

longitudinal wave reflecting multiple times between the top and the bottom of the slab. When there

is a defect under the impact, reflections between the top of the concrete and the defect will occur, resulting in a new peak in the frequency spectrum. When there is a defect at a depth shallower than bottom of the concrete, a higher peak frequency can be expected and the depth of the defect can also be determined using Equation (4.1).

For a composite slab, such as a BCOA, the thickness frequency corresponding to the total thickness can be calculated according to Sansalone and Carino (1989), as shown in Equation (4.3).

$$f_c = \frac{1}{\frac{2h_1}{c_{p1}} + \frac{2h_2}{c_{p2}}} \tag{4.3}$$

where the subscripts 1 and 2 represents concrete and asphalt, respectively.

However, for the BCOA, there might not be a noticeable thickness frequency excited corresponding to the depth of the interface until the bond breaks at the interface. This can be proved by examining the reflection ratio of the incident wave at the interface as is defined in Equation (4.4).

$$R = \frac{Z_2 - Z_1}{Z_2 + Z_1} = \frac{c_{p2} \cdot \rho_2 - c_{p1} \cdot \rho_1}{c_{p2} \cdot \rho_2 + c_{p1} \cdot \rho_1} \tag{4.4}$$

where Z is the acoustic impedance of the medium. When the wave from the concrete meets a bonded interface, the reflection ratio is only -0.3 to -0.5 assuming that asphalt and concrete have the same density and the Young's modulus for asphalt is approximately 1/10 to 1/4 of the concrete. On the other hand, since the acoustic impedance for concrete is approximately 20 million times larger than that of air (Carino, 2001), the reflection ratio is approximately -1 for a debonded interface (the negative sign of the reflection ratio implying the change in phase for the wave).

4.2.2 Scanning impact-echo

While a single impact-echo test can reveal the existence of interface debonding by looking up new peaks other than that related to the total thickness in the frequency spectrum, the size of the debonding is usually determined by conducting many impact-echo tests in a grid pattern, which is referred to as a scanning impact-echo test. Based on the obtained thickness-mode frequencies, the depth contour of the defects can be generated using Equation (4.1). This methodology has been applied for the defect/debonding detection in both concrete (Zhu and Popovics, 2007) and asphalt (Heitzman et al., 2013). Based on the review of these applications, a conclusion might be drawn that the scanning impact-echo method is adequate to qualitatively evaluate the occurrence of interface debonding. However, it does not present the ability to quantify the debonding size with the precision needed in this study.

The precision of the scanning impact-echo method depends on 1.) the accuracy of identifying the thickness-mode frequency corresponding to the interface debonding and 2) the resolution of the scanning grid. As a matter of fact, the major difficulty always lies in how to identify the thickness-mode frequency among other resonant peaks, such as those due to Rayleigh waves or flexural-mode resonance. Cheng and Sansalone (1993) demonstrated based on their numerical study that an impact over a large, shallow defect in concrete would excite multiple flexural-mode vibrations. As a result, the impact-echo method was only effective when the impact-sensor pair was at an optimum distance from the defect, since the frequency corresponding to the defect depth was not obvious when the impact was either directly above or too far away from the defect. Furthermore, it was found that the resonant thickness-frequency for the defect was smaller for a larger defect, which might be due to the reduced effective stiffness of the concrete with a larger defect. Motivated by the demand to identify the resonant thickness-mode frequency, various

signal processing techniques have been developed, based on cross-spectral correlation (Medina and Garrido, 2007), temporal windowing and band-pass frequency filters. Furthermore, in recognition of the dispersion nature of propagating transient waves in concrete, time-frequency analyses, such as the wavelet method (Yeh and Liu, 2008) and Hilbert-Huang Transform (Bouden et al. 2012) were also employed in order to isolate different wave modes and guide the determination of the thickness-mode resonant frequency. Despite the improved capability in isolating the thickness-mode, variability in calculating the depth contours still exists because the material properties such as Poisson's ratio and the effective stiffness of the structure that is a changing function of the debonding size cannot be accurately determined for each location of impact. This variability can be reduced by using a refined scanning interval but with a practical limit, i.e. the size of the impact-sensor pair. From the data processing perspective, data fusion technique was proposed to sharpen the defect boundary by fusing the signals from the same sensor due to different impacts (Xie et al., 2012), or from multiple sensors (Zhang et al., 2012).

4.2.3 Baseline-dependent transient wave method

Although the impact-echo test setup is promising, the traditional means of interpreting the test data, namely identifying the thickness-mode resonant frequencies and determining the defect boundary based on scanning impact-echo, cannot be used to quantify the interface debonding for BCOA with the resolution required. This is largely because the traditional analysis only relies on one wave mode to obtain the defect information. After all, the thickness-mode resonance is only one of the many responses from an impacted structure. The Lamb-wave based explanation for the thickness-mode frequency identified by the impact-echo method was provided by Gibson and Popovics (2005). The thickness-mode frequency was proved to be equal to the cutoff frequency

for the S1 Lamb wave, i.e. at zero group velocity. The reason for the resonance at this frequency was because the excitability of the S1 Lamb wave was much greater than all the other modes at the cutoff point. On the other hand, for propagating Lamb waves in concrete plates, most of the energy is carried by the fundamental S0 and A0 waves. Schubert and Köhler (2008) showed an example based on a finite element analysis where over 90% of the energy due to the mechanical impact was transmitted through the surface and shear waves.

There has been a tremendous amount of research in developing the transfer function that relates the wave modes to the characteristics of the defects. It has been demonstrated that the Lamb waves of various modes interact with defects and thus carried on the information such as the shape, size and location (Guo and Cawley, 1993; Alleyne and Cawley 1992; Koh et al. 2002, Su et al., 2006 and Ng and Veidt, 2011). Even the surface wave has been used for the detection of defects at relatively shallower depths based on the propagation of its low frequency components (Rose et al., 1990; Al-Hunaidi, 1996; Aggelis and Shiotani, 2007).

The research on mode-dependent transfer functions was driven by the need of conducting defect detection without any knowledge on the previous health condition of the structure. For the quantification of interface debonding for BCOAs, a baseline scan could be obtained at the beginning of the fatigue loading, which provides the possibility to avoid the complicated mode-dependent analysis. In the following section, a baseline-dependent transient wave method is presented, where a measureable characteristic parameter is found to proportionally relate to the area of interface debonding for BCOAs. The method developed was then applied to the accelerated loading experiment, where the parameter was updated after each loading period by conducting a transient wave scan of the BCOA and comparing it to the baseline scan. The obtained estimation was compared with the measurement from a destructive examination conducted at the end of the

test. A good agreement was obtained between the two methods. The estimation by the transient wave method also matches the predictions from a deflection-based nondestructive evaluation.

4.3   FINITE ELEMENT ANALYSIS

A finite element model was developed using ABAQUS Standard Ver. 6.11 to study the transient wave propagation in a partially bonded BCOA plate with the dimensions illustrated in Figure 4.1. A 2-D model was used in order to achieve the desired mesh fineness at a reasonable computational cost.
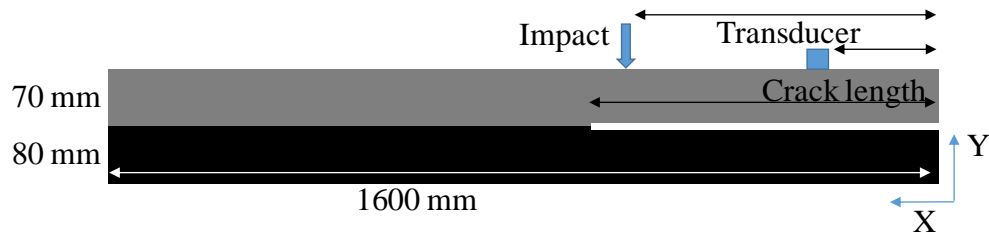
Figure 4.1. Finite element model to study the transient wave behavior in a partially bonded BOCA slab.

The length of the BCOA slab was 1.6 m, similar to the slab size used in the practice. Free boundary conditions were used to simulate the edge reflections at the slab joints. A convergence test was conducted to determine the proper mesh fineness. As a result, 10 mm was used in this study, which was also used in the other studies of transient wave behaviors in both concrete plates (Gibson and Popovics, 2005) and asphalt slabs (Munoz, 2009).

In Figure 4.1, the interface bond was simulated by a tie between the adjacent concrete and asphalt nodes and the interface crack was created by assuming no tension but only friction between the nodes. Over the length of the crack, 'Hard' contact was used in the normal direction to prevent

node intrusion. The crack length was increased from 0 to 1 m at an interval of 50 mm to simulate the growth of the interface debonding.

The material properties used in the model are presented in Table 4.1. Asphalt was considered as an elastic material and its Young's modulus was estimated based on the measured dynamic modulus of the asphalt at 20 °C, which agrees with the values used by Munoz (2009).

Table 4.1. Material properties used in the finite element model.

	E, MPa	v	ρ, kg/m^3
Concrete	30,000	0.2	2500
Asphalt	8,000	0.35	2500

The impact was simulated by a half sine concentrated load and the impact duration was chosen to be 20 µs. The impact was applied at X=0.3m, 0.6m, 0.9m and 1.2m for each crack length. The resultant displacement waves were recorded every 60 mm starting at x=20mm. The sampling frequency is 1 MHz, the same as the sampling frequency used in the laboratory test.

4.3.1   Normalized frequency spectrum

The frequency spectrum of the resultant waves were obtained using the fast Fourier transform. In Figure 4.2, it shows that the frequency spectra of the waves generated by an impact at X=0.6 m and recorded at X=0.55 m for three crack lengths.
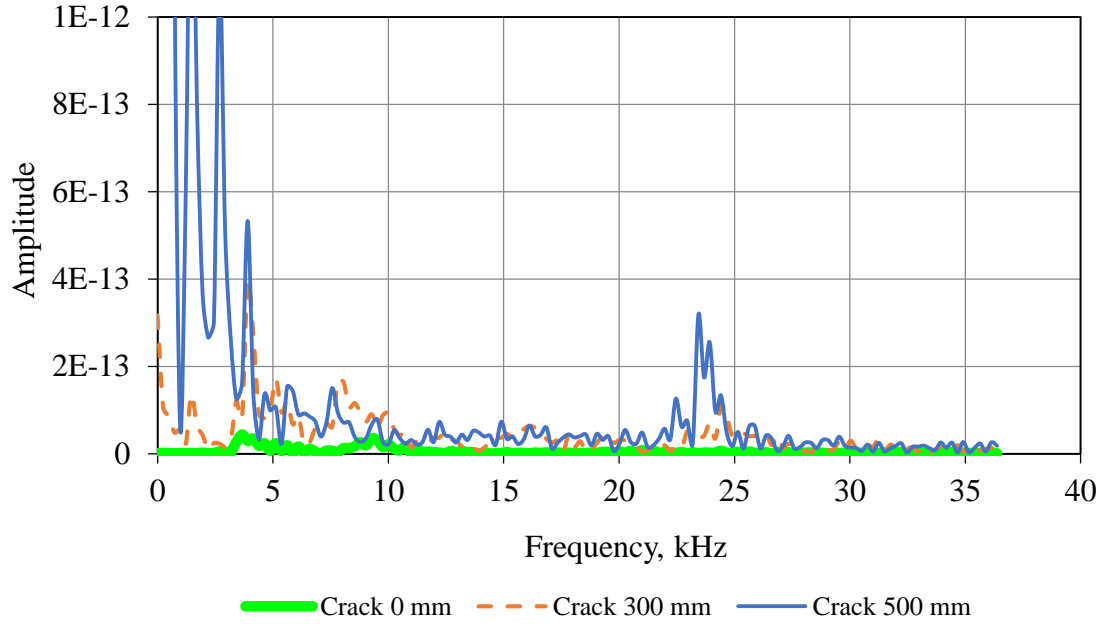
Figure 4.2.Frequency spectrum of the 1.6-m model with impact at X=0.6m and transducer at X=0.55m.

It is obvious that the amplitude of the transient wave is much greater at longer cracks. This is resulting from the reduction of the structural effective stiffness due to the interface cracking. It is not reliable to determine the crack length based on the amplitude of the transient displacements since the amplitude is also highly dependent on the energy of the impact that introduces great variability during experimenting. In order to minimize such variability, each frequency spectrum was normalized relative to the square root of its energy which is defined by Equation (4.5).

$$P = \int_{-\infty}^{\infty} |\hat{x}(f)|^2 \, df$$

(4.5)

where P is the energy of a signal $x(t)$ and $\hat{x}(f)$ is the Fourier transform of the signal.

In Figure 4.3, it shows the normalized frequency spectra for Figure 4.2.The thickness-mode frequency corresponding to the interface as well as the bottom of the asphalt can be determined using Equations (4.1) to (4.3) together with the materials properties in Table 4.1 and are 24.2 kHz and 8.1 kHz, respectively. In Figure 4.3, there is a peak frequency around 9-10 kHz for the zero

62

crack length, which corresponds to the total thickness of the BCOA slab. However, there is no evident peak at 24.2 kHz. This confirms the inference based on the reflection ratio that the thickness mode for the concrete/asphalt interface should be negligible when the bond is intact. There is another dominant frequency at 3.7 kHz for the zero crack length, which agrees with the resonant frequency of the finite element model. The other ripples in the frequency spectrum might be the result of the surface waves or wave reflections at the edges. At a crack length of 300 mm, both thickness-mode frequencies are excited. Meanwhile, the flexural vibration starts to shift to lower resonant modes. When the crack propagates to 500 mm, the flexural mode is so dominant that the thickness-mode resonance corresponding to the total thickness disappears and the amplitude of the frequency corresponding to the interface crack becomes less obvious.
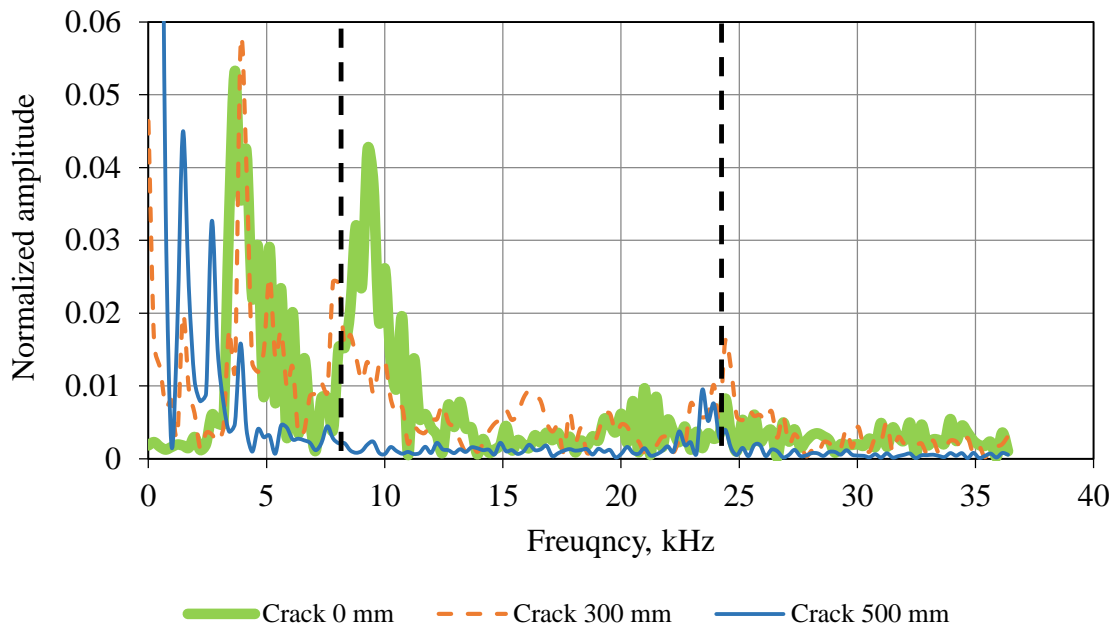
Figure 4.3.Normalized frequency spectrum of the 1.6-m model with impact at X=0.6m and transducer at X=0.55m.

4.3.2 Cross-spectral difference

Multiple mechanisms are responsible for the change in the frequency spectrum as the crack grows, such as the change in resonant frequencies due to the reduction of the structural effective stiffness, the conversion between the thickness modes and the flexural mode, and the relative influence from surface waves and reflections from edges, among others. Most of these mechanisms are complimentary to each other in reflecting the change in the interface debonding. Therefore, it is unnecessary to isolate any individual mechanism in order to establish a function for the interface debonding. Instead, it is more beneficial to establish such a function based on the composite of these mechanisms where they may complement each other.

The whole frequency spectrum at a given crack length was compared to that of the initial condition, which could be related to the size of the debonding. The cross-spectral density S_{xy}, according to Penny (2009), as defined in Equation (4.6) was used to quantify the difference.

$$S_{xy}(\omega) = \int_{-\infty}^{\infty} R_{xy}(\tau)e^{-i\omega t} \, d\tau = \hat{x}(\omega)\bar{\hat{y}}(\omega) \tag{4.6}$$

where $R_{xy}(t)$ is the cross correlation of the two time-domain waveforms x(t) and y(t); $\hat{x}(\omega)$ is the Fourier transform of x(t) and $\bar{\hat{y}}(\omega)$ is the conjugate of the Fourier transform of y(t). It should be noted that the second equality in Equation (4.6) is only true when the two signals have the same length.

In Equation (4.6), $S_{xy}(\omega)$ is a function of the frequency. In order to utilize all the frequencies, the cross spectral density was integrated into the cross-spectral difference (CSD) over the frequency spectrum, as defined in Equation (4.7).

$$CSD = \int_{-\infty}^{\infty} S_{xy}(\omega) \, d\omega \tag{4.7}$$

Normalized cross-spectral density i.e. NCSD was obtained when the normalized frequency spectrum introduced in Section 4.3.1 was used to calculate the CSD. The NCSD is equal to one when the two signals are identical and it reduces as the two signals differ.

4.3.3 Linearity between the crack length and the normalized cross-spectral difference

The magnitude of NCSD depends on the impact location, transducer location and crack length. For example, when the impact was at X=300 mm, the NCSD was determined for four transducer locations. The results were presented as a function of the crack length as shown in Figure 4.4. In the finite element model shown in Figure 4.1, 20 different crack lengths were used excluding the initial condition. For each crack length, the impact was applied at X=0.3m, 0.6m, 0.9m and 1.2m and the waveforms were recorded at 27 locations, namely every 60 mm starting at X=20mm. Therefore, there are in total 20×4×27=2160 NCSDs.
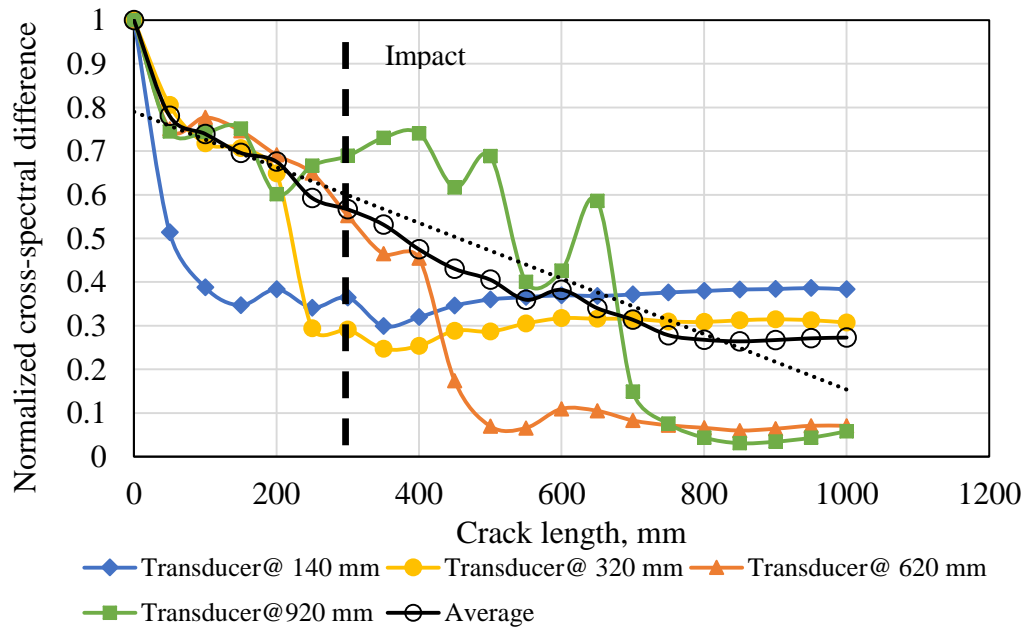
Figure 4.4. Normalized cross-spectral difference Vs. the crack length for the 1.6-m model at four transducers locations, with the impact at X=0.3m

In Figure 4.4, the transducers show a more or less linear relationship between the NCSD and the crack length until the crack approaches to the transducer location. This linearity reflects the shift of resonances from the total-thickness frequency to the interface-depth frequency as well as the shift of energy from thickness-mode vibration to flexural-mode vibration. The linearity is interrupted when the crack gets to the transducers and the flexural vibration becomes dominant. However, realizing that the rapid drop in NCSD is a very strong indicator of the approaching crack, the linearity of the relationship between the NCSD and the crack length can actually be enhanced through averaging the NCSDs for all the transducer locations at the same crack length. The averaged NCSDs (ANCSD) show a better linear relationship with the crack length than any of the transducers alone, at a crack length within the range of 50 mm to 800 mm. Beyond this range, the ANCSD seem to not be a good indicator, because the edge effect is very significant at small crack length and the flexural vibration is very dominant when the crack is larger than half of the model length. This working range is of particular interest for BCOA applications, because the interface cracking smaller than 50 mm is structurally insignificant for BCOAs and BCOAs would have cracked before the interface cracking exceeds 800 mm.

4.3.3.1 Effect of impact location

For impacts applied at three locations, namely X= 0.3 m, 0.6 m and 0.9 m, the average NCSDs were calculated and compared as presented in Figure 4.5. No significant difference could be concluded between impacts.
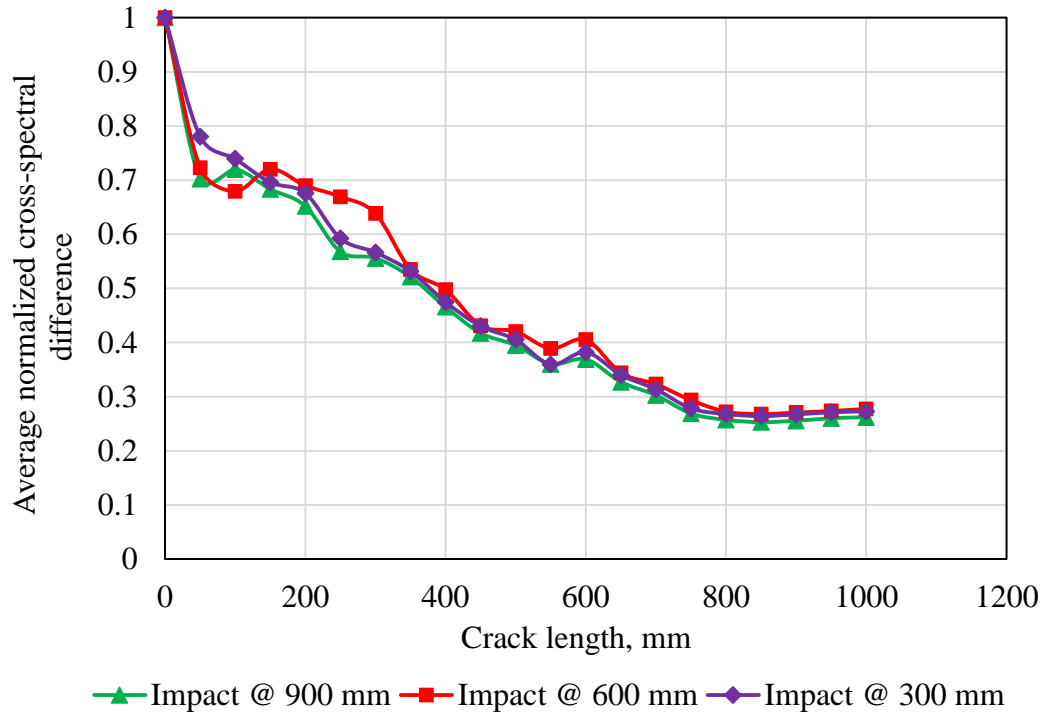
Figure 4.5. Average normalized cross-spectral difference for the 1.6-m model, with the impact at X=0.3m, 0.6 m and 0.9m

4.3.3.2 Effect of crack definition

The cracks were redefined with a smooth interaction between the concrete and asphalt, instead of the frictional interaction in order to reveal the effect of crack definition. The NCSDs were recomputed and the results are presented in Figure 4.6. No significant difference could be concluded between smooth and rough cracks, except that the relationship between the NCSD and the crack length is smoother for a smooth crack.
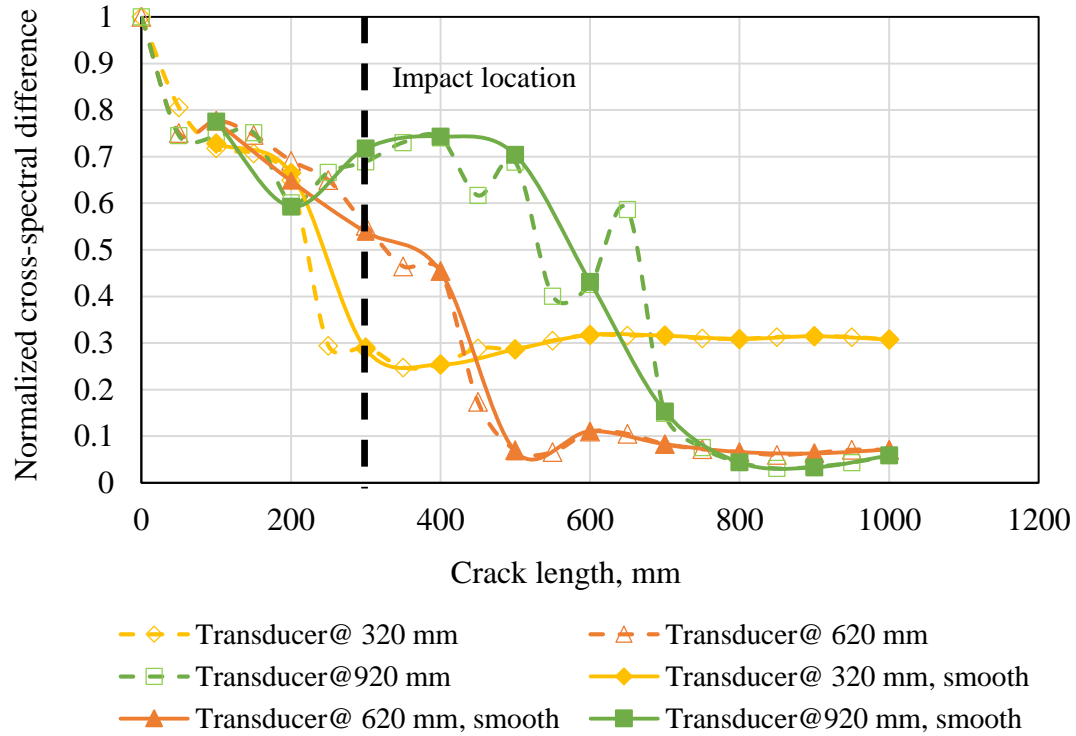
Figure 4.6. Comparison of NCSDs between smooth and rough cracks, 1.6-m model with the impact at X=0.3m.

4.3.3.3 Effect of slab geometry

Another 0.6-m model was developed to study the effect of slab geometry. The length-thickness ratio for this model was 4, compared to 11 for the 1.6-m model. As a result, the 0.6-m model yielded a more desirable linearity between the NCSD and the crack length as illustrated in Figure 4.7. This is most likely because the change in geometry influences on the flexural vibration of the BCOA slabs. It is also noteworthy that the linearity improves greatly for small crack lengths, which is beneficial for determining the crack initiation.
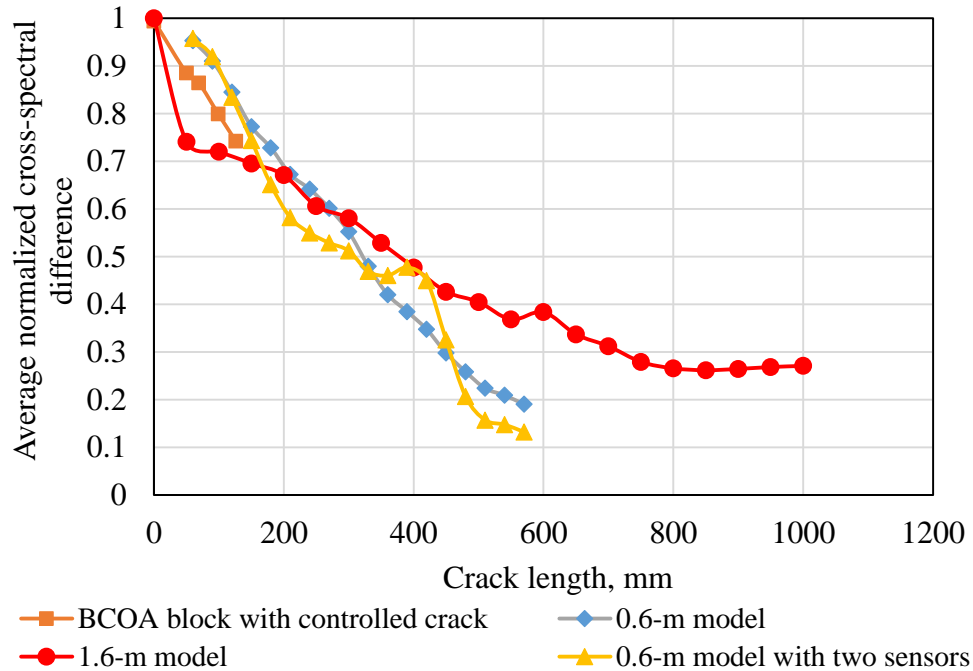
Figure 4.7. ANCSD-Crack length relations for the FE models and the laboratory experiment with controlled crack length.

4.4   LABORATORY EXPERIMENT WITH CONTROLLED CRACK LENGTH

It is common to cast specimens with artificial defects of known size in order to evaluate the effectiveness of a nondestructive method (Kohl et al., 2005, Zhu and Popovics, 2007, and Xie et al., 2012). However, no methodology has been available to simulate a growing interface crack with controlled laboratory specimens. In this study, the interface crack was simulated by introducing saw cuts at the interface of a BCOA specimen and the growth of the crack was simulated by deepening the cuts. It is critical to introduce cuts to the same specimen, since the ANCSD is sensitive to not only the cracking but also any changes of the BCOA specimen.

Figure 4.8 (a) presents the sketch of the test setup. A small BCOA specimen of 300 mm×150 mm×200 mm as shown in Figure 4.8 (b) was used, considering the difficulty in cutting accurately at the interface of a BCOA slab.
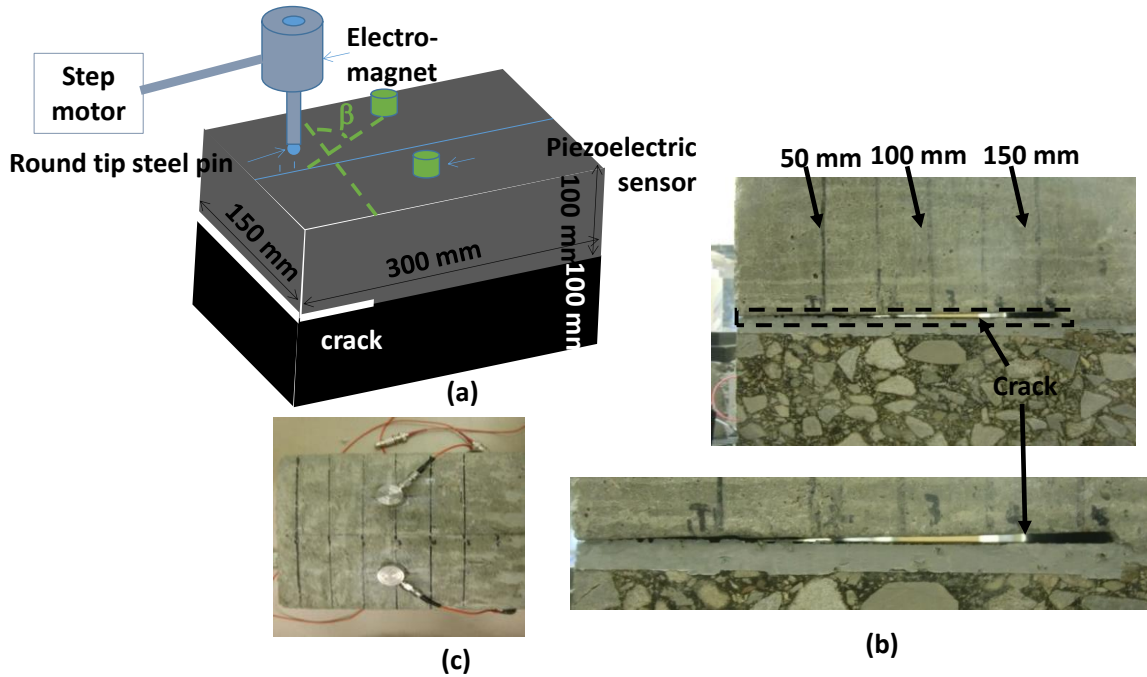
Figure 4.8. Laboratory experiment on a BCOA block, a) test setup, b) controlled precise cuts at the interface, and c) sensor layout and impact locations.

The impact was provided by a round-tip steel pin weighing 10 g. It was first lifted using an electromagnet, engaged for one second after it hit the rubber ceiling and then dropped onto the surface of the specimen. The electromagnet assembly was held by a robot arm that was programmed to apply impacts along the center axis of the block at 23 locations, i.e. every 12.5 mm from one edge. A complete scan of the specimen consisted of 5 impacts at each of the 23 impact locations. The variability due to the impact load was concluded by comparing the five impacts at each location. On average, the standard deviation of the NCSDs between impacts was 2.4%. At least two scans were carried out for each crack length in order to study the variability due to

deepening the crack and recoupling of the sensors. On average, the difference of the ANCSD between the two scans is 2.9%.

Such complete scans were first performed prior to any crack to establish the baseline. They were then carried out after each of the four crack lengths, namely 50 mm, 70mm, 100mm, and 125mm. The concrete collapsed onto the asphalt shortly after extending the crack to 150 mm as shown in Figure 4.8 (b). Signals were recorded with a sampling frequency of 1 MHz for 3 ms. In Figure 4.8 (c), it shows the piezoelectric transducers instrumented 40 mm away from the center axis.

The ANCSDs were calculated based on the laboratory measurements and presented in Figure 4.7. The results confirmed the existence of the linear relationship between the ANCSD and the size of the interface debonding.

In Figure 4.7, the linearity for the laboratory experiment is more similar to the 0.6-m model than the 1.6-m model. This is because the BCOA block used in the experiment presents a length/height ratio of 1.5 that is more similar to the 0.6-m model (length/height ratio of 4) than the 1.6-m model (length/height ratio of 11). It is also interesting to find that the linearity for ANCSD seems to be insensitive to the orientation of the impact-transducer pair. As shown in Figure 4.8 (a), β is the angle of the impact-transducer pair relative to the crack front and it changes as the impact moves forward. Therefore, it seems unnecessary to align the transducers along the direction of crack propagation in order to predict the crack size using the ANCSDs.

4.5 ACCELERATED LOADING TEST

The baseline-dependent transient wave method developed in the previous sections was used to predict the debonding during an accelerated loading test. The configuration of the experiment is shown in Figure 4.9 (a). An intact asphalt slab of 1.8m×1.45m was obtained from an asphalt pavement that was in service for more than five years. The asphalt was aged and distressed by live traffic. The surface the asphalt slab was swept and wet brushed prior to the placement of the overlay and the concrete was cast in the laboratory. For BCOAs with unmilled asphalt, the average thickness was 80 mm and 115 mm for the concrete and the asphalt layers, respectively. For BCOAs with milled asphalt, the average thickness was 100 mm and 90 mm for the concrete and the asphalt layers, respectively. The BCOA slab was then placed onto the concrete testing platform, as shown in Figure 4.9 (b). Two layers of neoprene pads, known as Fabcel 25 (http://www.fabreeka.com/Products &productId=24), were placed between the composite slab and the platform to simulate the granular layers beneath the asphalt. The stiffness of the Fabcel layers was determined by conducting a plate load test according to the ASTM D1195/D1195M (2009), and it was found to be 55 kPa/mm. A joint approximately 10 mm wide was cut through the thickness of the concrete at the midspan after the composite slab was in place. As shown in Figure 4.9 (b), a hydraulic actuator was used to apply cyclic loadings at one of the slab corners. As the loaded side of the joint deflects downward, the asphalt on the unloaded side deflected accordingly owing to the continuity of the asphalt layer. Meanwhile, the concrete on the unloaded side tended to retain its vertical position because it was tied to the massive dead-weight slab and moreover there was nearly zero load transfer across the joint. As a result, a differential deflection occurred between the concrete and the asphalt, which caused damage to the interface bond. The damage accumulated during the fatigue loading eventually resulting in the interface debonding.
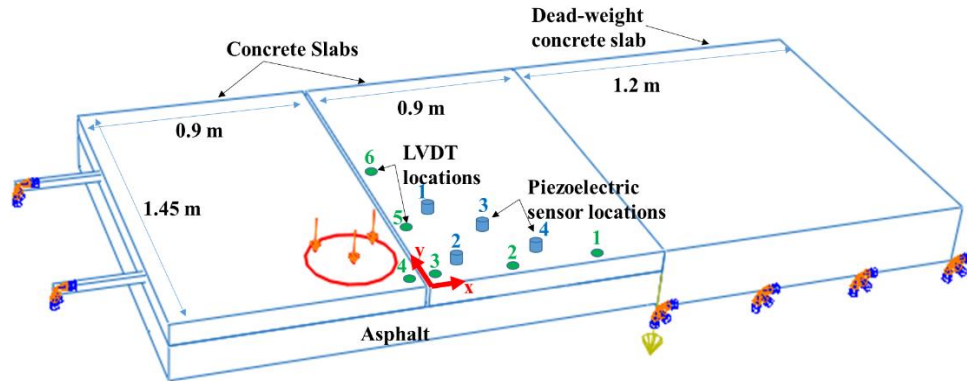
(a)
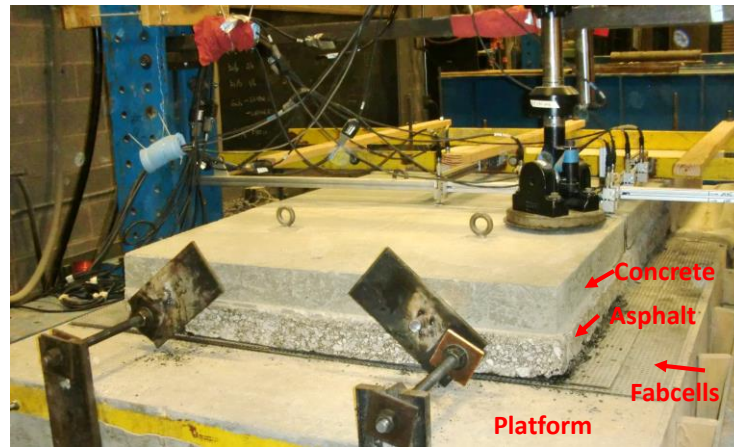
(b)

Figure 4.9. Accelerated loading experiment to study the debonding between concrete overlay and underlying asphalt pavement, (a) sketch of dimensions, (b) test setup.

After each loading period, the composite slab was relaxed adequately to account for the viscoelastic nature of the asphalt. Then the transient wave method was carried out to scan the slab for the development of interface debonding.

For each scan, there were in total 300 impacts applied over the 0.6m×0.6m triangular area at the corner of the unloaded slab. To make sure the impacts consistently hit the same locations, a template with holes in a 25mm×25mm grid pattern, as shown in Figure 4.10, was used. The steel pin used for impact weighed 20 g, which was heavier than the one used for the laboratory test presented in Section 4.4 so that the incident waves would have enough energy to propagate further.

Four piezoelectric sensors were used in the experiment, instrumented at the locations defined in Table 4.2 and shown in Figure 4.9 (a).

Electromagnet
Steel pin
Holes

(b) Top view

Template with holes
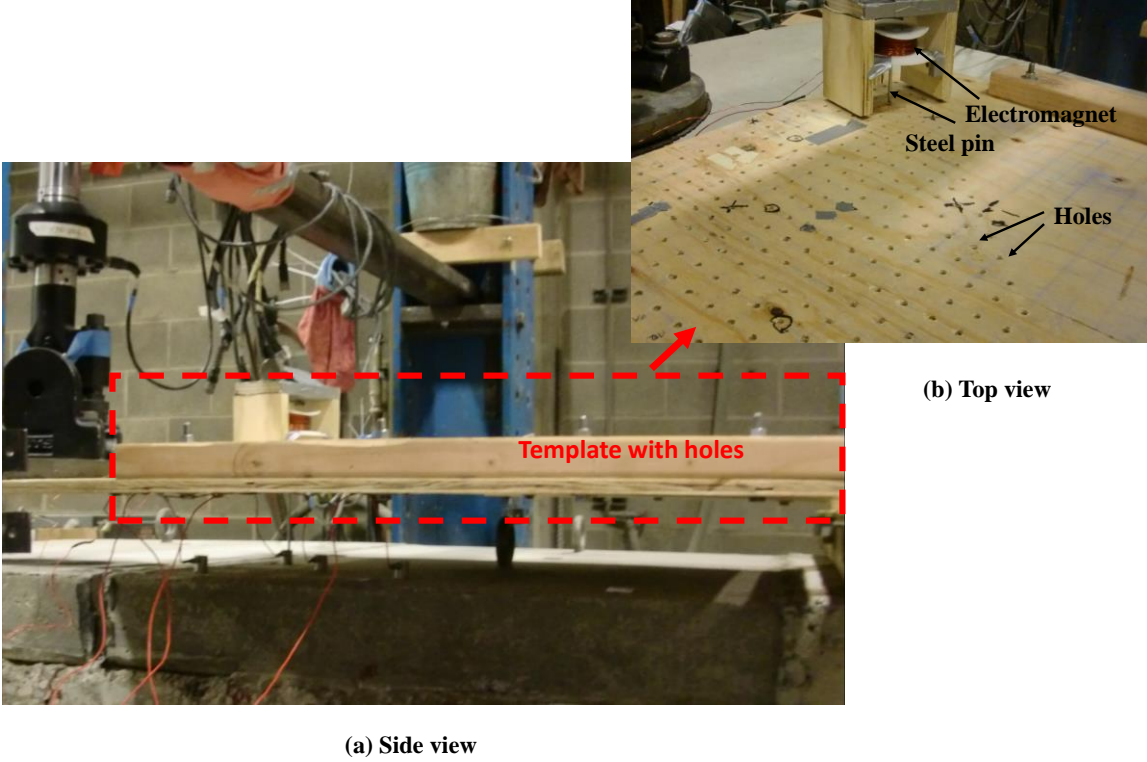
(a) Side view

Figure 4.10. Experimental setup for the transient wave method to scan the BOCA slabs after each accelerated loading period, (a) side view and (b) top view.

Table 4.2. Locations for the acoustic and deflection sensors

		x, mm	y, mm
Linear variable displacement transducer (LVDT)	1	610	40
	2	305	40
	3	25	40
	4	-30*	40
	5	70	460
	6	75	920
Piezoelectric transducer	1	75	610
	2	75	75
	3	340	330
	4	610	75

*negative sign indicating that the sensor is on the loaded side

After establishing the baseline scan at a zero crack length, the average NCSDs for all the impact-sensor pairs of each scan were calculated. For each scan, there were 300 impacts conducted evenly across over the triangular scanning zone outlined by the dashed lines in Figure 4.11. In order to utilize the 2-D model for a 3-D analysis, the 300 impacts were divided into 30 groups, each of which spans three degrees. Next, two closest sensors were assigned to each group. For example, the signals generated by the impacts in the first ten groups that are 0-30º off from the y axis were best received by Sensor 1 and Sensor 2 and thus these two sensors are affiliated with the first ten groups. Similarly, Sensors 2 and 3 are assigned to the ten groups that are 30º -60º off from the y axis and Sensors 2 and 4 are assigned to the ten groups that are 60º -90º off from the y axis. This is illustrated in Figure 4.11.

The linear relationship between the ANCSD and crack length derived from the 0.6-m model was applied to each group independently. As a result, the debonding front was determined at thirty discrete points, one from each group. The shape of the interface debonding was then obtained by connecting the thirty points. Figure 4.11 shows the estimated crack profiles for the unmilled BCOA slab after the loading periods given in the legends. Each data series was labeled to indicate the number of loads accumulated at the time the NDT was performed and the destructive examination was conducted at the end of 1 million loads.
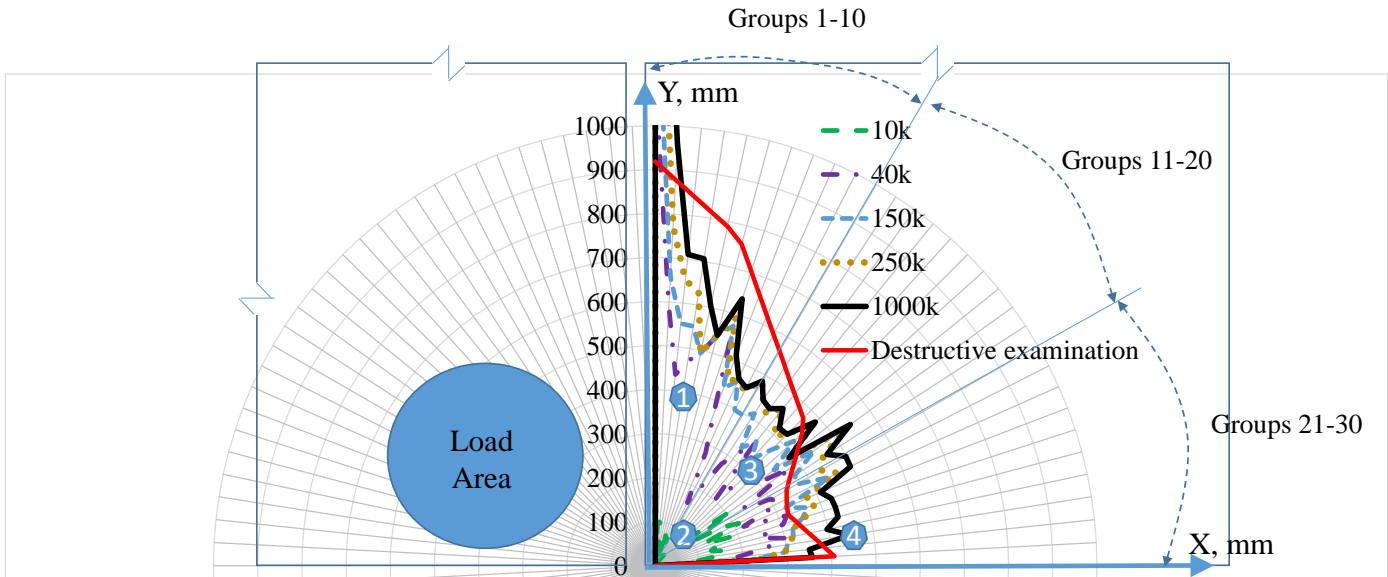
Figure 4.11. Estimated interface debonding for the accelerated loaded unmilled slab using the transient wave method.

It is very clear that the estimated debonding is a function of the load repetitions. Furthermore, the crack profile after 1 million loads was determined destructively by pumping red dye into the delaminated area and then cutting off the concrete overlay in small pieces beyond the crack tip. If we consider the destructively determined crack profile as a relatively reliable measurement, it can be concluded that the estimated crack profile agrees with the measured one at least at 1 million loads. This is especially true when only the total area of debonding is the concern, although the debonding shape is overestimated along the X axis and underestimated along the Y axis. The difference can be explained by the asymmetric boundary conditions in the accelerated loading test, where the restraints for the composite slab was stronger along the X axis than the Y axis. On the other hand, the ANCSD-crack relationship used in the estimation was derived from the 0.6-m model that had symmetric boundary conditions. According to Figure 4.3, the same NCSD relates to a larger crack when the system is more susceptible to flexural vibration. Therefore, the estimation of the crack along the X axis should be reduced to take into account the

stronger restraint at that direction. Similarly, the crack estimation along the Y axis should be increased

Figure 4.12 shows the estimated crack profiles for the milled slab, where the destructive examination was conducted at the end of 2 million loads.
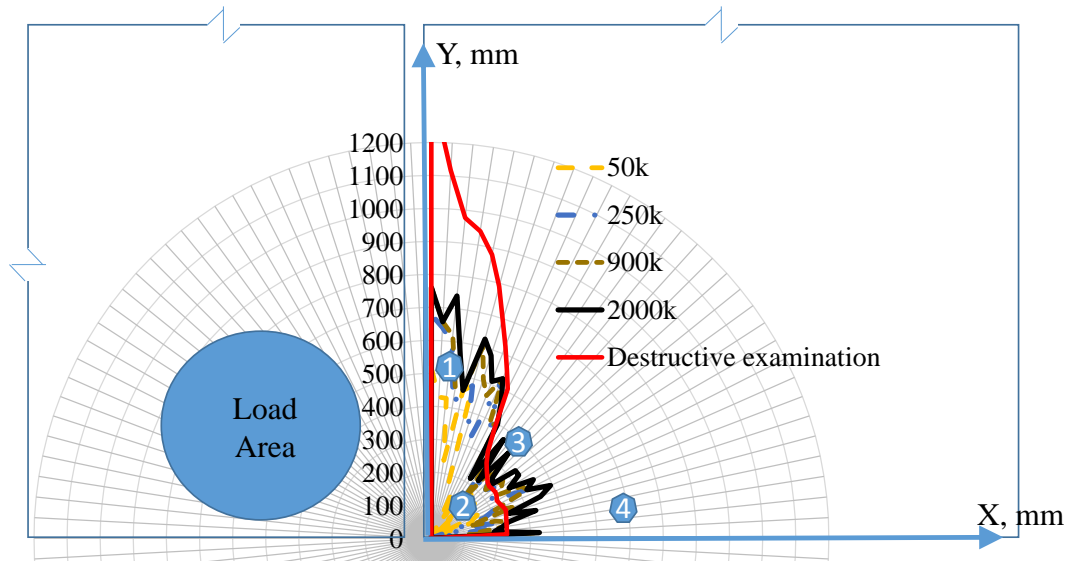
Figure 4.12. Estimated interface debonding for the accelerated loaded milled slab using the transient wave method.

In general, the predicted debonding size for the milled slab is smaller than that measured destructively at the end of the test. This might be due to the fact that the milled slab has a concrete layer 20 mm thicker than the unmilled slab resulting in a much higher flexural stiffness. As discussed previously, the same NCSD will correspond to a smaller crack if the system is stiffer to flexural vibration.

4.6   DEFLECTION METHOD TO DETERMINE THE DEFFECT SIZE

After each loading period, the deflections of the slab associated with a quasi-static load were also measured. The quasi-static load was applied at the same location as the fatigue load, as presented by the circle in Figure 4.9 (a). It was ramped from 0 to 21kN in 60 seconds and the corresponding deflections at the locations defined in Table 4.2 were recorded with a sampling frequency of 1 Hz. The accuracy and range of the linear variable displacement transducers (LVDT) used to measure the deflections is 2.5 µm and 2.5 mm, respectively.

The effective stiffness of the composite structure decreases as the debonding grows. As a result, the deflection measured on the loaded side, i.e. LVDT 4, should increase. On the other hand, since there is no load transfer across the joint, the debonding should lead to the decrease in deflections measured by the LVDTs on the unloaded side. This is confirmed by the LVDT measurements presented in Figure 4.13, where the deflections at zero loading were compared to those after 1 million load applications. Furthermore, it is noticed that the deflections decrease as the LVDT is placed further away from the loaded corner.
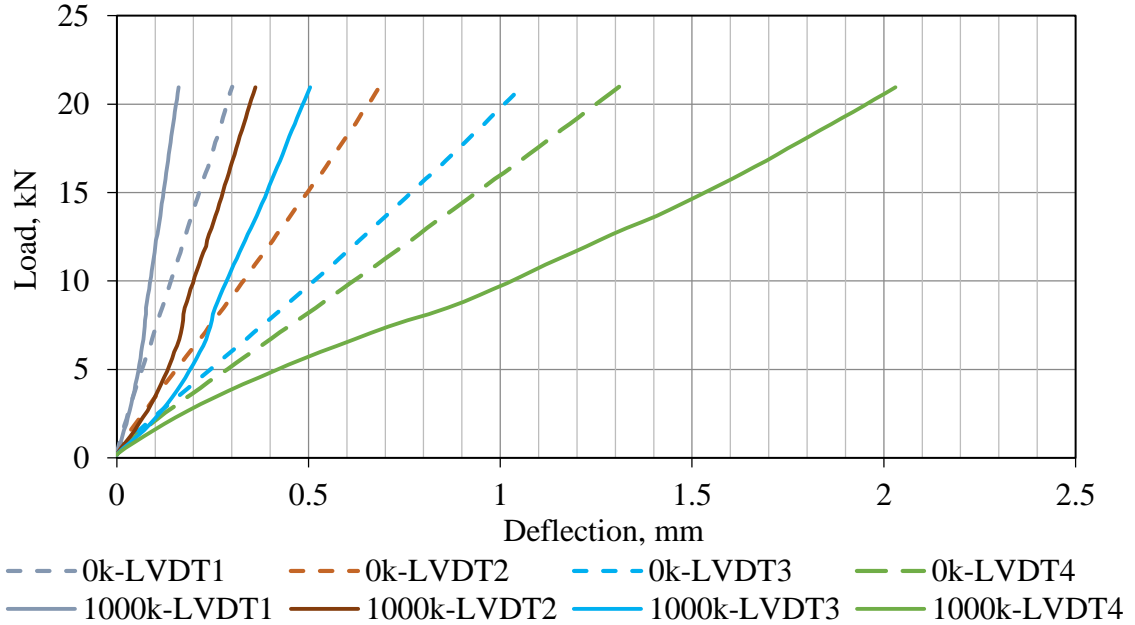
Figure 4.13. Change of deflections due to the growth of the debonding at the interface.

In order to backcalculate the size of the debonding based on the measured deflections, a 3-D finite element model was established using ABAQUS for the assembly presented in Figure 4.9 (a). A mesh size of 2 mm was used after checking the convergence of the model in terms of the deflections at LVDT 4. The same material properties as described in Table 4.1 were used, with the exception that the asphalt was defined as a viscoelastic material due to the much slower loading rate compared to that employed in the impact-load analysis. AASHTO T 342-11 was followed to determine the dynamic modulus of the asphalt specimens at three temperatures and four frequencies, for which the results were summarized in Table 4.3.

Table 4.3. Dynamic modulus and phase angle for the asphalt

Temp, °C	5		21		40	
f, Hz	$|E^*|$, GPa	φ, °	$|E^*|$, GPa	φ, °	$|E^*|$, GPa	φ, °
10	10.58	9.5	5.72	18.3	1.58	27.7
1	8.31	12.4	3.48	23.9	0.80	27.1
0.1	6.24	16.1	1.99	26.7	0.47	25.1
0.01	N.A.	N.A.	N.A.	N.A.	0.047	23.9

The master curve at a reference temperature of 20 °C was then established statistically based on the data in Table 4.3. The master curve is presented in Equation (4.8) with R^2 of 0.999. A spring foundation was used with a k-value of 55 kPa/mm.

$$\log(E^*) = -1.2427 + \frac{2.6173}{1 + \exp(-0.7778 - 0.3749\log(f))} \tag{4.8}$$

where E^* is the dynamic modulus of the asphalt mixture in GPa and f is the loading frequency, Hz.

For simplicity, it is assumed that the debonding presents the shape of a triangle based on the observed debonding in Figure 4.11 and Figure 4.12. Then, an objective function with the two parameters a_1 and a_2 representing the two edges of the triangle was defined as shown in Equation (4.9). The size of the debonding was then backcalculated by minimizing the objective function.

$$obj(a_1, a_2) = 1 - \frac{\sum_{j=1}^{6} b_j P(x(t), y(t))}{\sum_{j=1}^{6} b_j} \tag{4.9}$$

where P is the Pearson correlation coefficient (Lehmann, 1986) between the measured deflections $x(t)$ and estimated deflections $y(t)$, which measures the similarity between the estimation and the measurement for each individual LVDT. Since the shape of the interface resembles a triangle according to Figure 4.11, $y(t)$ is determined by searching the triangular shapes of various edge lengths at the interface. b_j is the weight factor for the jth LVDT and 0.25, 0.5, 1, 1, 0.5, and 0.25 were employed for LVDTs 1 to 6, respectively. A larger weight was assigned to the LVDTs closer to the loaded corner, because of their greater sensitivity to the debonding.

The bottom of the asphalt taken from the in-service pavement was uneven. A strip approximately 0.3 m wide was missing for the whole length of the unmilled slab as shown in Figure 4.14, which was more severe for the milled slab. Despite the fact that the BCOA slab was

flipped to fill up the missing strip with cold patch, the cold patch presents much different properties relative to the aged hot mix asphalt and it failed much quicker during the fatigue loading. The degradation of the cold patch was accounted for by reducing the modulus of subgrade reaction, i.e. k-value, over the patched area.
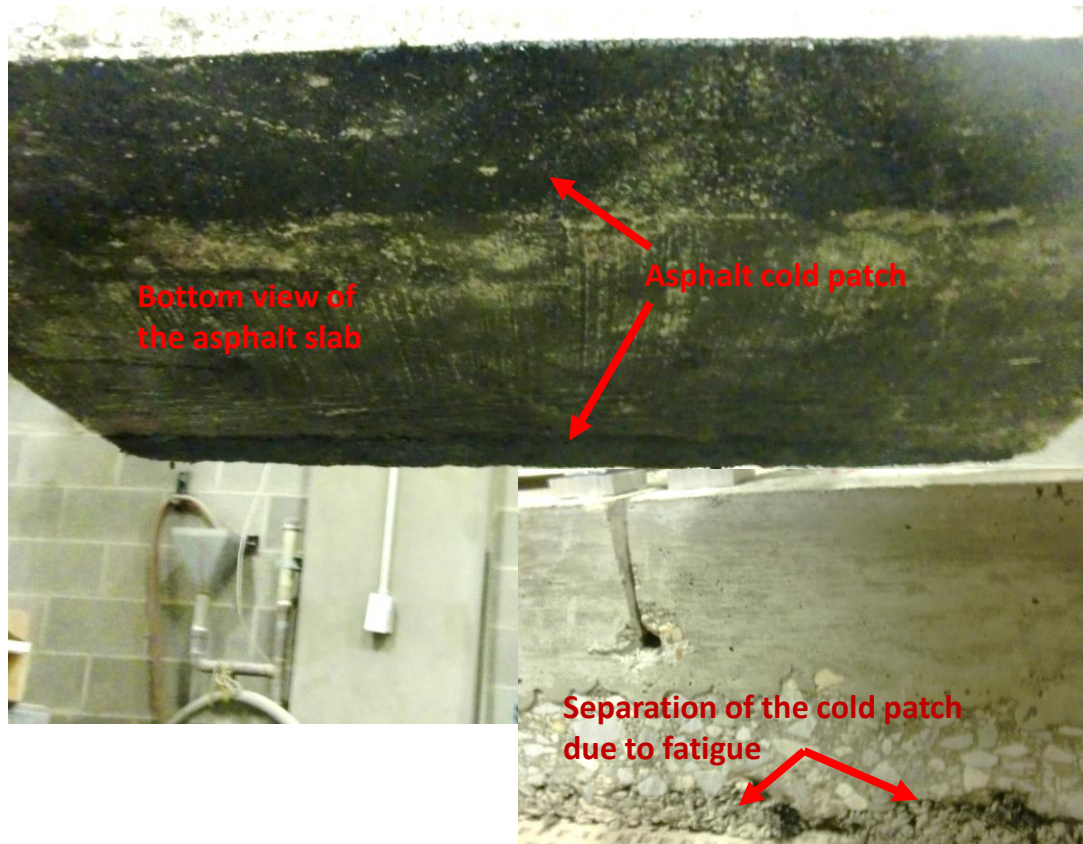
Figure 4.14. Cold patch at the bottom of the unmilled asphalt slab and its separation during fatigue loading.

The magnitude of the reduced k-value was determined by optimizing the objective function at the beginning and end of the test. For the unmilled slab with zero debonding, the objective function reaches its minimum, i.e. 0.06, when the k-value for the cold patch is approximately 27.5 kPa/mm. The estimated deflections at this moment was compared with the measured deflections in Figure 4.15, in order to demonstrate the quality of the backcalculation associated with obj=0.06. For the model with the final debonding shape, as determined destructively after 1 million load applications, the objective function is only optimized with a k-value of approximately 14 kPa/mm. It was impossible to measure the degradation of the cold patch during the experimental fatigue loading. Therefore, the backcalculation for the interface debonding was carried out for the reduced k-value of both 27.5 kPa/mm and 14 kPa/mm for the patched area.
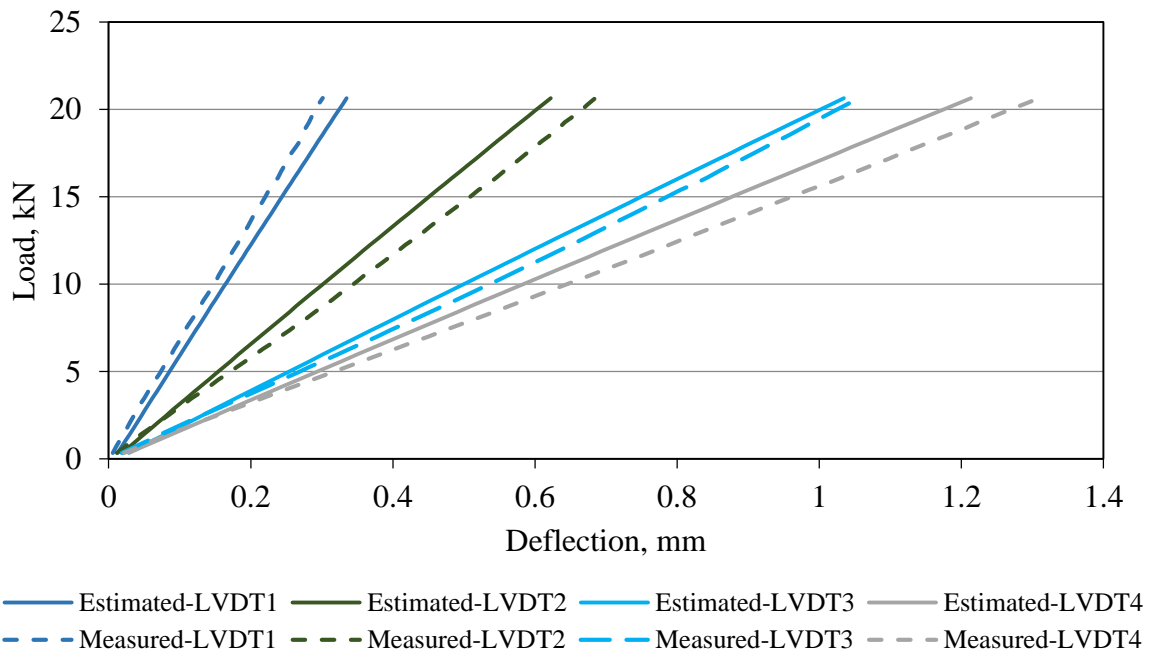
Figure 4.15. Comparison between estimated and measured deflections for the unmilled slab with a k-value of 27.5 kPa/mm for the cold patched area.

The area of debonding was calculated based on the deflection method and the transient wave method, and the results were compared as presented in Figure 4.16. The predictions based

on the two methods show a good agreement with each other. The transient-wave method seems capable to more accurately determine the growth of the interface debonding. This is indicated by the fact that its prediction was similar to that based on the deflection method with a k-value (Patch)=27.5 kPa/mm at the beginning of the loading. As the cold patch degraded, the transient-wave predictions approached the values provided by a k-value (Patch)=14 kPa/mm.
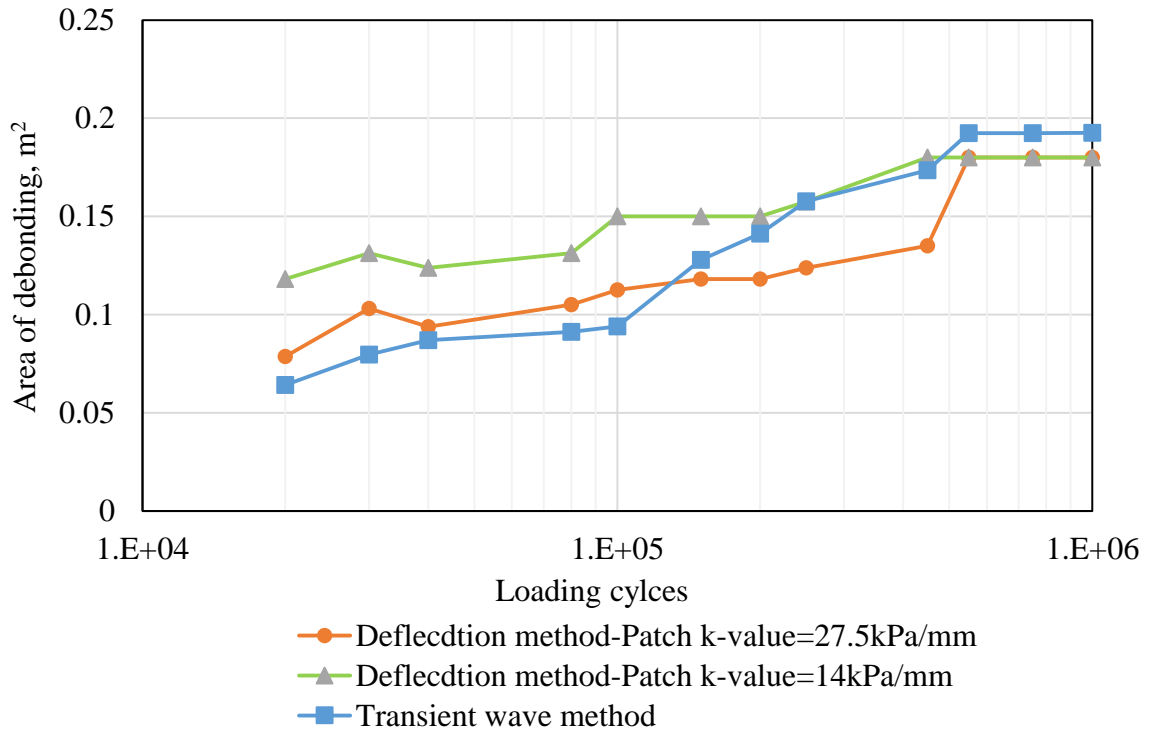
Figure 4.16.Area of debonding as a function of loading cycles predicted by both the deflection and transient wave methods for the unmilled slab.

4.7   CONCLUSIONS

A baseline-dependent transient wave method was developed to quantify the growth of the interface debonding between the concrete overlay and the underlying asphalt due to fatigue loading. The test setup was similar to that of an impact-echo test. However, the resultant frequency spectra were

compared to the baseline condition to update the debonding information, instead of identifying the peak frequency corresponding to the thickness-mode resonance as was traditionally used in the impact-echo test.

A characteristic parameter, the average normalized cross-spectral difference, was established and found to have a linear relationship with the length of the interface crack based on numerical modeling. The linear relationship is independent of the crack smoothness or impact location, while is a function of the geometry of the tested slab and its boundary conditions. Such linearity was confirmed by a laboratory experiment where the normalized cross-spectral difference was measured for a specimen with controlled crack lengths.

The transient wave method was applied to the quantification of the interface debonding during the accelerated loading test. The estimated debonding was validated by the profile determined destructively at the end of the test. It also shows good agreement with the predictions made based on a deflection based nondestructive method. In order to improve the accuracy of the transient-wave method, a 3-D finite element model will be needed to study the ANCSD-crack length linearity corresponding to various flexural stiffness and boundary conditions.

5.0   DEBONDING MECHANISM OF BONDED CONCRETE OVERLAY OF ASPHALT DUE TO FATIGUE LOADING AND ITS EFFECT ON THE PERFORMANCE OF THE OVERLAY

5.1   INTRODUCTION

Bonded concrete overlay of asphalt (BCOA) has been widely used to rehabilitate distressed asphalt pavements over the past two decades (Cole et al., 1998 and Roesler et al, 2008). The overlay is often constructed as thin as 70 mm to 150 mm yet still reported to be able to achieve a satisfying service life of 10 years or longer with minor maintenance. One key for such a thin overlay to survive significant traffic and environmental loading is the presence of the interface bond between the overlay and the underlying asphalt. An effective bond lowers the neutral axis of the composite structure resulting in the reduction of the tensile stress in the overlay. On the other hand, the loss of the bond can result in premature failure of the BCOAs, which has been reported many times over the past decade (Vandenbossche and Fagerness, 2002, Nelson and Rasmussen, 2002; Vandenbossche, 2005). Forensics on the debonded slabs revealed three possible scenarios for the loss of the bond, namely the debonding at the concrete/asphalt interface, the delamination between asphalt lifts and asphalt raveling. Although the consequence for all the scenarios is the same, i.e. reducing the effective stiffness of the BCOA and increasing the probability of overlay cracking, they happen for different reasons. Asphalt raveling is a material- and moisture-related distress. It can be prevented by proper design of the asphalt mixture and maintaining good pavement drainage. The delamination between the asphalt lifts mostly occurs when the asphalt layer milling depth is poorly chosen so that there is a very thin layer of the asphalt surface course left after milling.

85

Cracking then tends to initiate at the interface between the remaining surface course and the base course. This type of delamination can also be minimized by coring prior to milling so the depths of the asphalt lifts can be established. Finally, debonding at the concrete/asphalt interface develops due to repetitive traffic and environmental loading. The primary mechanism for the traffic-related fatigue is depicted in Figure 5.1. When a traveling wheel approaches a joint, the asphalt on the loaded side of the joint is compressed. The asphalt on the unloaded side of the joint deflects accordingly, owing to the continuity of the asphalt layer. However, the concrete overlay on the unloaded side tends to retain its position and thus causes a differential deflection between the concrete overlay and the underlying asphalt on the unloaded side of the joint. The repetitive application of such wheel loads will result in fatigue damage to the interfacial bond and eventually fractures the interface.
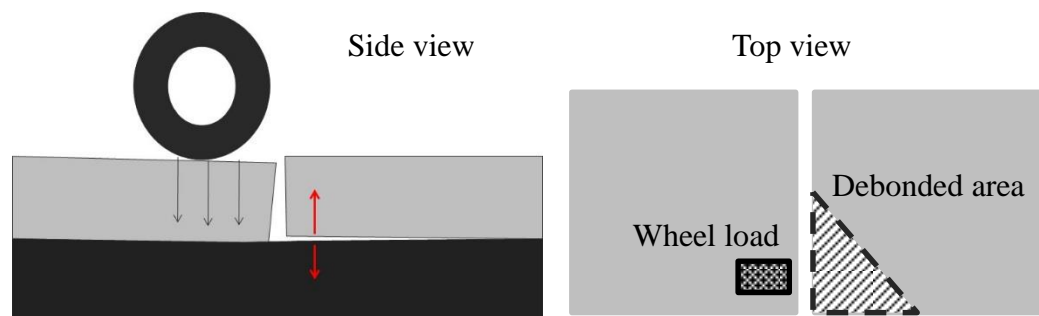
Figure 5.1. Mode-I debonding of the interface due to repetitive traffic loads.

Pouteau et al. (2004) and Chabot et al. (2008) have successfully recreated the interface debonding for BCOAs under fatigue loading in their accelerated loading facility. They further found that the fatigue of the interfacial bond was a function of the surface preparation of the asphalt layer as well as the environmental conditions, such as temperature and moisture. These findings have been confirmed by other laboratory and field experiments (Delatte and Sehdev, 2003 and Al-Qadi et al. 2008).

Despite the considerable research effort in studying the BCOA interfacial debonding, there has been no quantitative study on the development of such debonding under fatigue loading. As a result, a constant adjustment factor has been accepted in the current design procedures to account for the increase in the stress in the overlay due to partial bonding. Tarr et al. (1998) proposed 50%-60% for the increase in the stress, based on the comparison between the predicted and measured strains from three projects in Colorado. Wu et al. (1999) suggested 20%-60% increase based on three projects, one in Missouri and two in Colorado. The use of such empirical and constant adjustment factors might lead to unreliable design, since the projects used for the calibrations only represent a few design scenarios and more importantly, the interface debonding grows gradually over time and is not constant.

In this study, the growth of the interface debonding under fatigue loading will be quantified and taken into account in the design of the BCOA. For the first time, it is proposed that the degree of debonding at the concrete/asphalt interface be defined by the area of the interface debonding as illustrated in Figure 5.1. Fatigue of the interface bond was realized through the accelerated loading of large-scale BCOA slabs in the Accelerated Loading Facility (ALF) housed at University of Pittsburgh. After each loading interval, the growth of the interface debonding was established nondestructively and the fracture energy responsible for the fracture was calculated using a cohesive-zone based finite element model. Based on the ALF test and the numerical modeling, the growth of the interface debonding was established as a function of the fatigue loading numbers as well as the fracture energy subjected by each individual load. The effect of the interfacial debonding in terms of increasing the critical stress in the concrete overlay was also discussed.

5.2   ACCELERATED LOADING TEST

ALF testing is a good compromise between in-situ testing and small-scale laboratory testing. The difficulty of conducting in-situ fatigue tests not only lies in the tremendous monetary and time cost but also the complexity to collect and analyze the data, although the results from an in-situ test best reflects the realistic climatic and traffic conditions. On the other hand, a small-scale laboratory test can be more economical, quicker and better controlled. Nevertheless, its shortcoming is the unavoidable loss of reality due to the size effect. In an ALF test, actuators are used to simulate traffic loads with much higher frequency than live traffic so it is less time consuming to collect the data. Large-scale slabs are used so that the size effect is minimized. Moreover, the test is prepared and conducted indoor so that accurate control and precise measurements become possible. For example, the mechanical boundary conditions of the tested slabs can be well established giving leverage to the modeling of the experiment. The configuration of the BCOA slabs tested at the Pitt-ALF is shown in Figure 5.2 (a).
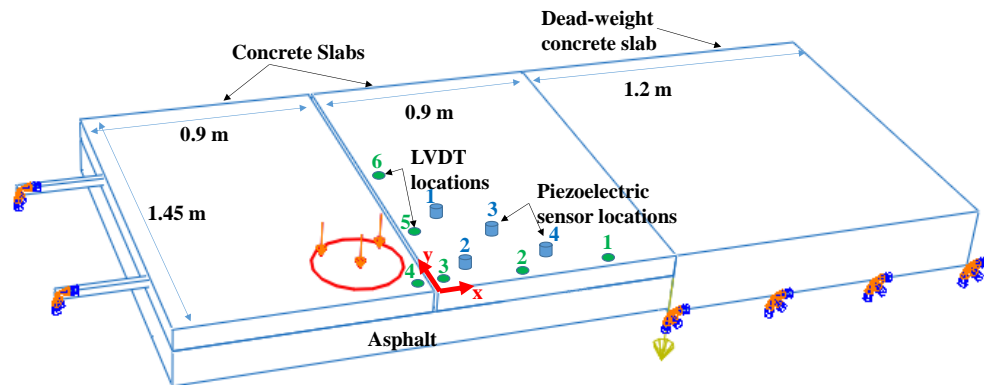
(a)
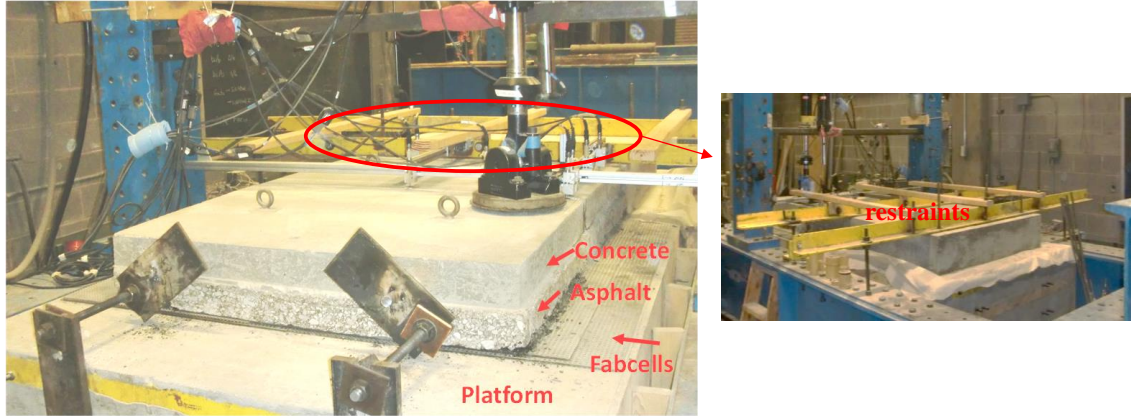
(b)
Figure 5.2. (a) Schematic and (b) setup of the BCOA tested at the Pitt-ALF.

5.2.1 Layers

The asphalt layer of the BCOA slabs is approximately 80-100 mm thick if milled, and 100-130 mm thick if unmilled. The asphalt was extracted as intact slabs that are approximately 1.8 m×1.45 m from Highway 50 near Bridgeville, PA. After more than five years in service, the asphalt was aged and mildly distressed. Portions of the pavement were milled in place by the contractors before retrieving the asphalt slabs in order to study the effect of milling. The concrete overlay in Figure 5.2 (b) was cast onto the asphalt in the laboratory. In total, two composite BCOA slabs were tested and analyzed, one milled and the other unmilled, for which the statistics of the measured layer thicknesses are presented in Table 5.1.

Table 5.1. Layer thickness for the BCOA slabs tested at Pitt-ALF.

		Slab 1	Slab 2
Asphalt thickness, mm	mean	90	115
	standard deviation	5	5
Concrete thickness, mm	mean	100	80
	standard deviation	5	5
Milling condition		Milled	Unmilled

Before lifting the cured BCOA slab onto the testing platform, two layers of neoprene pads were placed on the platform to simulate the underlying granular layers. The stiffness of the Fabcel layers was determined by conducting a plate load test and was found to be 55 kPa/mm. Before testing, a joint of about 10 mm wide was cut through the depth of the concrete overlay to form two concrete slabs.

5.2.2   Loading and boundary condition

One hydraulic actuator with a 300-mm diameter circular loading plate was employed. A half-sine load ranging from 2 kN to 40 kN was applied repeatedly at the corner of the concrete slab. The duration of the load is 0.035 second followed by a rest period of 0.165 second when the static load was maintained at 2 kN. Therefore, the effective period for one loading cycle is 0.20 second. The temporal profile for the load magnitude is illustrated in Figure 5.3.
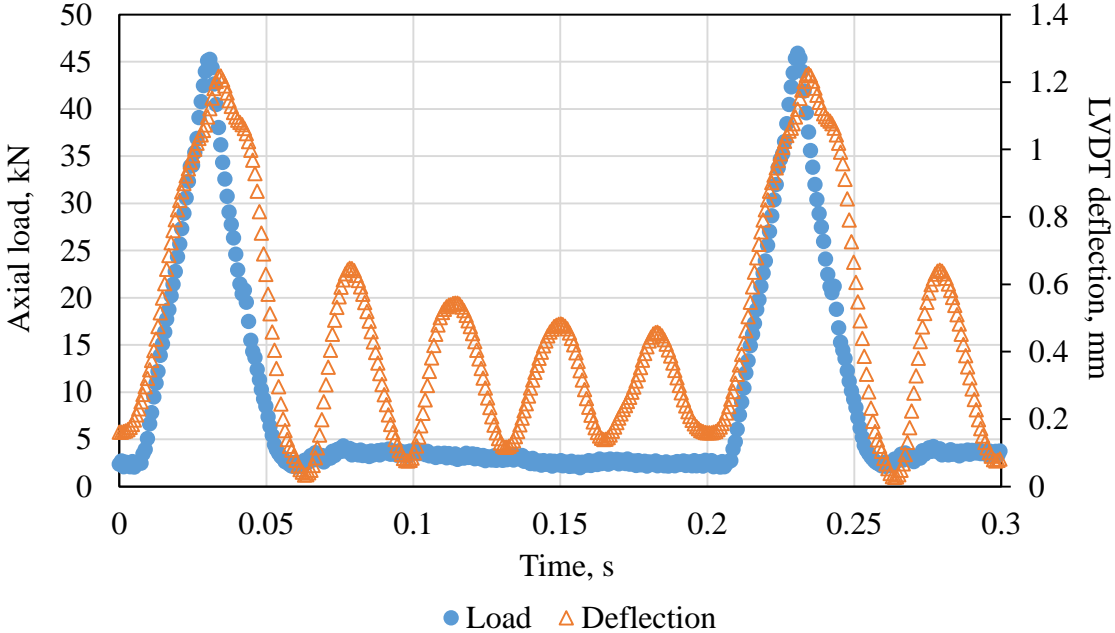
Figure 5.3. Loading profile used in the ALF test and the resultant LVDT deflections.

In Figure 5.3, its shows the deflection measured at the corner of the loaded slab depicted as Location 4 in Figure 5.2 (a) using a linear variable displacement transducer (LVDT). There is a phase lag between the deflection and the load due to the viscosity of the asphalt. It is also interesting to notice the damping of the deflection during the rest period, which can be also attributed to the visco-elastic nature of the asphalt.

The actuator load introduces differential deflections at the interface of the unloaded slab, similar to that illustrated in Figure 5.1. As the loaded side of the joint deflects with the actuator, the asphalt underneath the unloaded concrete slabs tends to deflect accordingly owing to the continuity of the asphalt layer. Meanwhile, the concrete slab on the unloaded size retained its position because there was nearly zero load transfer across the concrete joint. Furthermore, the unloaded concrete slab was tied to the massive testing platform on its further end restraining it from any vertical displacement. A closer view of the restraint system is available in Figure 5.2.

5.2.3   Material properties

Cores of the asphalt slabs were taken to measure the complex modulus of the asphalt, as is presented in Table 5.2. Both fresh and harden concrete properties were also tested and the results are presented in Table 5.3.

Table 5.2. Dynamic modulus for the asphalt as a function of temperature and frequency.

Temperature, °C	5		21		40	
Frequency, Hz	|E*|, GPa	Temp., °	|E*|, GPa	Temp., °	|E*|, GPa	Temp., °
10	10.58	9.5	5.72	18.3	1.58	27.7
1	8.31	12.4	3.48	23.9	0.80	27.1
0.1	6.24	16.1	1.99	26.7	0.47	25.1
0.01	N/A	N/A	N/A	N/A	0.32	23.9

Table 5.3. Concrete material properties.

Property	Value
28-day Compressive strength, MPa	35.5
28-day Elastic modulus, GPa	25.5
Air, %	2.5
Slump, mm	75

5.3 NONDESTRUCTIVE EVALUATION OF THE INTERFACIAL DEBONDING

After each loading period, the asphalt was first relaxed adequately and then two methods, namely a transient wave based method and a deflection based method, were employed to conduct the nondestructive evaluation. The details of the methods can be found in the Section 4.5. An example can be found in Figure 5.4, where it presents the estimated area of debonding after 10,000, 40,000, 150,000, 250,000 and 1 million loads as well as the area of debonding determined destructively at the end of 1 million loads. The destructive examination was carried out by pumping red dye into the interface and then carefully sawing off the concrete overlay beyond the crack tip, as shown in Figure 5.5. This method was found to be effective in revealing the location of the crack tip.
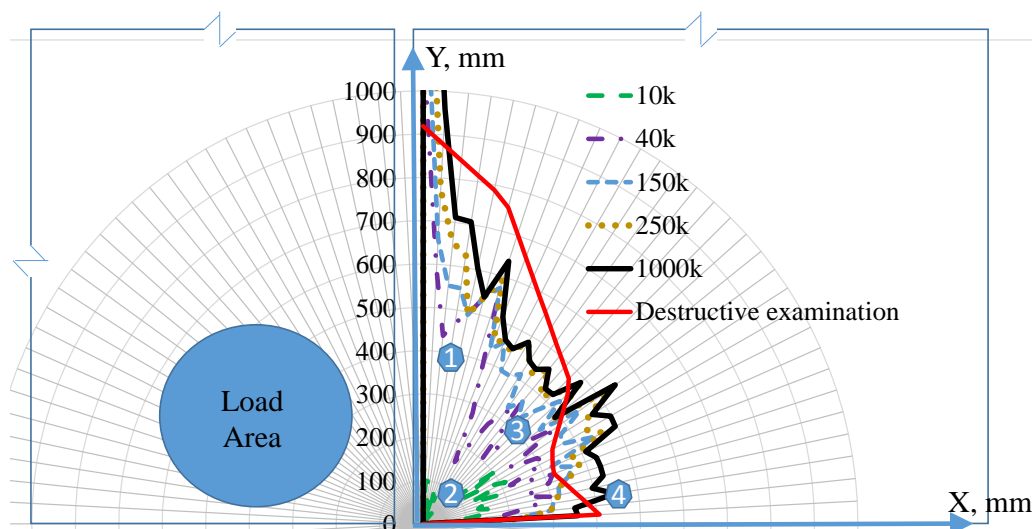
Figure 5.4. Estimated interface debonding for Slab 2 as a function of the fatigue loading.

Figure 5.5. Forensics of the interface debonding by dying and cutting.

If we assume the area of debonding determined destructively is a relatively more reliable measurement, the estimation by the nondestructive testing seems to have a good predictability. The offset between the destructive and nondestructive estimations at 1 million loads might be due to the fact that asymmetric boundary conditions were used in the ALF between the edge (x axis) and the joint (y axis), while the transient wave method was developed for symmetric boundary conditions. It is obvious that the crack preferred to propagate along the joint where it was less restrained. Provided the area of debonding destructively determined at the end of the ALF tests, the area of debonding corresponding to different load intervals was interpolated for the two tested slabs as summerized in Figure 5.6.
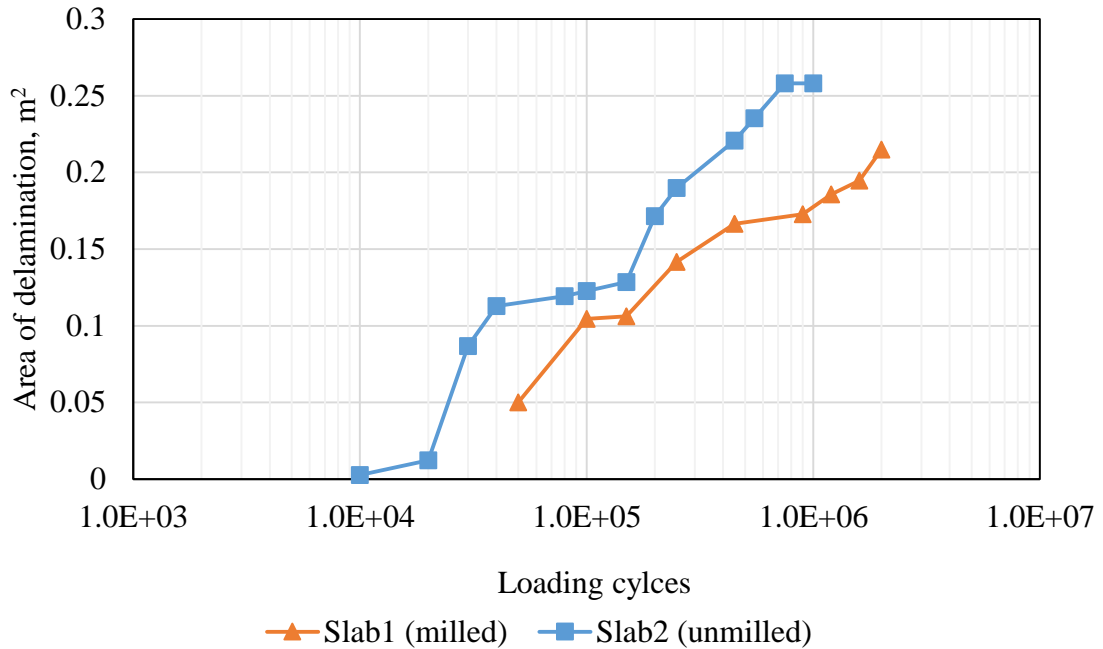
Figure 5.6. Area of the interface debonding as a function of number of fatigue loads.

It is expected that the interface debonding for the milled slab grew at a slower rate than the unmilled slab. During the fatigue test, the development of the interfacial crack was monitored from the side of the BCOA slabs, as shown in Figure 5.7. Although the observation made from the side could not fully represent the phenomenon across the section, it confirms the occurrence of asphalt cracking resulting from the dissipation of fatigue energy into the asphalt after 100,000 loads. The fatigue of the asphalt most likely happens when the interface fracture grows to such a level that cracking in the asphalt becomes more efficient in dissipating the fatigue energy.

Figure 5.7. Interface cracking observed on the side of Slab 2 during the ALF test.

5.4　FINITE ELEMENT ANALYSIS FOR CALCULATING THE INTERFACIAL FRACTURE ENERGY

In order to establish the fatigue law for the interface debonding, a cohesive-zone based finite element model was developed for the ALF tests using ABAQUS Ver. 6.11 in order to calculate the energy driving the fracture of the bond. The schematic of the model is presented in Figure 5.8, where it employed the built-in geometry as well as the measured material properties from the ALF tests as discussed in the previous section.

The key of the model is the cohesive elements that simulate the bond at the interface of the unloaded slab. The cohesive elements have two layers of nodes, which are tied to the concrete and asphalt respectively. The constitutive behavior for the cohesive elements can be defined by the relationship between the tension and separation of the two layers of nodes, i.e. the so-called traction-separation law. The traction-separation laws were determined for both milled and unmilled specimens based on the wedge-splitting test of BCOA small-scale block specimens, as

95

shown in Figure 5.8. The details of the wedge splitting test as well as the establishment of the cohesive elements can be found in Section 2.2 and Section 3.3, respectively.
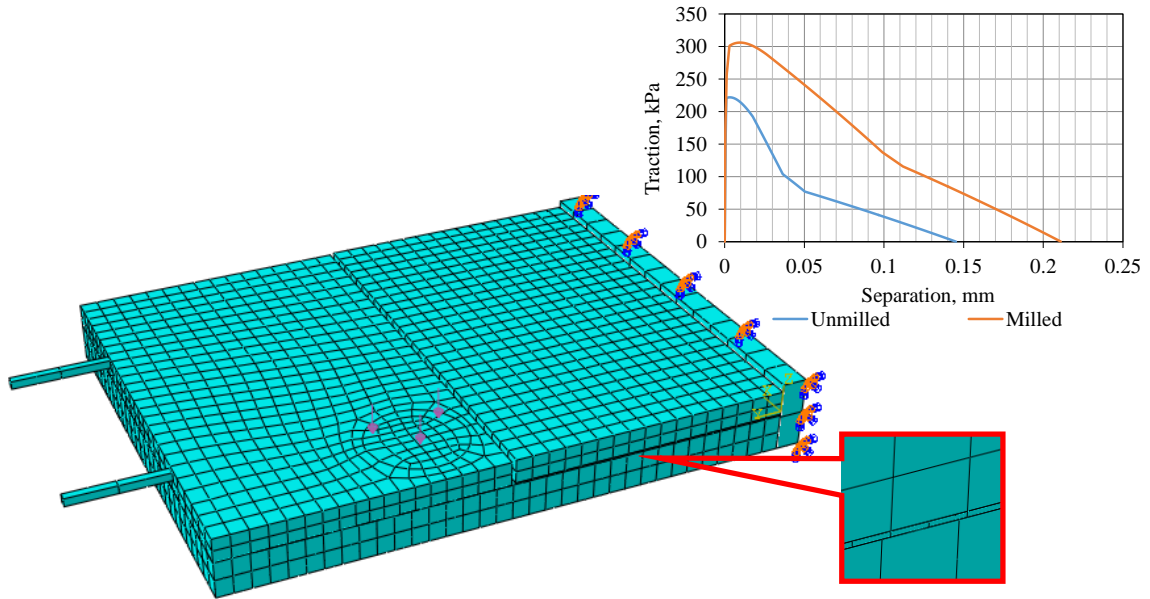
Figure 5.8. Finite element model for the ALF tested BCOA slabs using cohesive elements.

The damage of the cohesive element, termed as $SDEG$ in ABAQUS, is defined by the ratio of its degraded stiffness to the undamaged stiffness E_0 as shown in Equation (5.1).

$$SDEG(\delta) =\cdot \frac{E(\delta)}{E_0} \qquad (5.1)$$

where δ is the separation between the two layers of nodes of the element and $SDEG$ ranges from 0 for no damage to 1 for totally damaged.

In Figure 5.9, it shows the loading-unloading paths for the cohesive elements at different damage state. A cohesive element is undamaged if the maximum separation has not been beyond the nominal separation, when its loading-unloading is purely elastic, following the blue path in Figure 5.9. Once the separation of a pair of nodes exceeds the nominal value as indicated by the solid green curve, there is damage occurring to the cohesive element resulting in a permanent loss

of its stiffness. Therefore, the unloading and reloading of the element should following the green dash line. If a partially-damaged element continues to be loaded after its historical high separation, it will follow the red curve until it becomes fully damaged and is then removed from the rest of the analysis.
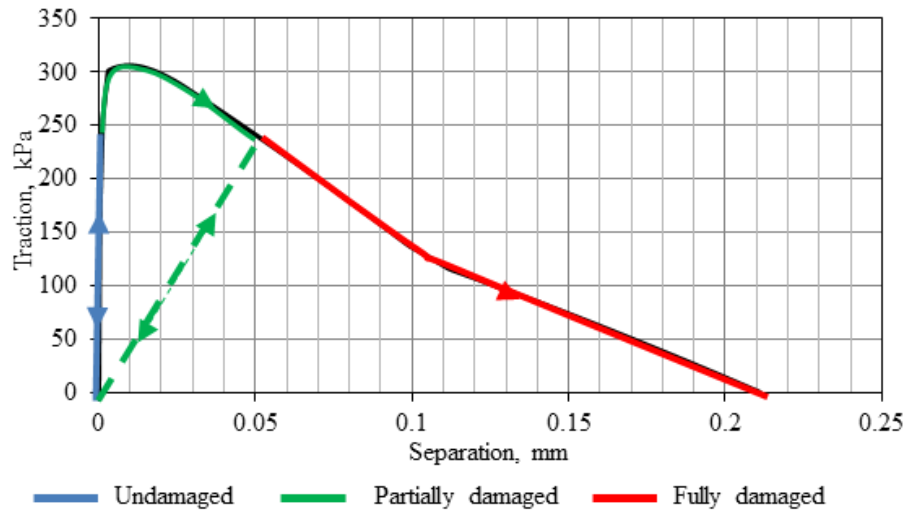
Figure 5.9. Loading-unloading paths for the cohesive elements.

The cohesive-zone based finite element model is capable of searching the distribution of undamaged, partially-damaged and fully-damaged elements across the concrete/asphalt interface in order to achieve the equilibrium at each time step. As a result, the damage history of the interfacial bond can be obtained. However, the damage would stop growing after the asphalt creep becomes steady. Because the cohesive elements were not assigned with any fatigue characteristic, repetition of the fatigue loads would only result in the elastic deformation of the elements at their original/degraded stiffness. Therefore, it is necessary to manually update the geometry of the interface elements according to the debonding determined from the nondestructive testing in order to calculate the fracture energy at different crack depths.

The damage of the interface was calculated when one cycle of the half-sine load in Figure 5.3 was applied in the model. As an example, the contour of the damage variable $SDEG$ at four crack depths is presented in Figure 5.10.
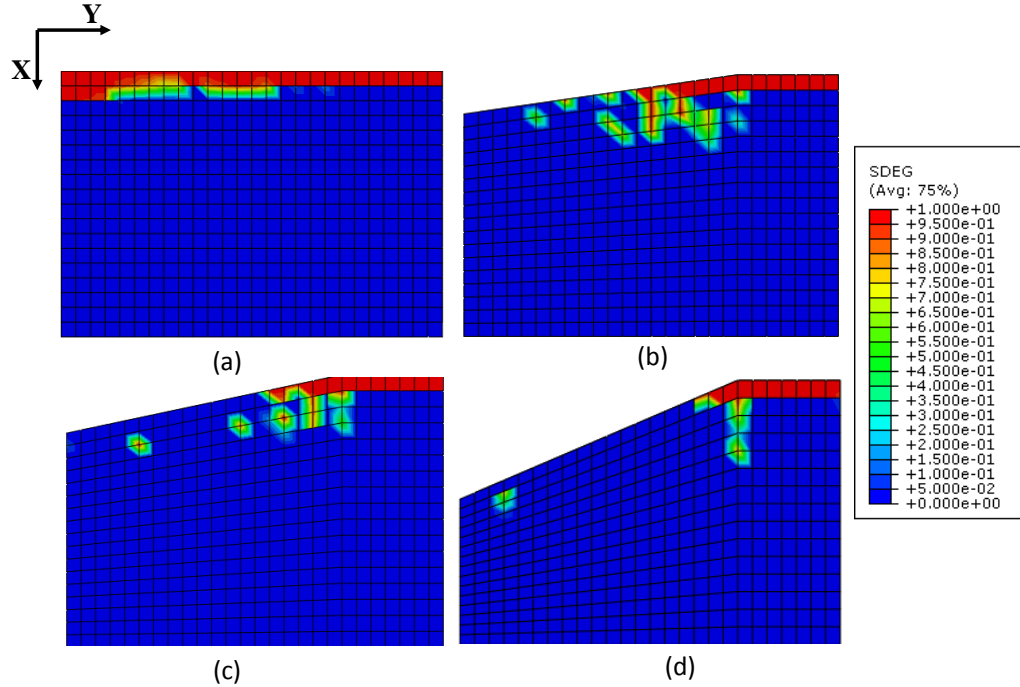
Figure 5.10. Contour of the damage variable for the cohesive elements of Slab 2 at the beginning of (a) 0, (b) 20,000, (c) 100,000 and (d) 1 million.

It is apparent that the influenced area of one individual load is a function of the crack depth. The damage decreases when the existing crack is large, indicating that the fracture energy dedicated to the fatigue of the interface also decreases as the interface debonding grows. This phenomenon explains why the debonding should eventually cease.

The fracture energy that is subjected to the slab by each individual load can be calculated using Equation (5.2).

$$\Delta G = \sum_{A_j \in A_D} \left(\int_0^{\delta_p} SDEG(\delta) \cdot E_0 \cdot \delta d\delta - \frac{SDEG(\delta_p) \cdot E_0 \cdot \delta_p^2}{2} \right) \frac{A_j}{h_{coh}} \tag{5.2}$$

where A_D is damaged area; A_j is the area of an element; δ_p is the historical maximum separation and h_{coh} is the original thickness of the cohesive elements.

The calculated ΔG for the ALF test is presented as a function of the delaminated area in Figure 5.11. The decreasing trend of ΔG in Figure 5.11 agrees with the conclusion from Figure 5.10.
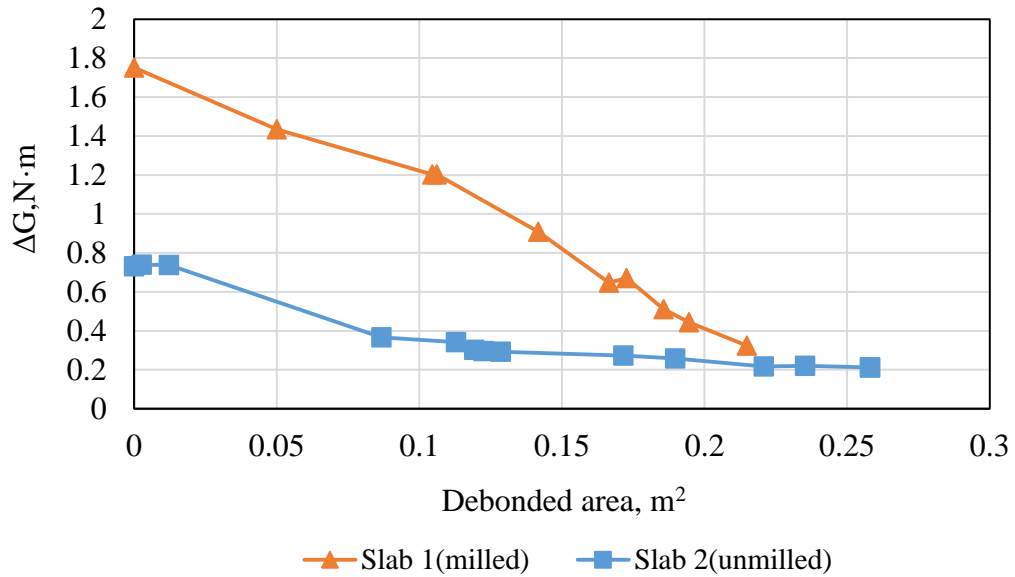
Figure 5.11. Fracture energy vs. delaminated area.

Another observation is that the fracture energy is much higher for the milled slab than the unmilled slab. For example, in Figure 5.11, the ratio of energy between the milled and unmilled slabs at zero damage is approximately 2.7. However, the size of the damaged area is very similar between the milled and unmilled slabs as shown in Figure 5.12. Therefore, the difference in the fracture energy is due to the fact that more fracture energy is needed to achieve the same damage for the cohesive elements of the milled slabs, as can be concluded by comparing the traction-separation laws in Figure 5.8.
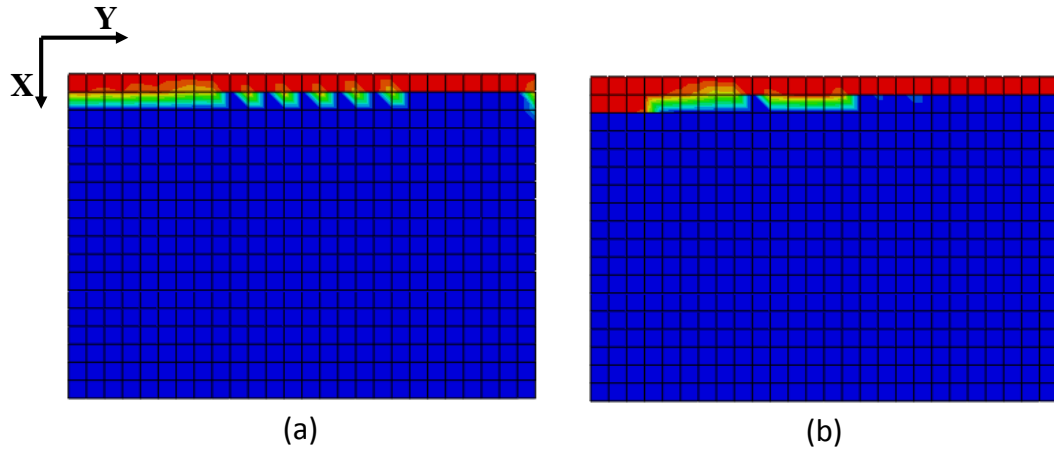
Figure 5.12. Comparison of damaged area between (a) milled and (b) unmilled slabs in the ALF test.

5.5 ESTIMATION OF INTERFACE DEBONDING FOR IN-SITU BCOA

A second finite element model was developed to calculate the fracture energy for in-situ BCOA slabs, as shown in Figure 5.13.
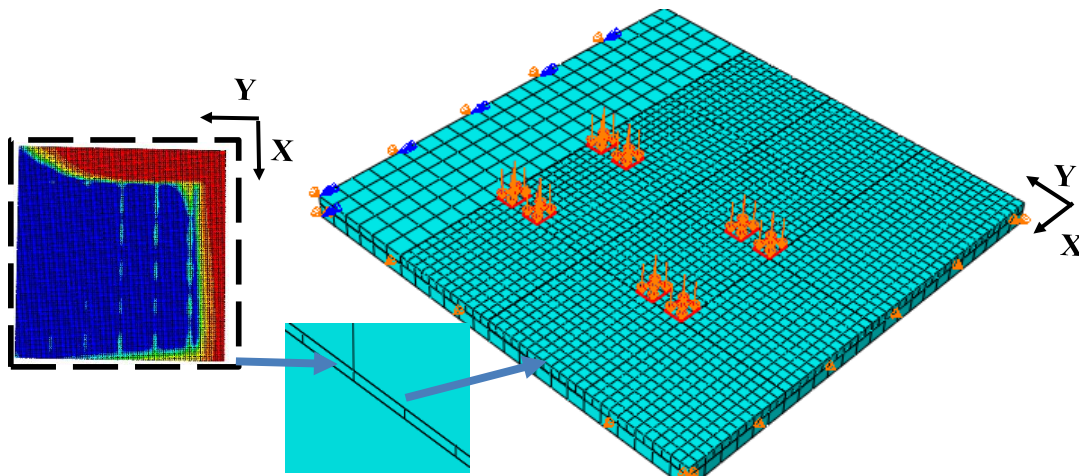
Figure 5.13. Cohesive-zone finite element model for in-situ BCOA slabs.

In the model, 16 slabs were used to simulate a 4.8m×3.6m section of a traffic lane. In addition, an asphalt shoulder of 1.2 m wide was included. Both the concrete slabs and the asphalt

shoulder were underlain by a continuous asphalt layer. A dual-tire tandem axle with tire pressure of 0.62 MPa was employed for the loading, following the suggestion of Li and Vandenbossche (2013).

Cohesive elements were only used for the center slab of the first row in Figure 5.13, for two reasons. First, the damage of the interface for this slab is most critical relative to the others. To demonstrate this, the damage contour was obtained for the scenario where cohesive elements were used for the six slabs at the first two rows, as presented in Figure 5.14. The most damage can be found at the center slab of the first row. Although the shape of the damaged area in Figure 5.13 is different from its counterpart in Figure 5.14, the size of the area is more or less the same. For simplicity, the interaction only between the loaded slab and the adjacent unloaded slab and its effect on the shape of the damaged area (damage flow) will be discussed. Second, the solution for the facture of cohesive elements is very computationally consuming and the usage of cohesive elements only for the critical slab makes the computation affordable.
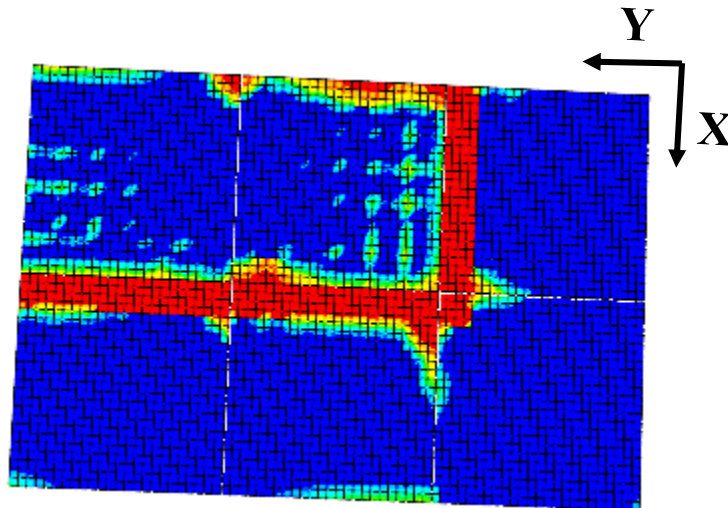
Figure 5.14. Damage contour when cohesive elements used for six slabs.

The fracture energy at zero interface debonding was estimated for various scenarios as summarized in Table 5.4. The benchmark model was constructed with a 100 mm concrete, 150

mm asphalt, and a subgrade k-value of 55 kPa/mm. The Young's modulus for the concrete was 26 GPa and the asphalt dynamic modulus at 21 °C and 1 Hz was determined to be 3.5 GPa. In the benchmark model, 40-kN wheel load was used and zero load transfer across the concrete joints was assumed.

Table 5.4. Fracture energy at zero debonding for various in-situ BCOA structures.

		Fracture energy at zero debonding, N·m		Percentage debonding @ 2 million for Milled and 1 million for Unmilled		Percentage increase of critical stress due to debonding	
		Milled	Unmilled	Milled	Unmilled	Milled	Unmilled
Wheel load	80 kN	13.6	5.9	100%	100%	149%	149%
	40 kN	0.4	1.6	4%	39%	18%	137%
	4.5 kN	0.00002	0.00001	0%	0%	0%	0%
k-value	138 kPa/mm	0.3	0.6	3%	15%	13%	79%
	55 kPa/mm	0.4	1.6	4%	39%	18%	137%
	28 kPa/mm	0.6	4.6	5%	100%	25%	149%
$\|E^*\|$ @ 21 °C and 1 Hz	7 GPa	0.3	0.7	3%	16%	13%	83%
	3.5 GPa	0.4	1.6	4%	39%	18%	137%
	1.4 GPa	0.8	1.6	7%	38%	29%	136%
Concrete thickness	100 mm	0.4	1.6	4%	39%	18%	137%
	75 mm	0.7	3.1	6%	75%	28%	154%
Asphalt thickness	225 mm	0.6	4.0	5%	98%	23%	150%
	150 mm	0.4	1.6	4%	39%	18%	137%
	75 mm	0.3	0.6	3%	15%	12%	78%
Load transfer at joints	0	0.2	1.1	4%	39%	18%	137%
	100%	0.1	0.2	1%	4%	12%	39%

The comparisons of all the scenarios to the benchmark case yields the following conclusions. First, the fracture energy increases with increased wheel load, decreased subgrade support, decreased asphalt stiffness, decreased concrete thickness, and increased asphalt thickness. The first four factors affect the fracture energy by inducing more differential deflection at the interface of the unloaded slab. On the other hand, although the increase in the asphalt thickness

reduces the stiffness of the composite layer, thereby resulting in smaller deflection on the loaded slab, it enhances the deflection transfer from the loaded side to the unloaded side. The net effect in increasing the asphalt thickness results in a higher fracture energy. Second, the fracture energy for the milled slabs is significantly lower than the unmilled slabs. Unlike for the restrained ALF slabs, the damaged zone for the in-situ slabs is smaller when the asphalt is milled as demonstrated in Figure 5.15 (a) and (b), resulting in a smaller fracture energy dedicated to the interface fracture. However, there are a few cases where the damage zone is activated to the same size regardless of the milling condition. For example, when the load is high as shown in Figure 5.15 (c) and (d), the fracture energy for the milled slab is higher, 13.6 N·m relative to 5.9 N·m for that of the unmilled slab. Third, the fracture energy is most sensitive to the wheelload. When the wheelload is twice that used in the benchmark model, the fracture energy increased by 4-35 times. On the other hand, when the wheel load is small as for the passenger cars, the fracture energy becomes negligible. Finally, it is very important to improve the load transfer efficiency across the concrete joints in order to alleviate the interface debonding. The fracture energy is significantly reduced by 50%-80% for milled and unmilled slabs, respectively, when the load transfer efficiency increases from 0 to 100%.
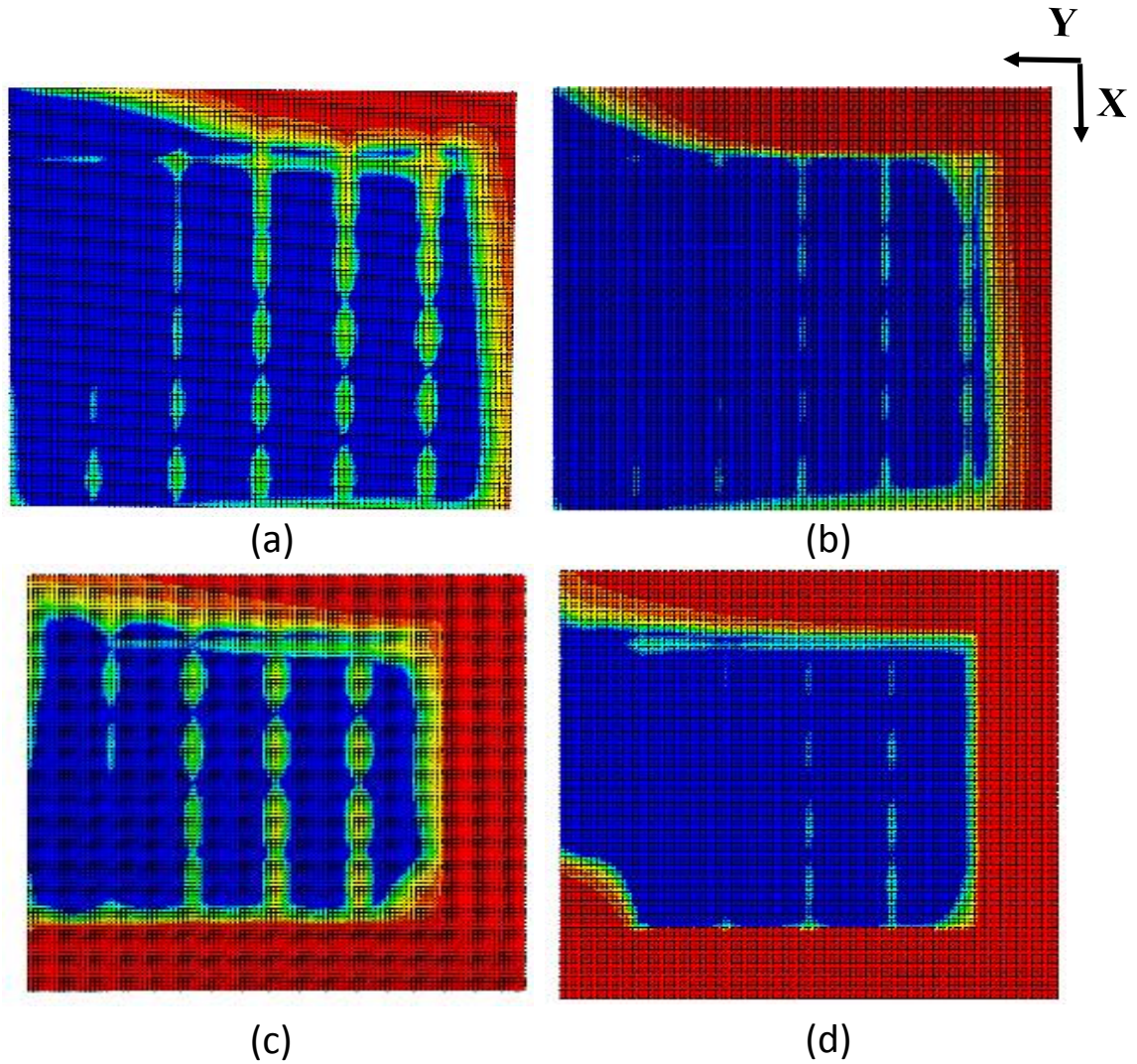
Figure 5.15. Damage zone for the in-situ BCOA slabs with (a) milled asphalt and 40 kN wheelload, (b) unmilled asphalt and 40 kN wheelload, (c) milled asphalt and 80 kN wheelload, (d) unmilled asphalt and 80 kN wheelload.

5.6 EFFECTS OF INTERFACIAL DEBONDING ON THE CRITICAL STRESS IN THE BCOA

If it is assumed that the area of debonding at the end of any fatigue loading is solely a linear function of the initial (at zero debonding) fracture energy, the area of debonding for the in-situ

slabs can be predicted based on the area-energy relationship for the ALF slabs from Figure 5.11. In Table 5.4, the area of debonding was estimated for the milled and unmilled in-situ slabs after 2 million and 1 million loads, respectively. It was calculated by first comparing the initial fracture energy of the in-situ slabs to the ALF slabs and then multiplying their ratio to the area of debonding of the ALF slabs at the end of the testing. However, if the delaminated area is larger than the slab size, i.e. 1.2 m×1.2 m, it is considered to be 1.44 m^2. Again the shape of the debonded area is not the focus of this discussion.

The existence of the interface debonding influences the critical stress in the BCOA overlay. In order to quantify the effect of the interface debonding on the critical stress in the overlay, a finite element model similar to the in-situ benchmark model in Figure 5.13 was developed, but with no cohesive elements. Tie constraints were used at the concrete/asphalt interface to represent a bonded condition and the growth of the debonding was simply formed by decreasing the area of the tie connections. The critical stress in the overlay was always extracted from the wheelpath at the bottom of the overlay. The relationship between the percentage of interface debonding and the critical stress in the overlay was established and presented in Figure 5.16. It can be seen that the critical stress in the overlay is very sensitive to the interface debonding. It is increased by 100% after the interface debonds over approximately 20% of the total area.

The increase in the critical stress due to the interface debonding was then evaluated for the in-situ slabs and the results are presented in Table 5.4. On average, the critical stress increases by 10%-30% for the milled slabs after 2 million loads and 80%-150% for the unmilled slabs after 1 million loads. When there is 100% load transfer at the joints, the stress increase becomes 10% and 40% for the milled and unmilled slabs, respectively. The percentage increase in the critical stress from this study seems to be able to support the proposed values suggested by other researchers,

105

recalling that Tarr et al. (1998) proposed 50%-60% and Wu et al. (1999) suggested 20%-60% for the increase of the stress.
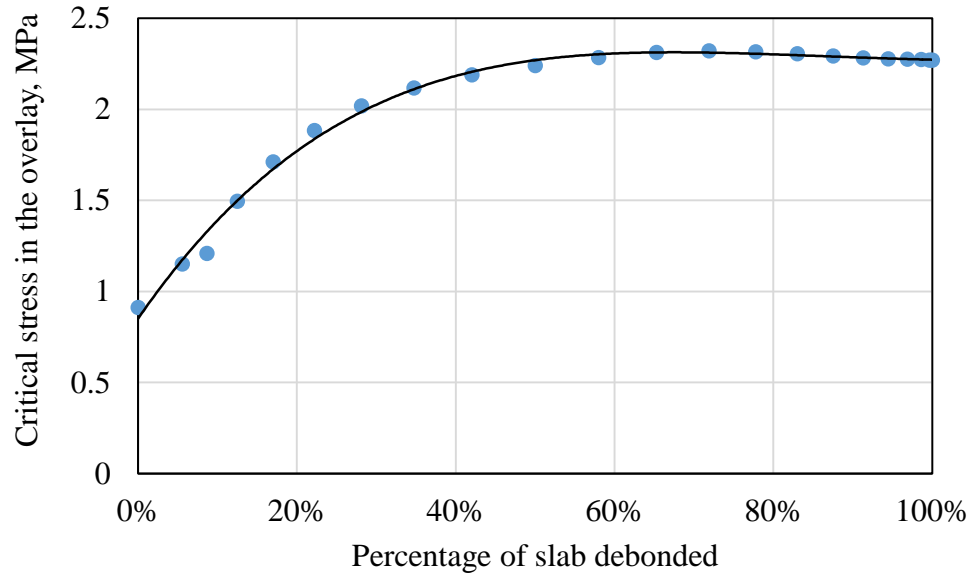
Figure 5.16. Relationship between the percentage of slab debonded and the critical stress in the overlay.

An incremental stress analysis is often used for the design of BCOA, where the critical stress in the overlay is calculated hourly based on hourly-updated climatic and traffic data. In order to incorporate the debonding analysis presented earlier into the incremental stress analysis, the ALF test results were also used to establish the growth rate of the interface debonding as a function of the fracture energy, as presented in Figure 5.17.

For the unmilled slab, the growth rate of the debonding was very small for the first 20k loads even when the fracture energy was very high. This slow initiation of the debonding was most likely because that the fatigue energy was initially otherwise utilized, such as the dissipation for seating the test setup. It might be more reasonable to exclude the two data points of the unmilled slab prior to 30 k from the regression analysis.
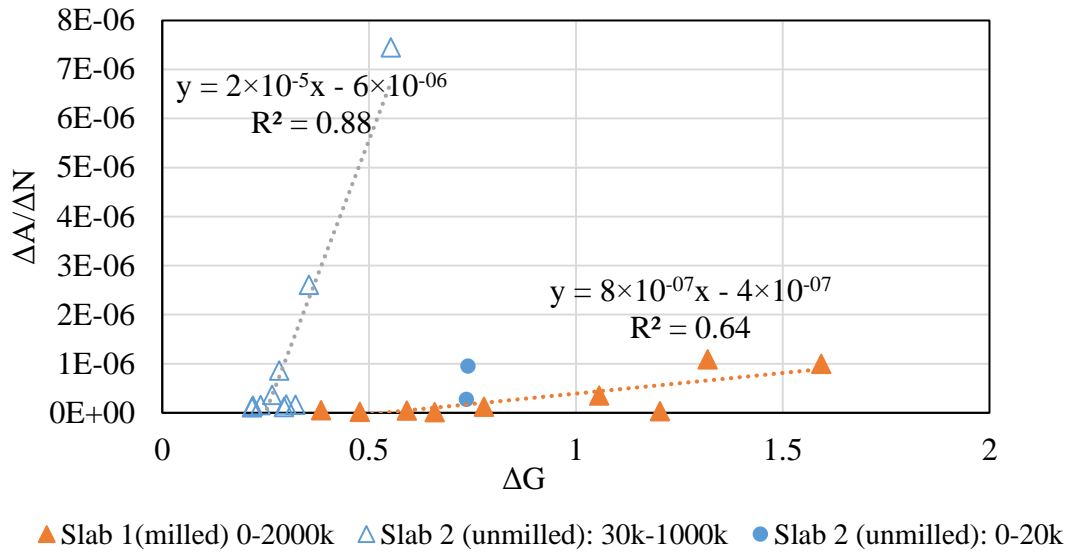
Figure 5.17. Relationship between the growth rate of interface debonding and the fracture energy.

The flowchart presented in Figure 5.18 illustrates how the development of interface debonding and its effect on the critical stress in the overlay can be incorporated into the incremental stress analysis for BCOA design.
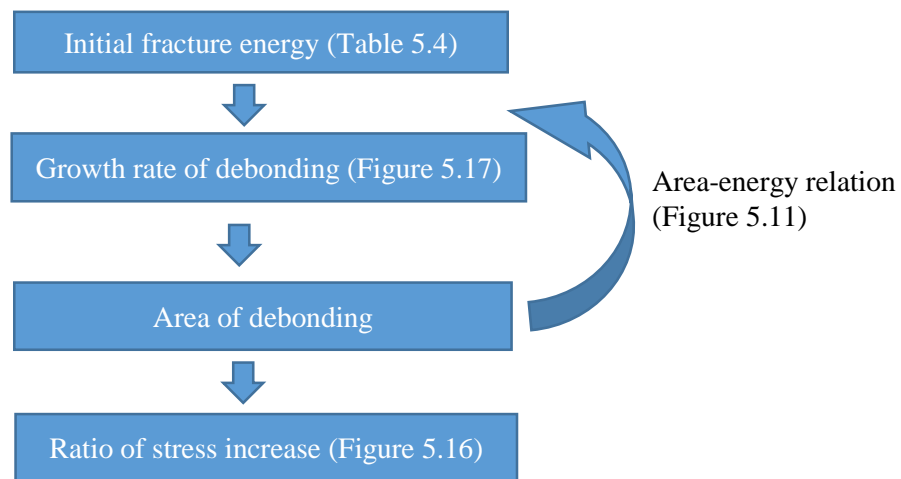
Figure 5.18. Flow chart for considering the interface debonding into the incremental stress analysis for BCOA design.

First, the initial fracture energy can be estimated for the specific BCOA to be designed or interpolated from the scenarios presented in Table 5.4. Next, the growth rate of the debonding for the first increment of the fatigue loads can be estimated from Figure 5.17, so that the area of debonding at the end of the increment can be calculated. Finally, the increase in the critical stress due to the increment of fatigue loading can be estimated based on Figure 5.16. For the next increment of fatigue loading, the updated fracture energy can be found from the area-energy relationship in Figure 5.11.

5.7   CONCLUSIONS

In this study, the development of the interfacial debonding for BCOA due to fatigue loading was quantified based on the accelerated loading test of large-scale BCOA slabs. The growth of the interface debonding was monitored using nondestructive methods and the results were validated by comparing to the destructive examination of the interface debonding at the end of the ALF test. Relationship between the area of debonding and the number of fatigue loads was established for BCOA slabs with milled and unmilled asphalt. It was found that the area of debonding grew with the fatigue loads but in a decreasing rate. The growth rate for the milled slab was smaller than the unmilled slab.

The fracture energy responsible for the interfacial debonding was calculated using a cohesive-zone based finite element model. The traction-separation law for both milled and unmilled interfaces were established from the wedge splitting test of small BCOA blocks. It was found that the fracture energy decreased with increased crack depth, which explains the decreasing rate for the interface debonding observed in the ALF test. The fracture energy for the milled slab

was higher than the unmilled slab for the slabs tested in the ALF. This, together with the slower growth rate for the milled slab, suggests that milling of the asphalt is very effective in providing longer fatigue life for the interfacial bond.

The fracture energy for a combination of in-situ slabs were calculated using finite element analysis, based on which the debonding area for these slabs could be estimated assuming that the fatigue mechanism for the in-situ slabs was similar to that for the ALF tested slabs. It was found that the interface debonding was very sensitive to traffic loading and joint load transfer. It also increased with increased wheel load, decreased subgrade support, decreased asphalt stiffness, decreased concrete thickness, and increased asphalt thickness.

In this paper, a framework was also proposed to incorporate the established fatigue algorithm into the incremental stress analysis for BCOA design. In the framework, the fracture energy is a function of the delaminated area and the growth rate of the interfacial debonding depends on the magnitude of the fracture energy as well as the number of fatigue loads. A third finite element model was employed to derive the relationship between the size of the interface debonding and the increase of critical stress in the overlay, so that the critical stress in the overlay can be updated as a function of the number of fatigue loads. When there is zero load transfer at the joints, the proposed framework predicts an increase of the critical stress by 10%-30% for milled slabs after 2 million loads and 80%-150% for unmilled slabs after 1 million loads. When there is 100% load transfer, the increase of the stress significantly decreases to 10% and 40% for the milled and unmilled slabs, respectively.

Some components of the proposed framework can be further improved. For example, the assumption that the fatigue performance is the same between the ALF tested slabs and the in-situ

109

slabs should be examined, as more testing data and field performances become available. The interaction between slabs could also be evaluated in future work.

6.0   CONCLUDING REMARKS AND FUTURE WORK

A fracture mechanics based framework has been developed and validated to determine the growth of interface debonding for Bonded concrete overlay of asphalt (BCOA) under fatigue loading and to incorporate the fatigue mechanism into the BCOA design. For the first time, the degree of debonding is defined as the delaminated area at the interface of BCOA. The framework includes four main components, namely two customized laboratory tests and two new methods. For the laboratory tests, on one hand, wedge splitting tests of small BCOA specimens were carried out to investigate the interface fracture resistance and its sensitivity to many factors such as initial crack depth, specimen size, and asphalt milling. On the other hand, large-scale BCOA slabs were tested in the accelerated loading facility to simulate the interface fracture under fatigue loading. A new nondestructive test method based on transient-wave analyses was developed to determine the growth of the interface debonding during the fatiue loading, and a cohesive zone model (CZM) was established in the finite element environment to calculate the fracture energy for the interface debonding.

The framework is capable of estimating the interface fracture energy subjected by a wheel of any load on BCOA slabs using the developed CZM. The traction-separation law of the CZM was obtained from the wedge splitting tests that is customized to create interface fracture of BCOA specimens under mode I loading. Six major types of failure were identified by examining the fractured BCOA specimens, namely the failure of concrete adhesion to asphalt matrix, the failure of concrete adhesion to exposed/crushed aggregate, aggregate breakage/pullout, and asphalt fracturing. Five root CZMs were then proposed to simulate the complicated fracture behavior of any BCOA interface by simply superimposing the root CZMs. The fracture properties of the root

CZMs were obtained based on an inverse analysis using the wedge splitting test results. The properties are material dependent and independent from the composition of the interface, i.e. the milling effect, so that they can be used to model the debonding of BCOA on different scales.

The framework can also determine the growth of the interface debonding as a function of the fracture energy subjected by an individual load as well as the number of fatigue loads. For BCOA slabs tested in the accelerated loading facility, it was found that the area of interface debonding grew with the fatigue loads but in a decreasing rate. The growth rate for milled slabs is slower than that for the unmilled slabs. In order to relate the growth of the interface debonding to the magnitude of the fracture energy, the area of interface debonding during the accelerated loading tests was determined using the transient-wave based NDT method developed in this study. The validity of the transient-wave based method has been examined by a laboratory test in which the depth of the interface crack could be controlled as well as the destructive examination at the end of the accelerated loading tests. Particularly the transient-wave based NDT method is shown to yield more accurate predictions when compared to a deflection based NDT method.

Eventually, the framework shows that the increase in the critical stress in the overlay can be proportionally related to the area of interface debonding. Therefore, the growth of interface debonding under fatigue loading can be taken into account for the design of BCOA. Using the framework, the interface debonding as well as the design stress in the overlay was predicted for a combination of in-situ slabs. It was found that the interface debonding was very sensitive to traffic loading and joint load transfer. The interface debonding also increases with increasing wheel load, decreasing subgrade support, decreasing asphalt stiffness, decreasing concrete thickness, and increasing asphalt thickness.

However, certain extensions can be made in order for the framework to be more mechanistically sound and for the NDT method to be more applicable to in-situ investigation in general. First of all, the finite element model for computing the slab debonding can be upgraded by considering the interaction between slabs and between wheel loads. Second, the assumption that the fatigue rate for the laboratory accelerated loaded slabs is the same as the in-situ slabs should be examined, especially when more test data and field performance data become available. Third, the NDT method should be modified to account for the slab geometry and asymmetric boundary conditions. In order to make the NDT method more applicable to a field investigation, new technologies such as air-coupled sensors (Zhu and Popovics, 2007) can be employed to improve the accuracy, mobility, and efficiency of the test. Forth, the mechanical characterization of the interface fracture has been scoped to focus on the interface debonding due to mode I (tensile) loading in this study. The interface fracture due to mode II (shear) loading could be studied or at least computationally modeled. Although it is believed that the interface failure due to mode I should be critical, scenarios of mode II being predominant might still exist. Last but not least, the asphalt fracture in addition to the interface fracture was both observed from the accelerated loading tests and reported by previous research. A more comprehensive framework can be expected after employing the interaction between the interface fracturing and asphalt fracturing.

CHARACTERISTIC OF WEDGE SPLITTING TEST SPECIMENS

There are in total 23 specimens used in the wedge splitting tests, prepared in two batches, namely WST-2 and WST-S. The dimensions of the specimens as illustrated in Figure A. 1 were measured and presented in Table A. 1.
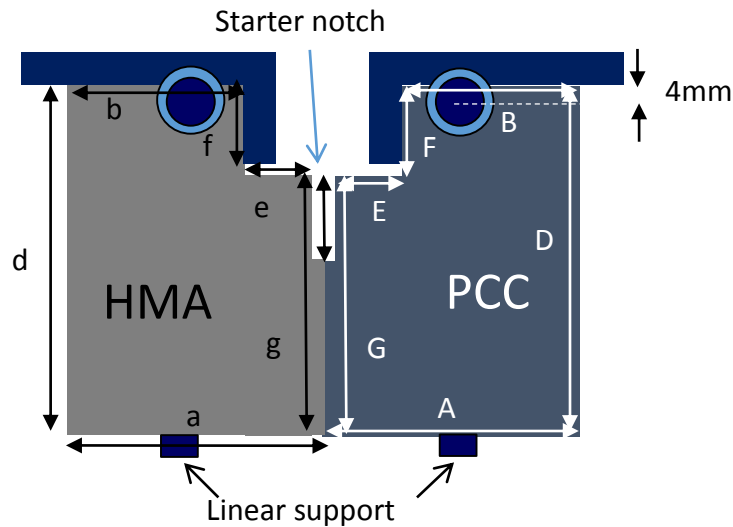
Figure A. 1. Sketch of the wedge splitting test configuration.

Specimens with various characteristics, i.e. specimen size, notch depth, curing time, surface roughness, milling direction, moisture condition, testing temperature, and loading rate, were tested to investigate the effects of these factors on the interface fracture. The term 'milling direction' refers to the angle between the direction of the milling grooves and the direction of the crack propagation.

The specimens tested in a dry condition were prepared by first placing the specimens in the curing room for 28 days and then they were air dried under room temperature until their weight

did not change. The specimens tested in a wet condition were saturated by placing them back in the curing room while monitoring the weight to insure they were maintained in a saturated condition. Some of the 'dry' specimens were placed in the freezer until their temperature stabilized at -15 °C and then they were tested to study the fracture at low temperatures.

Table A. 1. Characteristics of the WST specimens.

Specimen		2-01	2-02	2-03	2-04	2-05	2-06	2-07	2-08
Curing, days		28	29	29	186	186	186	28	28
Weight, kg		9.5	9.2	9.5	6.8	8.8	8.7	8.1	8.0
Dimension, mm	a	98	98	94	98	96	85	82	97
	A	106	108	105	102	101	91	99	110
	b	62	69	69	70	69	58	60	63
	B	74	81	81	81	75	69	70	82
	d	148	148	151	183	150	143	146	151
	D	149	149	152	145	150	144	147	153
	e	34	28	28	27	30	28	25	35
	E	33	26	23	23	26	24	27	28
	f	52	52	51	52	53	45	48	52
	F	52	52	52	54	53	45	47	51
	g	97	96	107	93	96	98	99	100
	h thickness	148	149	143	145	141	148	144	145
	H thickness	146	147	143	148	143	147	142	146
	Starter notch	10	10	14	16	15	9	10	14
	Guide notch	5	5	4	4	4	5	6	7
Milling		N	N	N	N	N	N	Y	Y
Milling direction		N/A	N/A	N/A	N/A	N/A	N/A	0	0
Roughness*, mm		0.48	0.58	0.56	0.84	0.56	0.56	0.97	1.73
Test condition		Dry	Dry	Dry	Forzen	Forzen	Forzen	Dry	Dry
Loading rate, mm/min		0.51	0.51	0.51	0.41	0.38	0.03	0.51	0.51

*measured using the sand patch test (ASTM-E965-96)

Table A. 1. (continued).

Specimen		2-09	2-10	2-11	2-12	2-13	2-14	2-15	2-09
Curing, days		28	186	186	28	29	186	29	28
Weight, kg		8.2	8.1	8.1	6.3	7.9	6.5	6.6	8.2
Dimension, mm	a	80	83	65	69	68	67	83	97
	A	100	96	80	110	78	78	99	110
	b	57	57	43	42	42	45	57	63
	B	71	68	45	78	51	50	73	82
	d	147	145	146	147	146	147	146	151
	D	145	147	145	145	148	150	148	153
	e	26	27	27	29	29	25	26	35
	E	26	27	29	27	28	31	27	28
	f	48	49	47	49	48	48	49	52
	F	49	48	45	49	48	49	48	51
	g	98	98	99	98	99	100	98	100
	h thickness	146	147	145	147	145	147	146	145
	H thickness	144	144	146	145	146	147	145	146
	Starter notch	10	9	17	17	14	11	10	14
	Guide notch	6	5	6	7	5	5	6	7
Milling		Y	Y	Y	Y	Y	Y	Y	Y
Milling direction		0	0	0	0	90	0	45°	0
Roughness, mm		1.47	1.52	1.65	1.73	2.11	2.16	2.01	1.47
Test condition		Dry	Frozen	Frozen	Dry	Dry	Frozen	Dry	Dry
Loading rate, mm/min		0.51	0.05	0.33	0.51	0.51	0.05	0.51	0.51

Table A. 1. (continued).

Specimen		S-01	S-04	S-10	S-11	S-12	S-13	S-14	S-15
Curing, days		163	189	163	163	189	163	189	163
Weight, kg		5.2	5.9	6.0	8.1	7.9	7.3	6.8	7.5
Dimension, mm	a	69	82	100	100	99	76	93	97
	A	74	70	85	84	85	76	87	110
	b	41	51	72	65	67	49	64	63
	B	49	43	62	61	65	48	61	82
	d	143	142	140	143	150	150	139	151
	D	145	144	141	144	151	152	141	153
	e	33	31	30	35	35	30	28	35
	E	23	27	23	26	24	28	28	28
	f	51	47	47	48	46	49	45	52
	F	51	48	48	49	47	50	45	51
	g	93	96	93	94	104	101	95	100
	h thickness	142	134	148	146	124	144	144	145
	H thickness	142	139	148	145	125	145	147	146
	Starter notch	18	18	12	14	28	14	43	14
	Guide notch	4	4	4	4	4	4	4	7
Milling		Y	Y	N	N	N	N	N	N
Milling direction		0	0	N/A	N/A	N/A	N/A	N/A	N/A
Roughness, mm		1.88	1.73	0.84	0.79	0.89	0.84	0.64	0.76
Test condition		Dry	Wet	Dry	Dry	Wet	Dry	Wet	Dry
Loading rate, mm/min		0.51	0.51	0.51	0.51	0.51	0.51	0.51	0.51

ANALYSIS OF WEDGE SPLITTING TEST UNDER DRY AND ROOM

TEMPERATURE CONDITIONS

The data for the specimens tested under dry and room-temperature condition was processed using

the model developed in Section 2.4. The results are presented in Figure B. 1 to Figure B. 14.
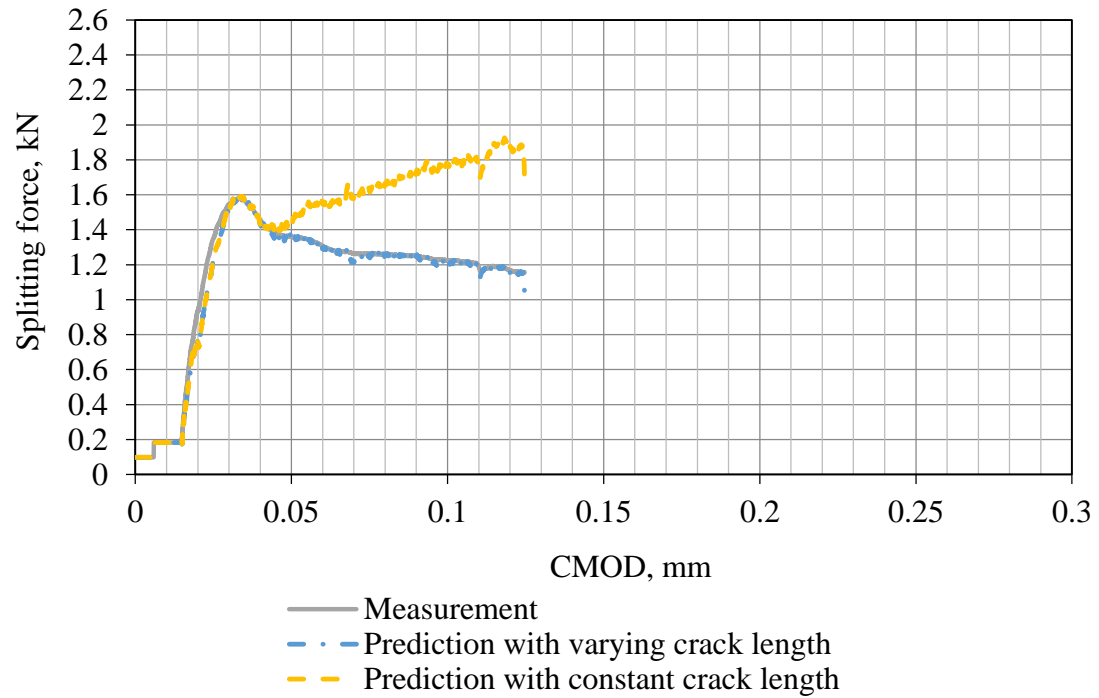
Figure B. 1. Measured and predicted load-CMOD curves for 2-07.
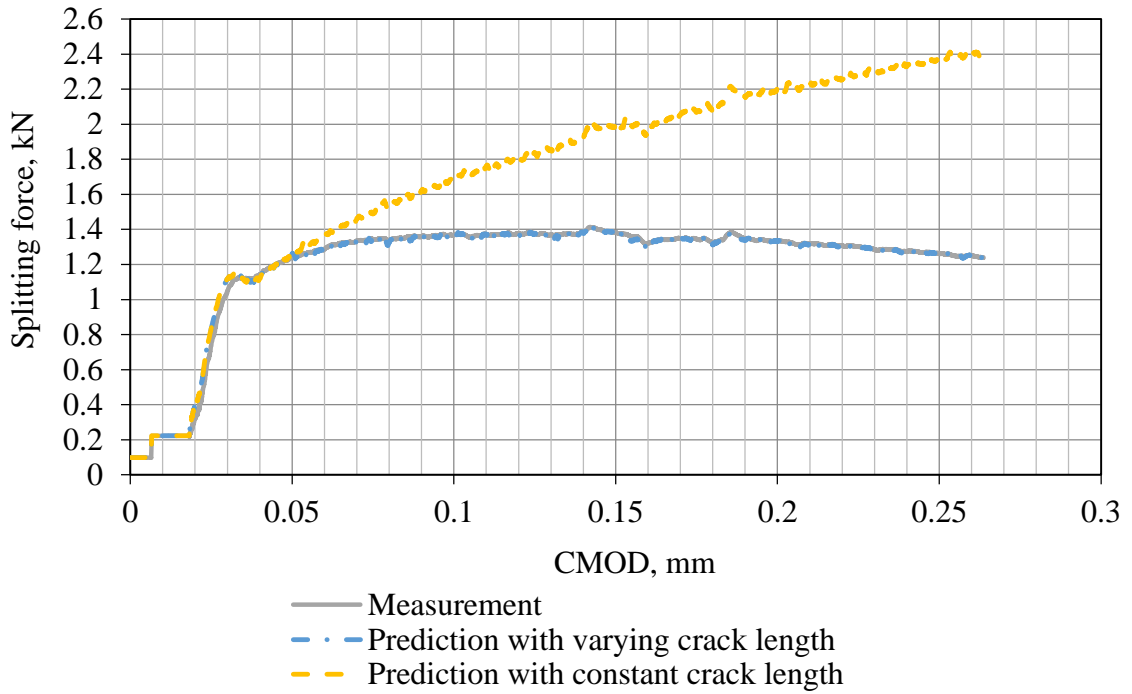
Figure B. 2. Measured and predicted load-CMOD curves for 2-08.
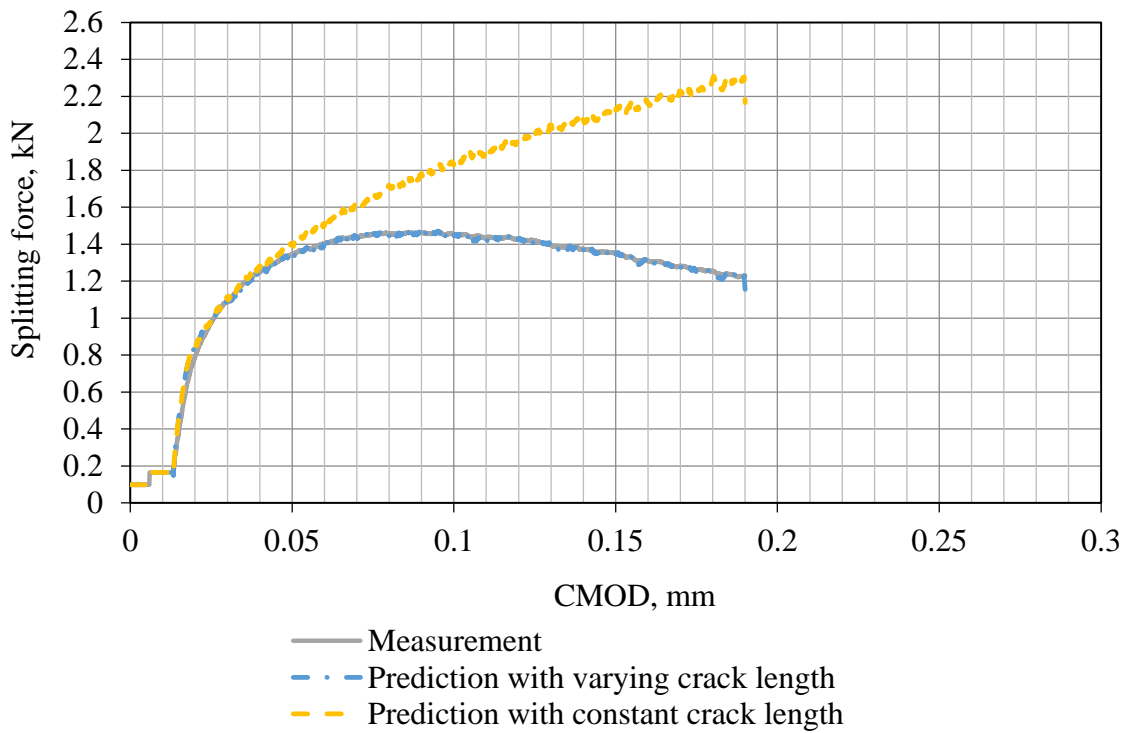
Figure B. 3. Measured and predicted load-CMOD curves for 2-09.
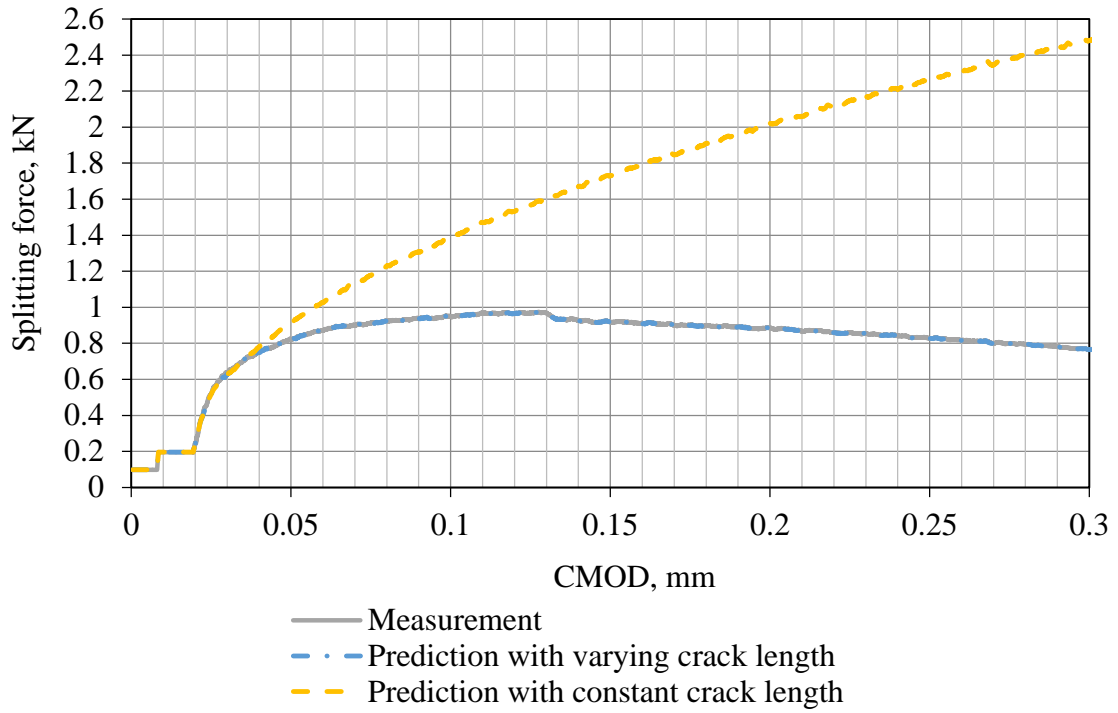
Figure B. 4. Measured and predicted load-CMOD curves for 2-12.
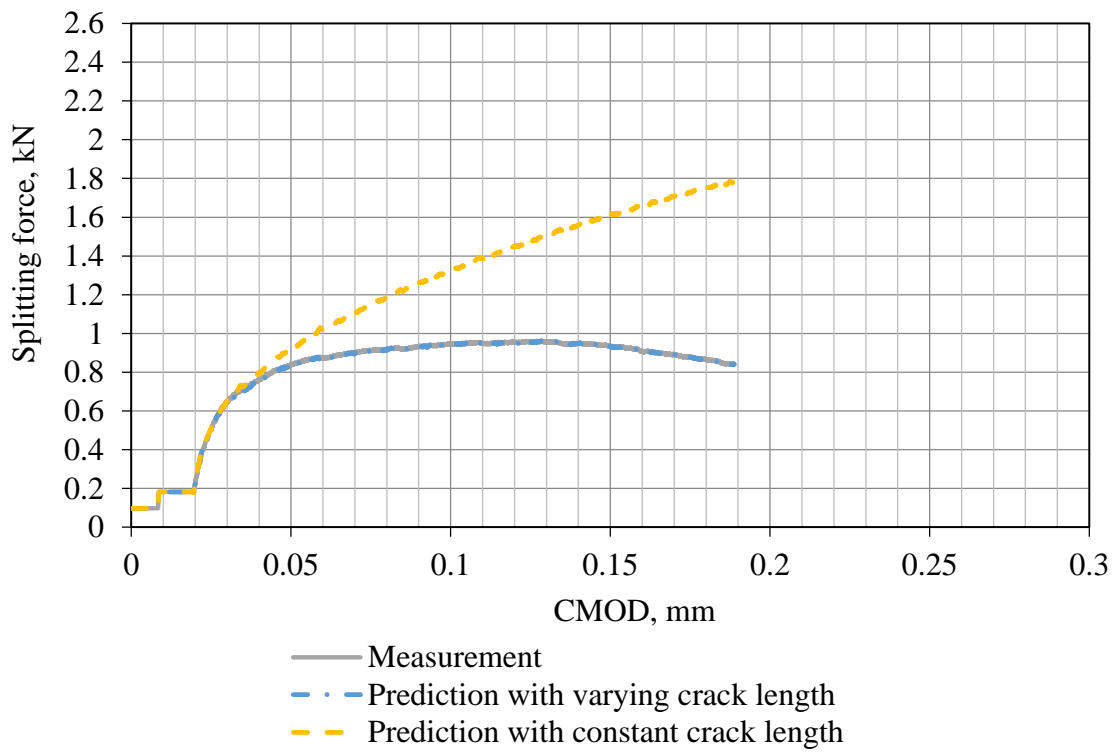
Figure B. 5. Measured and predicted load-CMOD curves for 2-13.
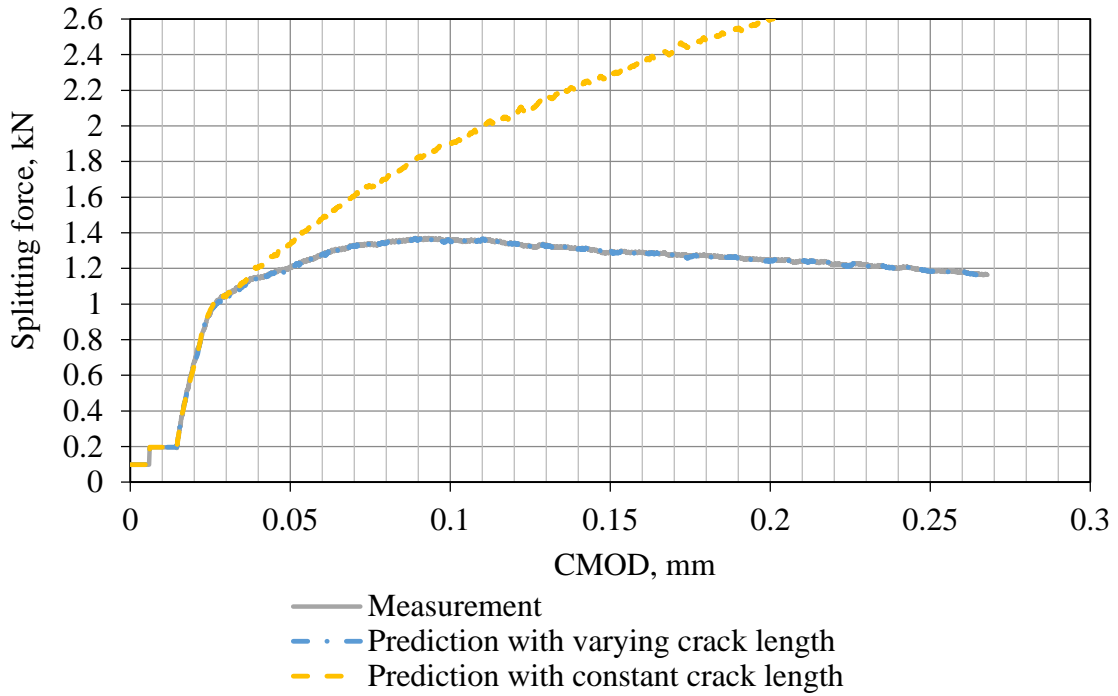
Figure B. 6. Measured and predicted load-CMOD curves for 2-15.
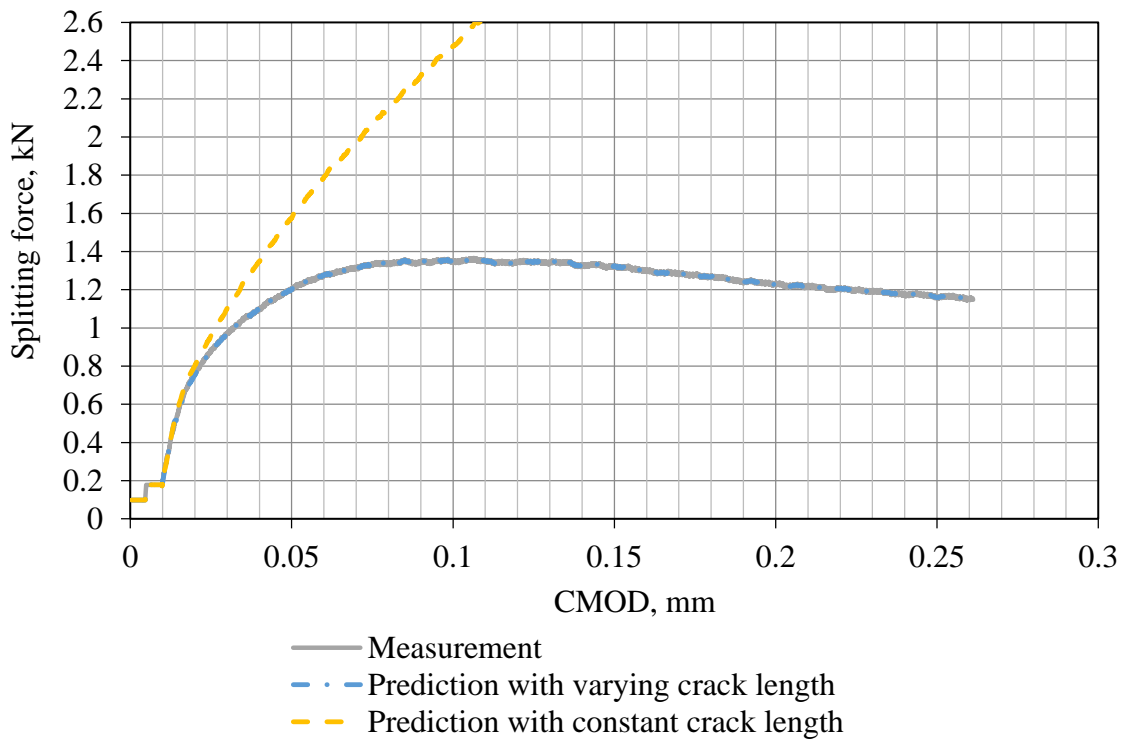
Figure B. 7. Measured and predicted load-CMOD curves for S-01.
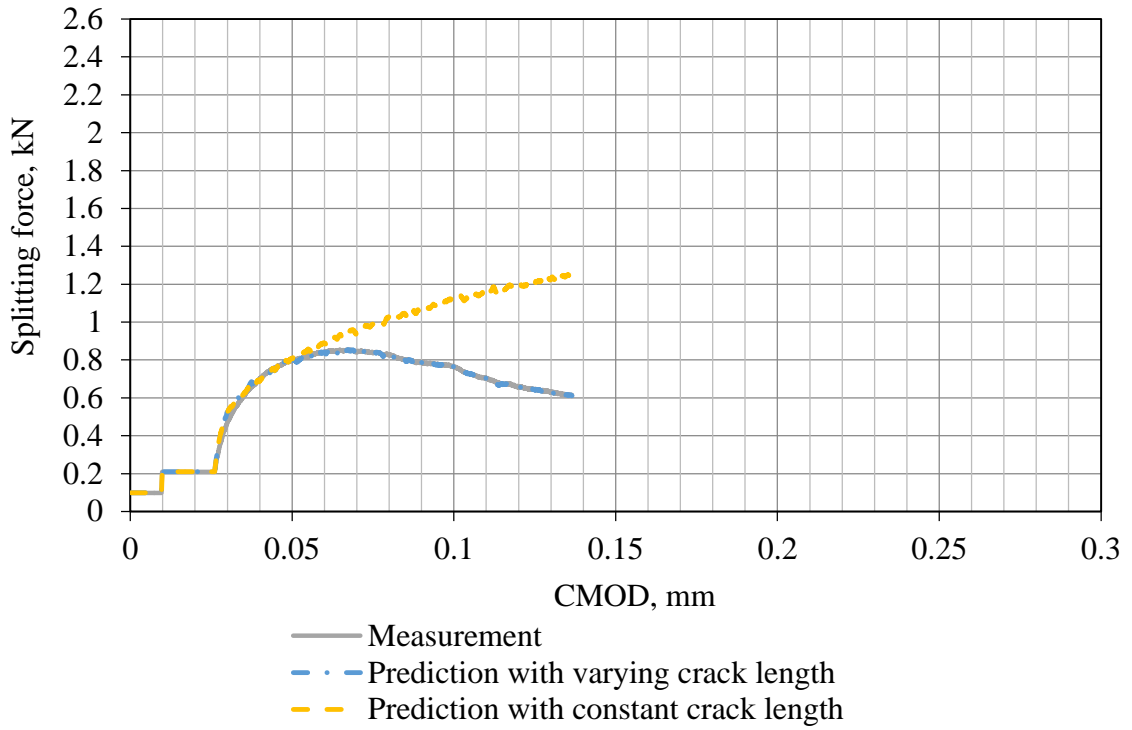
Figure B. 8. Measured and predicted load-CMOD curves for 2-01.
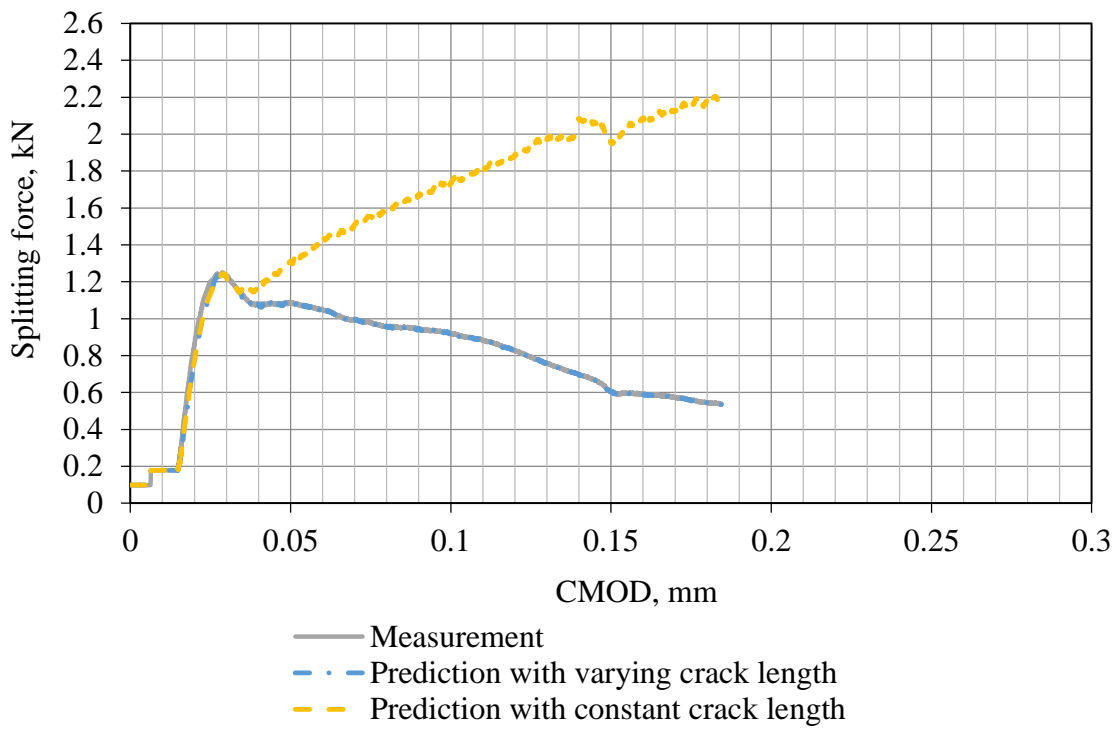
Figure B. 9. Measured and predicted load-CMOD curves for 2-02.
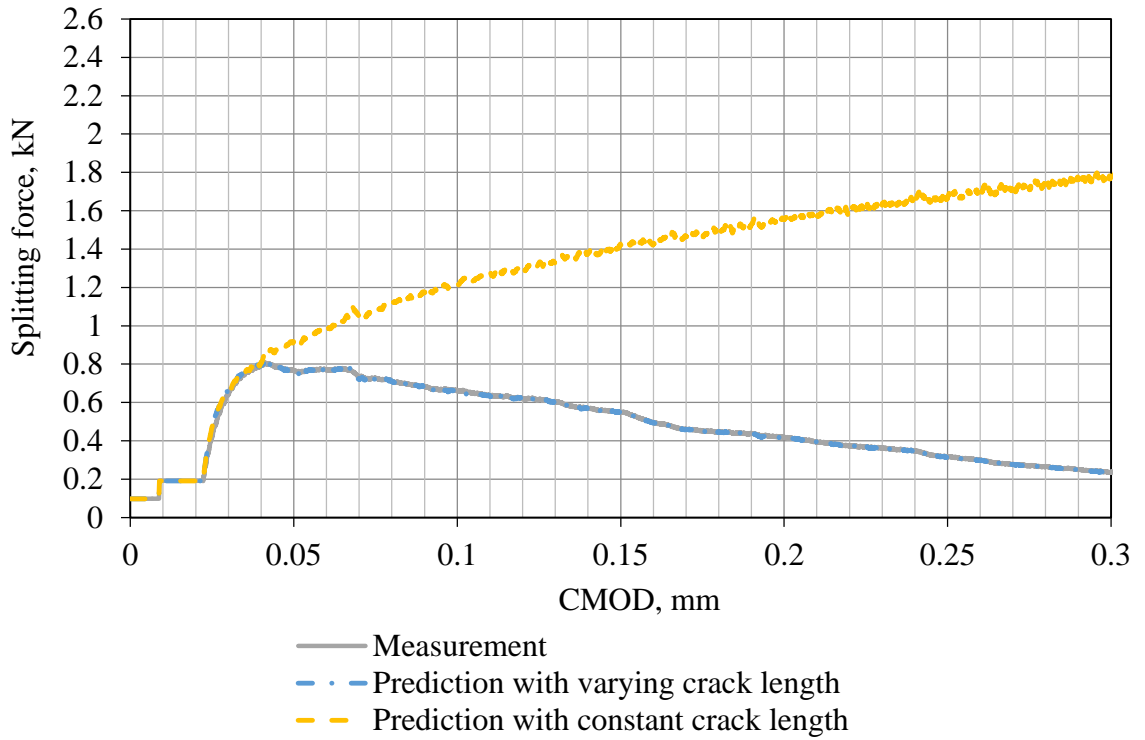
Figure B. 10. Measured and predicted load-CMOD curves for 2-03.
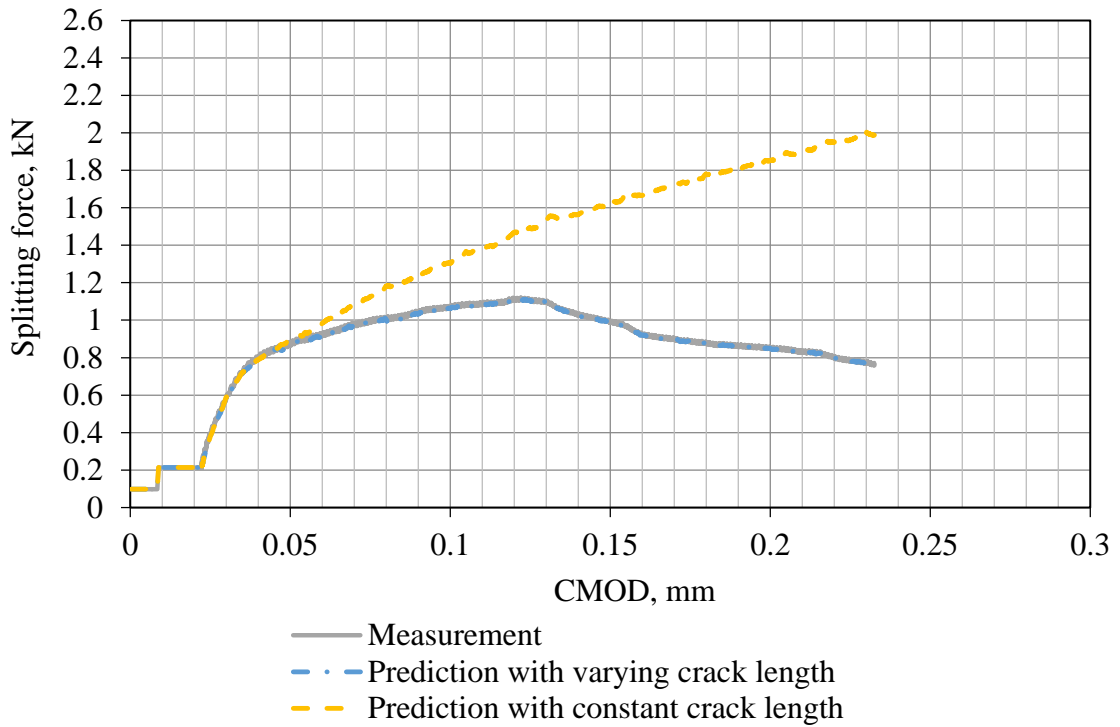
Figure B. 11. Measured and predicted load-CMOD curves for S-10.

123
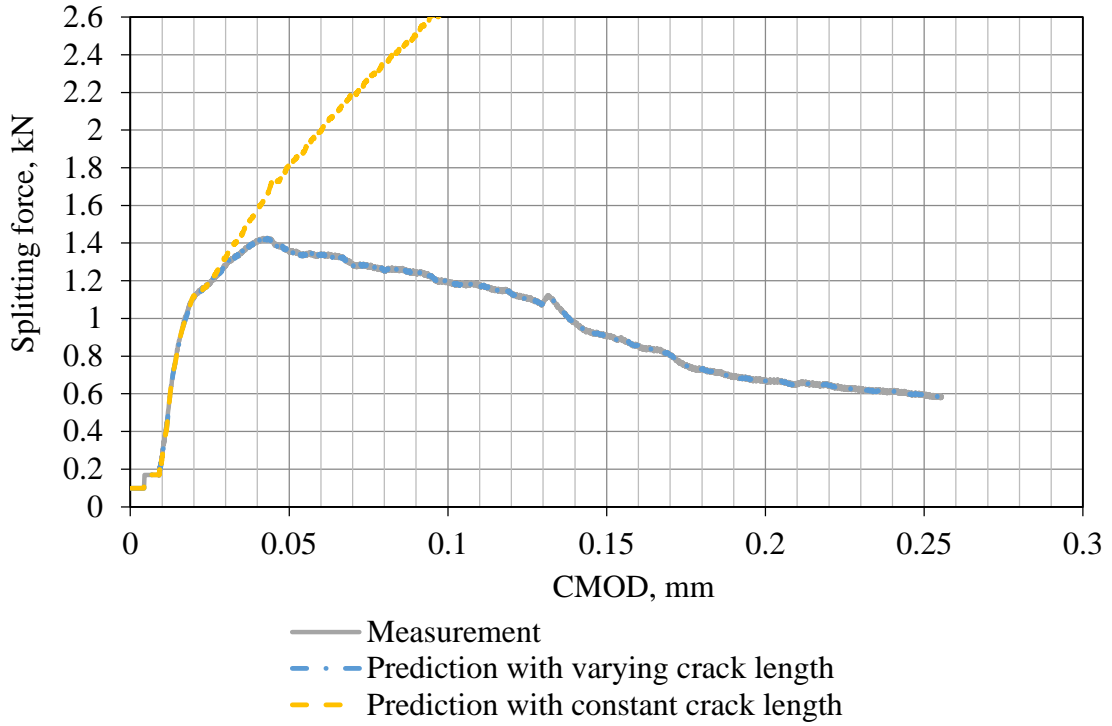
Figure B. 12. Measured and predicted load-CMOD curves S-11.
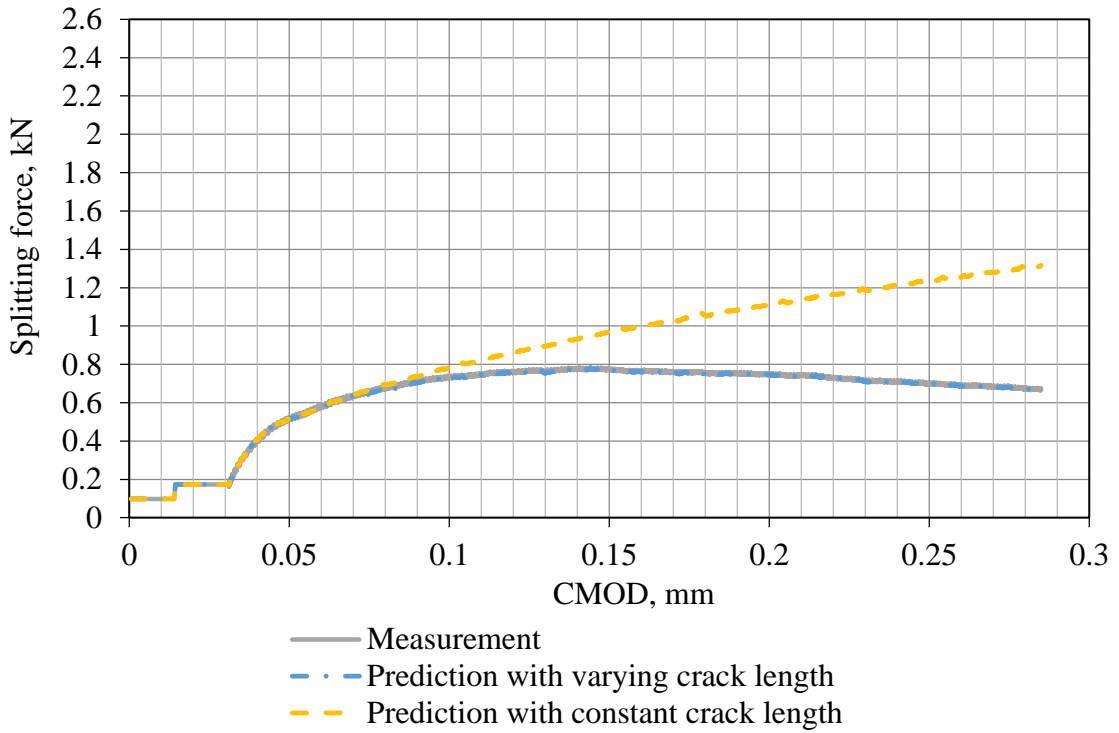
Figure B. 13. Measured and predicted load-CMOD curves for S-13.
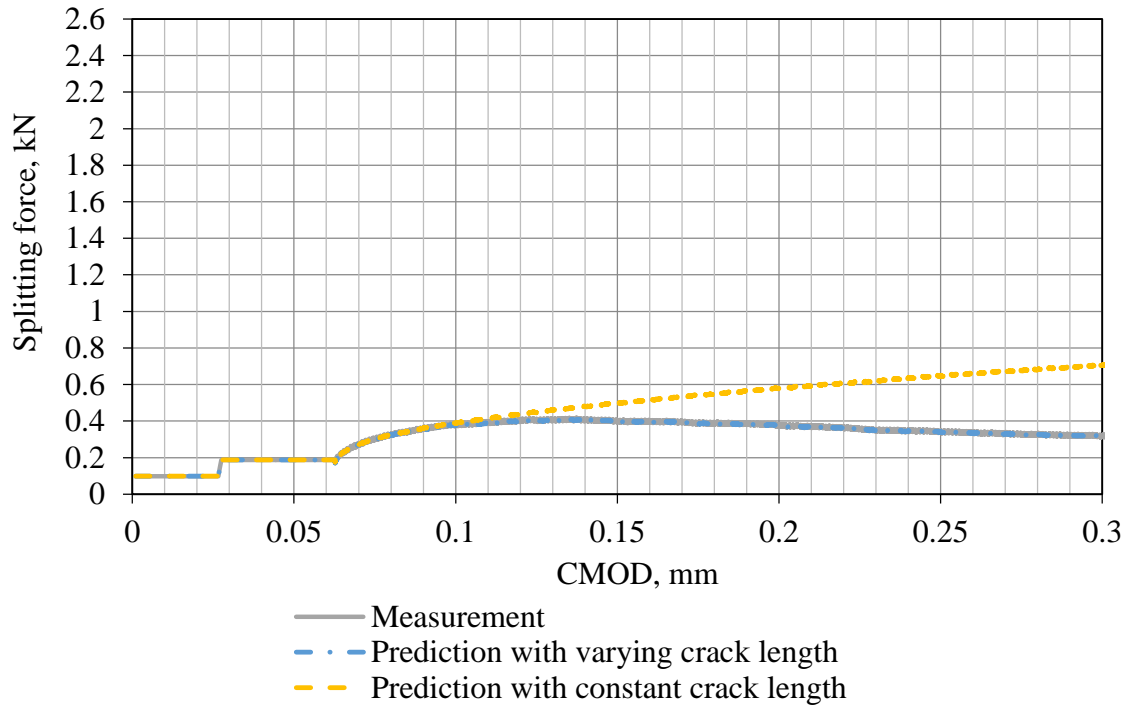
Figure B. 14. Measured and predicted load-CMOD curves for S-15.

ANALYSIS OF WEDGE SPLITTING TEST UNDER WET AND ROOM TEMPERATURE CONDITIONS

One milled (S-04) and two unmilled (S-12 and S-14) specimens were saturated before the testing. The weight of these specimens had been monitored, as shown in Figure C. 1. The specimens were considered saturated after 27 days as indicated by the negligible rate of weight gain after 27 days.
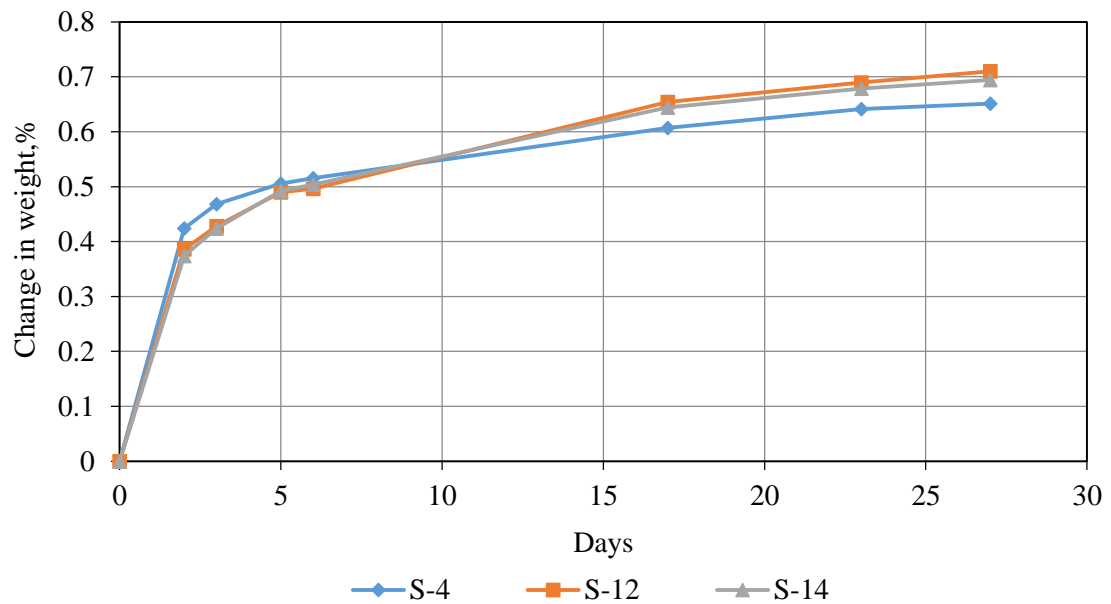
Figure C. 1. Weight gain curve for the wet specimens.

These specimens were tested under room temperature and the test data was processed using the model presented in in Section 2.4. The results are presented in Figure C. 2 to Figure C. 4.
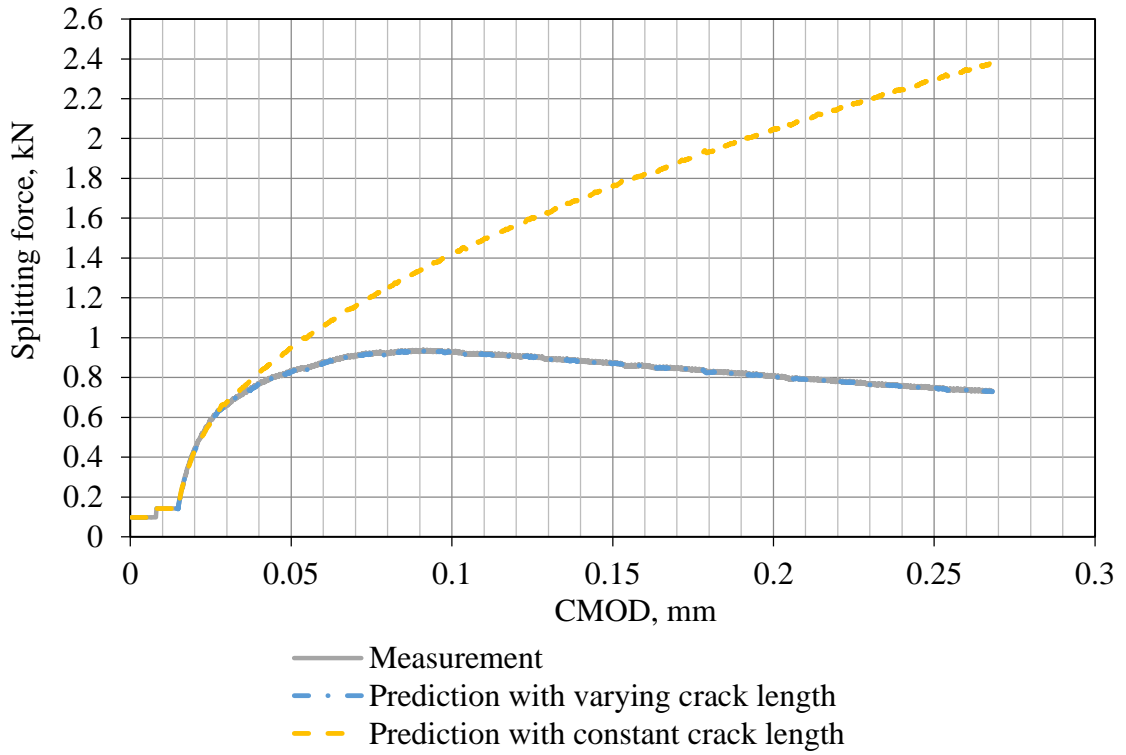
Figure C. 2. Measured and predicted load-CMOD curves for S-04.
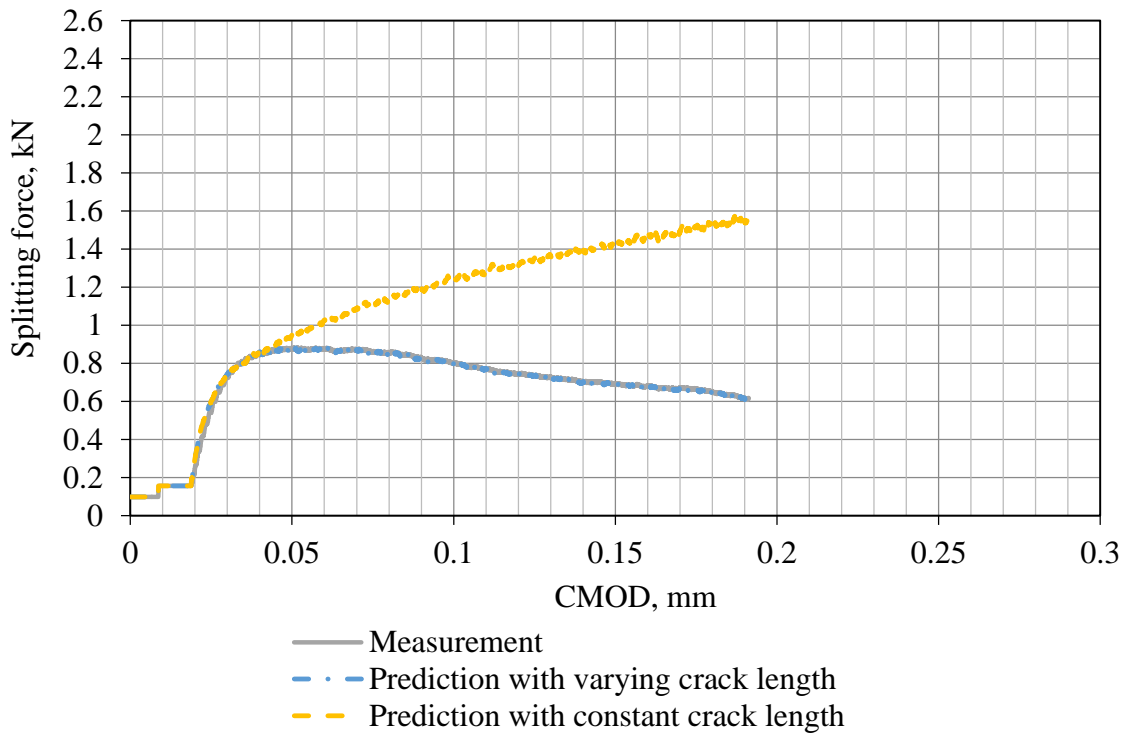
Figure C. 3. Measured and predicted load-CMOD curves for S-12.

127
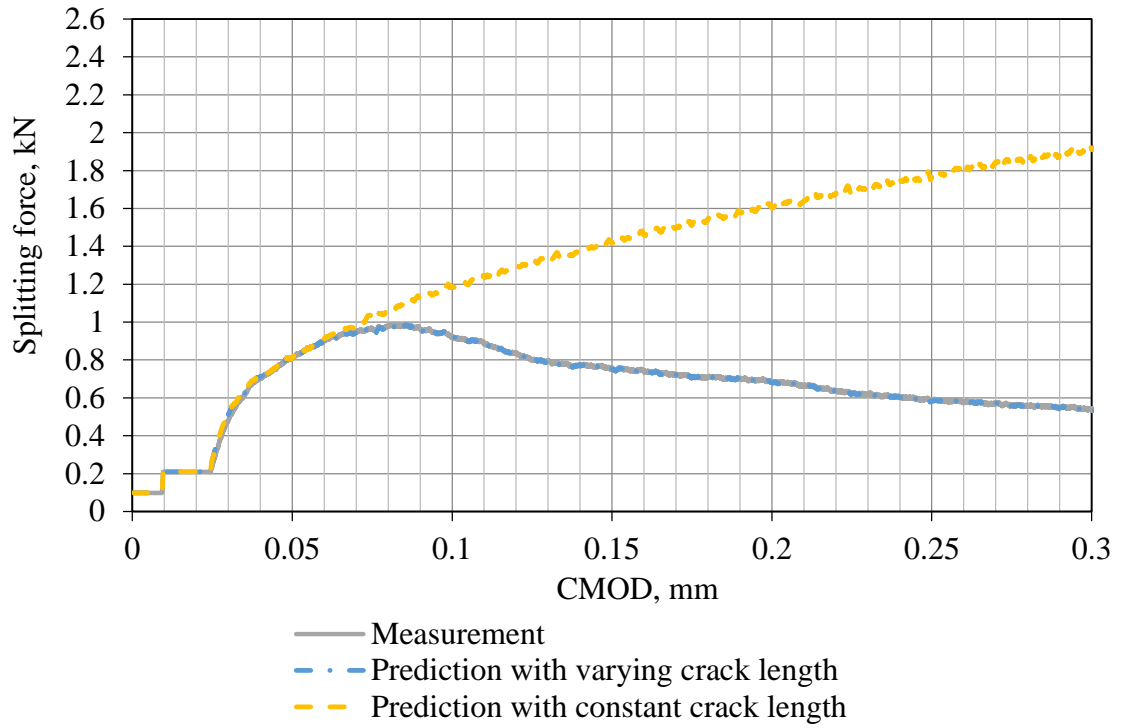
Figure C. 4. Measured and predicted load-CMOD curves for WST-S-14.

ANALYSIS OF WEDGE SPLITTING TEST UNDER DRY AND FREEZE CONDITIONS

Three milled (2-10, 2-11 and 2-14) and three unmilled (2-04 to 2-06) specimens were stored in a freezer before testing, where the temperature was monitored by three thermocouples embedded in a dummy WST. In Figure D. 1, it shows the temperature change recorded by the three thermocouples 1 through 3 that were 13 mm, 38 mm and 76 mm inside the dummy specimen, respectively.
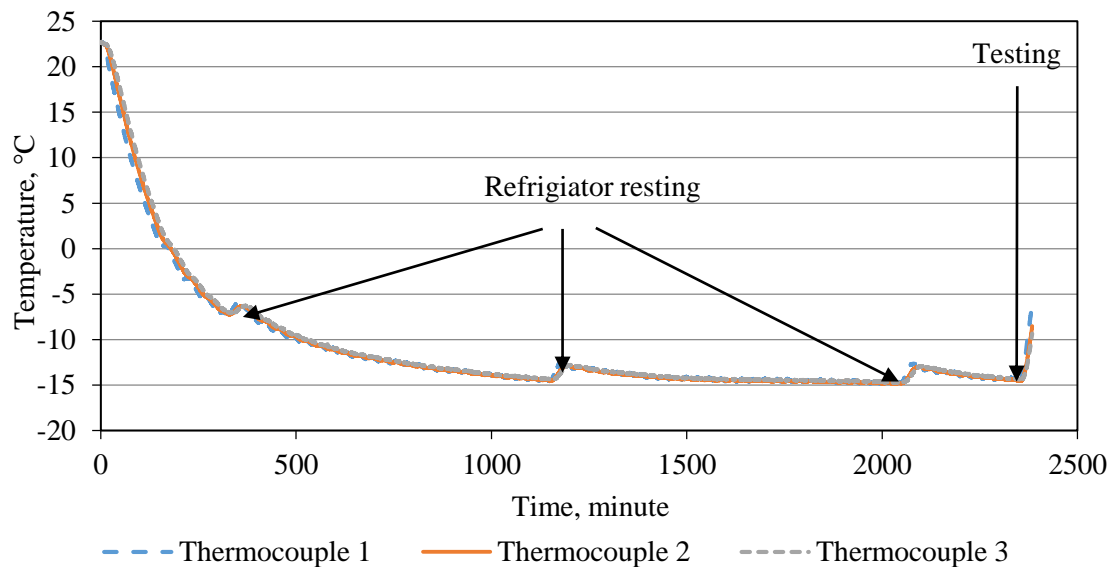
Figure D. 1. Change of temperature for the frozen specimens prior to testing.

The freezer storage of the specimens for 40 hours allowed the specimen to cool down to -15 °C. The loading of the specimens was conducted under room temperature, so the temperature began to rise as soon as testing began. As expected, the temperature at the edge rose slightly quicker than the inside. On average, the increase in the temperature is approximately 1 to 2 °C

during the testing period which is typically 10 minutes long, as shown in Figure D. 2. Therefore, it is fair to conclude the test was carried out at a low and relatively constant temperature.
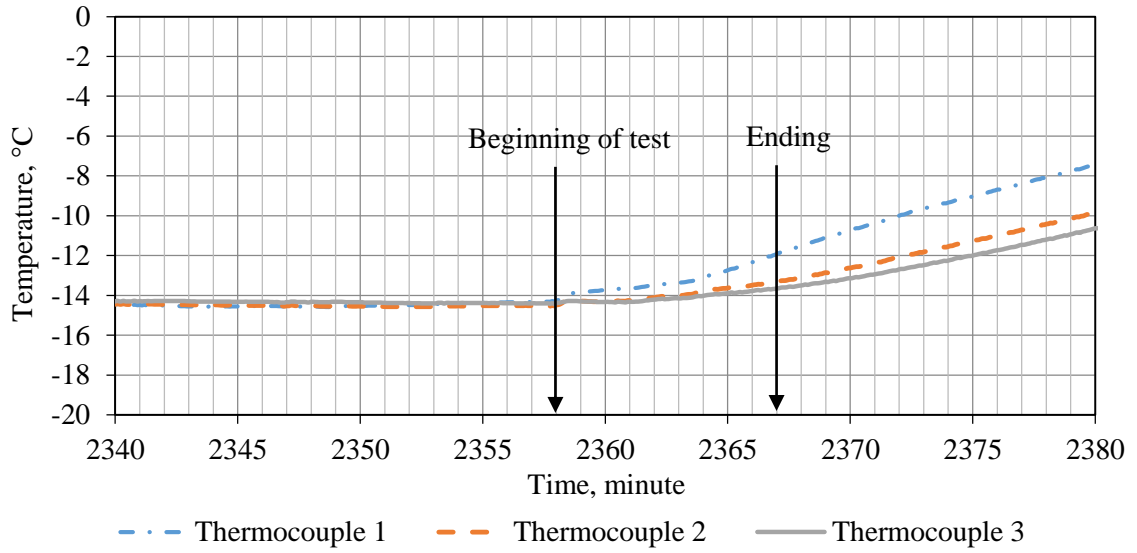
Figure D. 2. Change of temperature for the frozen specimens during testing.

The data for all the dry and frozen specimens were processed using the model presented in Section 2.4 and the results are presented in Figure D. 3 to Figure D. 8.
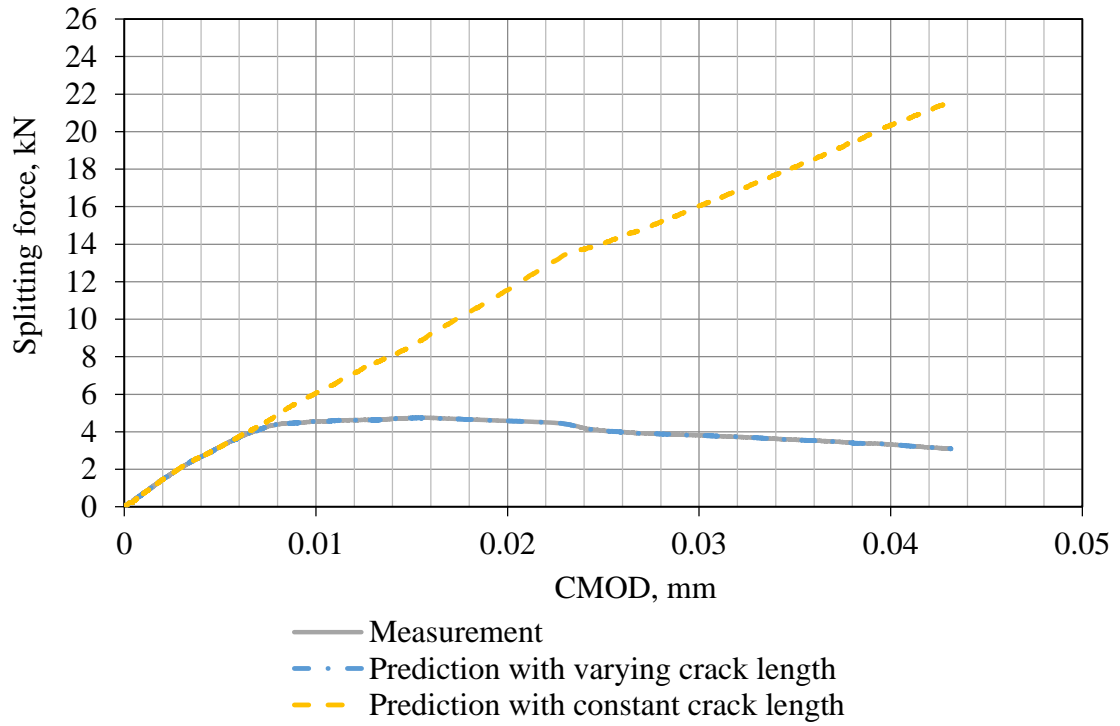
Figure D. 3. Measured and predicted load-CMOD curves for 2-10.
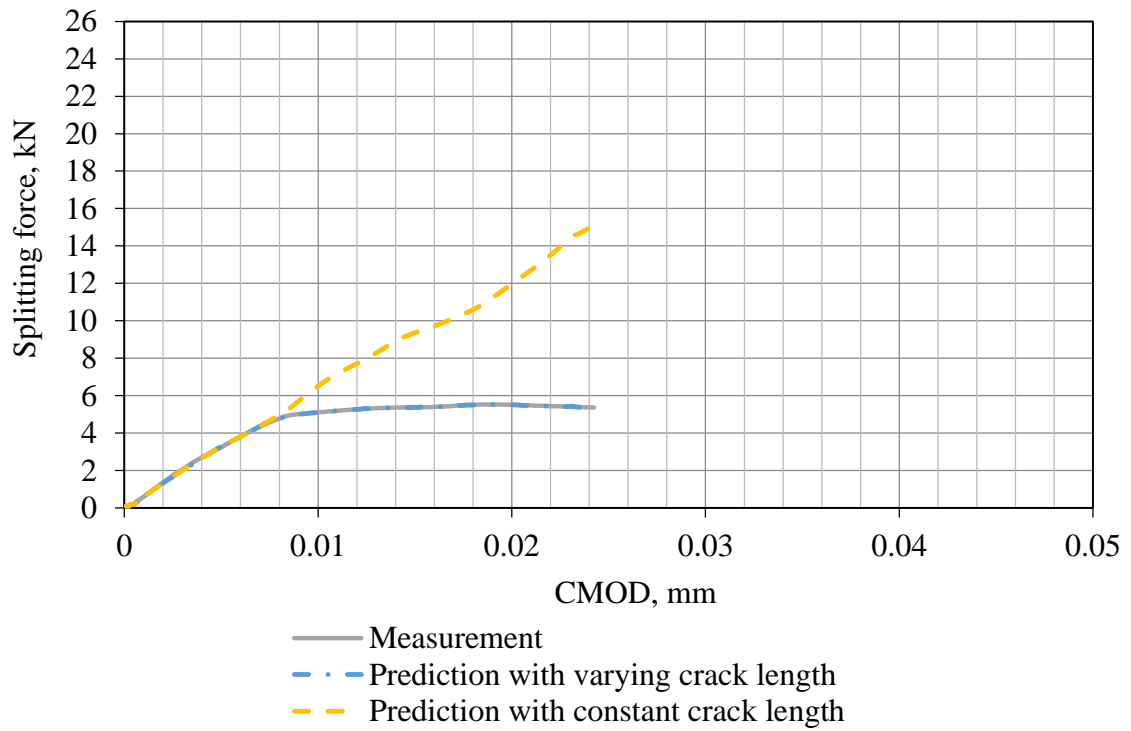
Figure D. 4. Measured and predicted load-CMOD curves for 2-11.
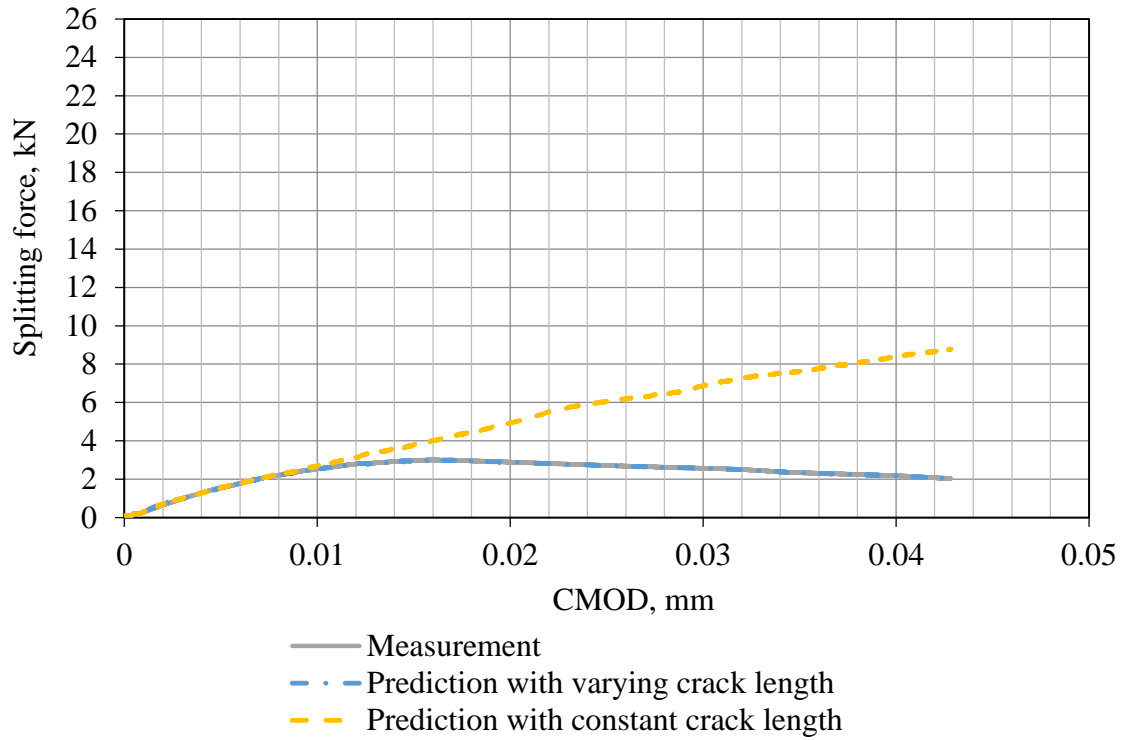
Figure D. 5. Measured and predicted load-CMOD curves for 2-14.
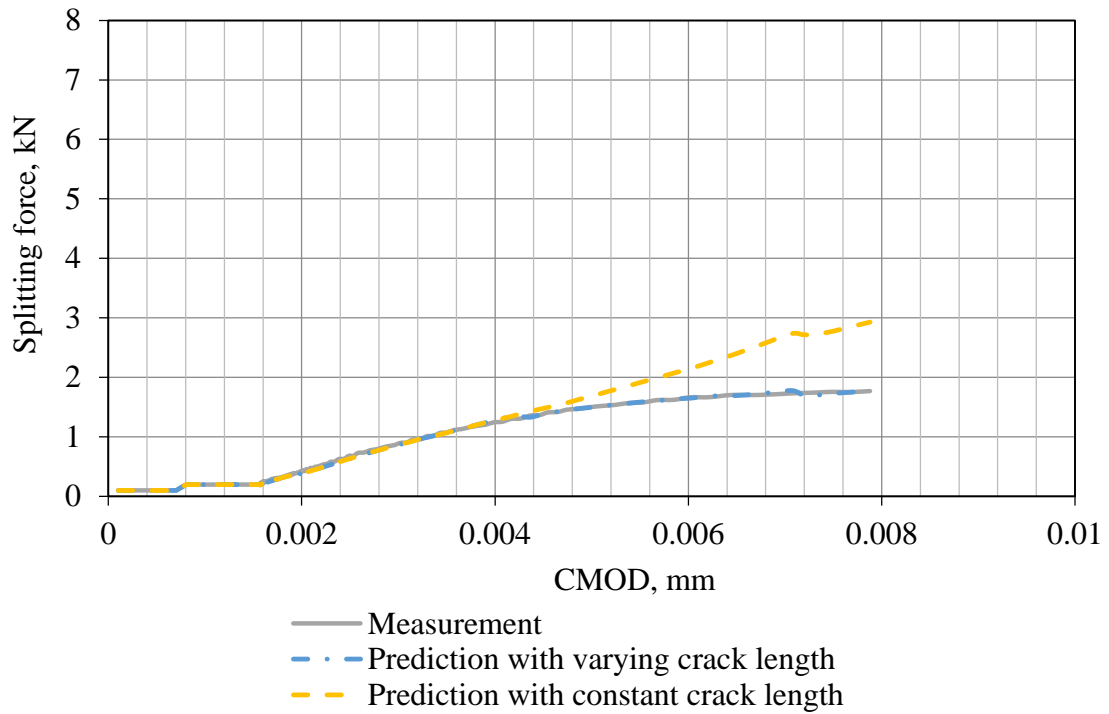
Figure D. 6. Measured and predicted load-CMOD curves for 2-04.
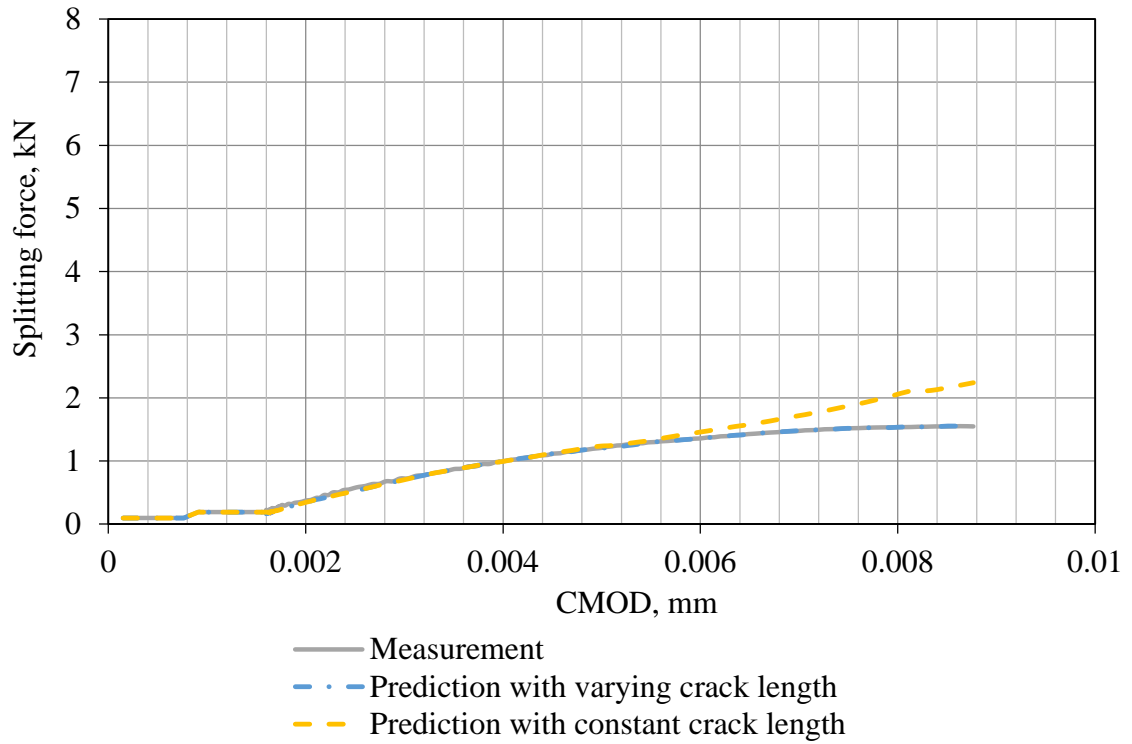
Figure D. 7. Measured and predicted load-CMOD curves for 2-05.
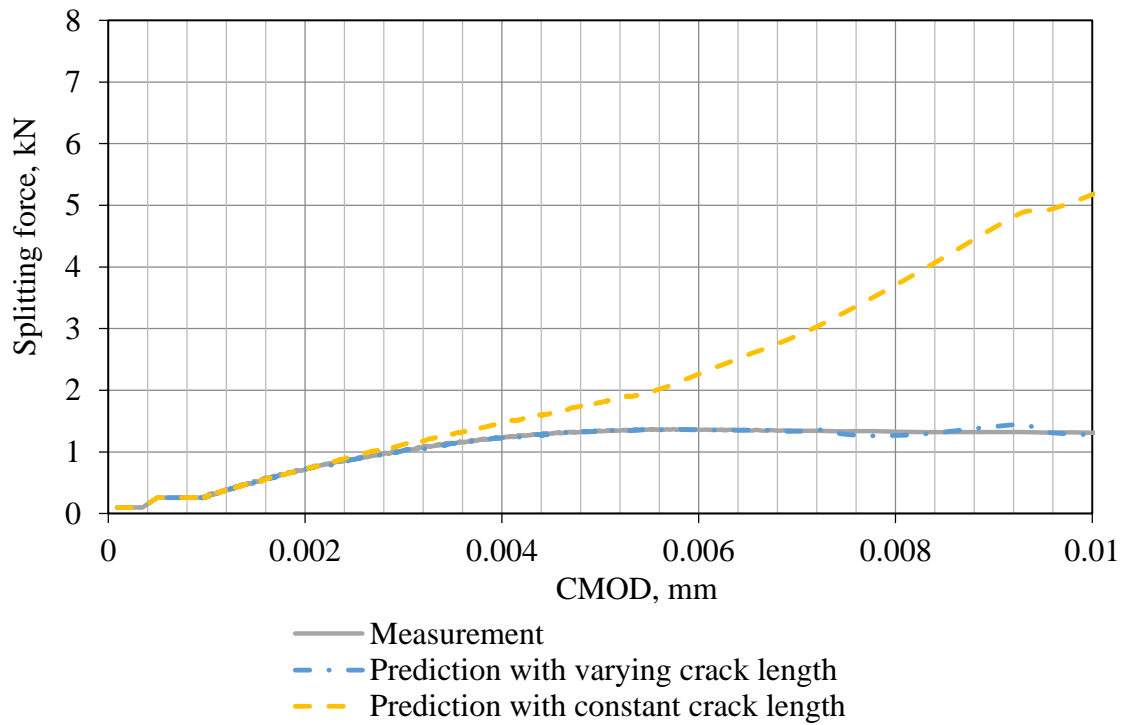
Figure D. 8. Measured and predicted load-CMOD curves for 2-06.

ENERGY RELEASE RATE FOR THE WST INTERFACE FRACTURE

The energy release rate was calculated for all the WST specimens using the model developed in Section 2.4 and the results are presented in Table E. 1.

Table E. 1. Energy release rate for all the WST specimens.

Specimen	Testing temperature, °C	Moisture condition	Roughness, mm	Initial notch depth, mm	Energy release rate, N·m/m^2
2-07	23	Dry	0.97	9.4	1647
2-08	23	Dry	1.73	9.7	1691
2-09	23	Dry	1.47	10.2	1780
2-12	23	Dry	1.73	16.5	2893
2-13	23	Dry	2.11	16.5	2893
2-15	23	Dry	2.01	11.4	2003
S-01	23	Dry	1.88	18.3	3204
2-01	23	Dry	0.48	13.7	2403
2-02	23	Dry	0.58	9.4	1647
2-03	23	Dry	0.56	9.7	1691
S-10	23	Dry	0.84	17.8	3115
S-11	23	Dry	0.79	11.7	2047
S-13	23	Dry	0.84	28.4	4984
S-15	23	Dry	0.76	42.7	7476
S-04	23	Wet	1.73	18.3	3204
S-12	23	Wet	0.89	13.7	2403
S-14	23	Wet	0.64	14.5	2537
2-10	-13	Dry	1.52	9.7	1691
2-11	-13	Dry	1.65	9.4	1647
2-14	-13	Dry	2.16	14.0	2448
2-04	-13	Dry	0.84	13.7	2403
2-05	-13	Dry	0.56	15.5	2715
2-06	-13	Dry	0.56	15.2	2670

It is not difficult to find that the energy release rate is highly correlated with the interface roughness as well as the initial notch depth, as demonstrated in Figure E. 1 and Figure E. 2. In these two figures, only specimens tested at 23 °C were included.
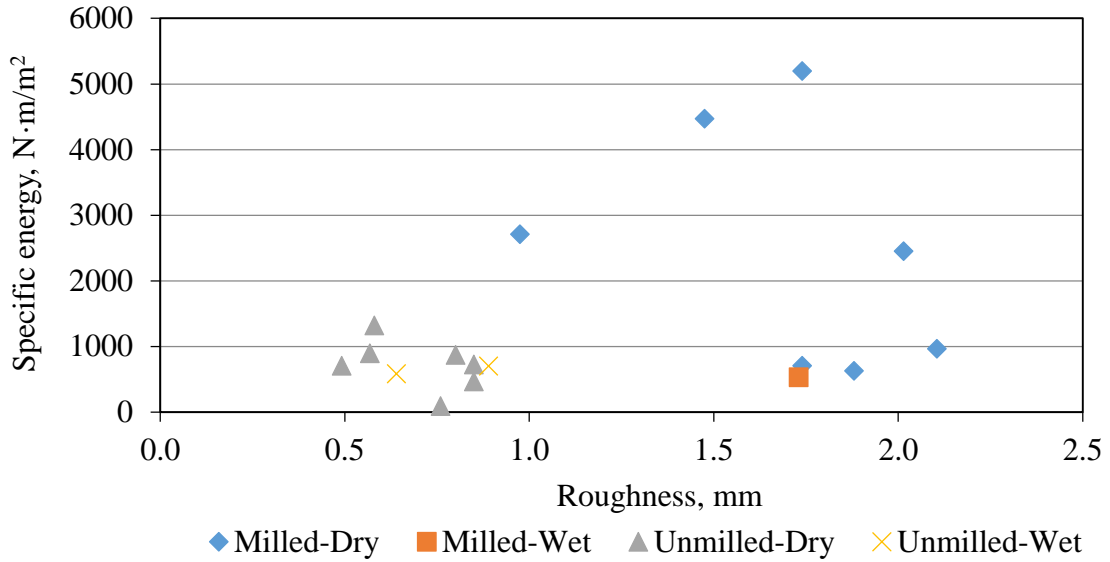
Figure E. 1. Energy release rate Vs. HMA surface roughness.
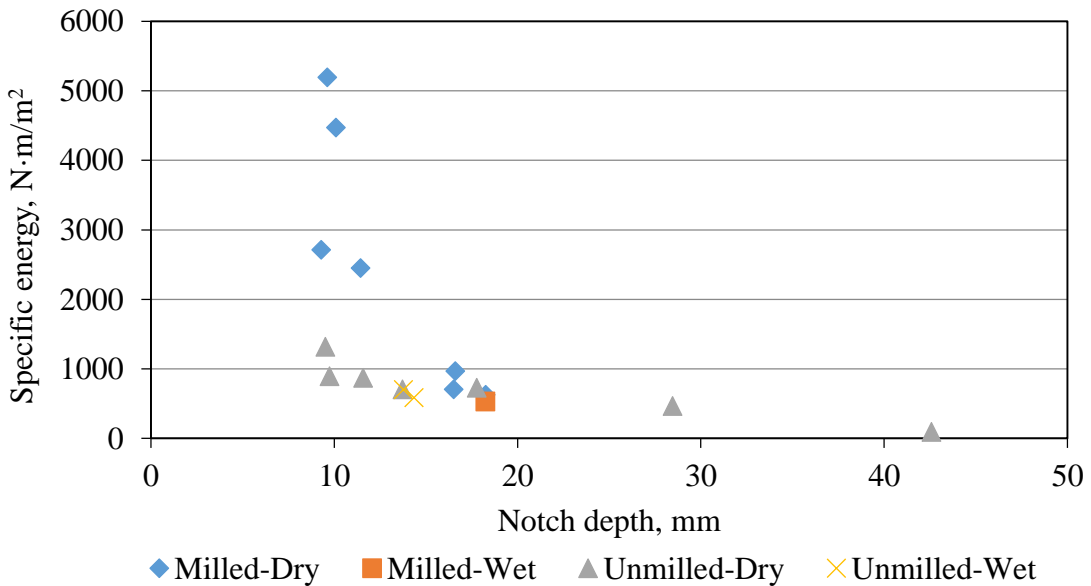
Figure E. 2. Energy release rate Vs. initial notch depth.

A statistical analysis was then carried out to yield the correlation between the energy release rate and the two parameters, represented by Equation (E.1).

$$Log(G)=B_0+B_1 \cdot log(R)+B_2 \cdot log(a_0) \qquad (E.1)$$

where G is the energy release rate, $N \cdot m/m^2$, R is the HMA surface roughness, mm, and a_0 is the initial notch depth, mm. The coefficients in Equation (E.1.) were computed based on the data in Table E.1 and the results are presented in Table E.2. The effect of moisture was not studied alone, because there was only three wet specimens tested. The calibration coefficients will vary when different subsets of specimens are used for the statistical analysis.

Table E. 2. Calibration Coefficients for Equation (E.1).

Set	Specimens used	B_0	B_1	B_2	R_{adj}^2
1	Milled-room temperature	-5.416	1.030	-3.420	0.95
2	Unmilled-room temperature	-3.242	0.914	-1.594	0.80
3	All frozen specimens	-5.172	0.736	-3.100	0.87

The energy release rate was predicted using Equation (E.1). Figure E. 3 compares the measured and predicted energy release rates. Based on the coefficients from Sets 1-3, the energy release rate for the specimens were computed and compared with the measurements, as shown in Figure E. 3. A good agreement can be seen.
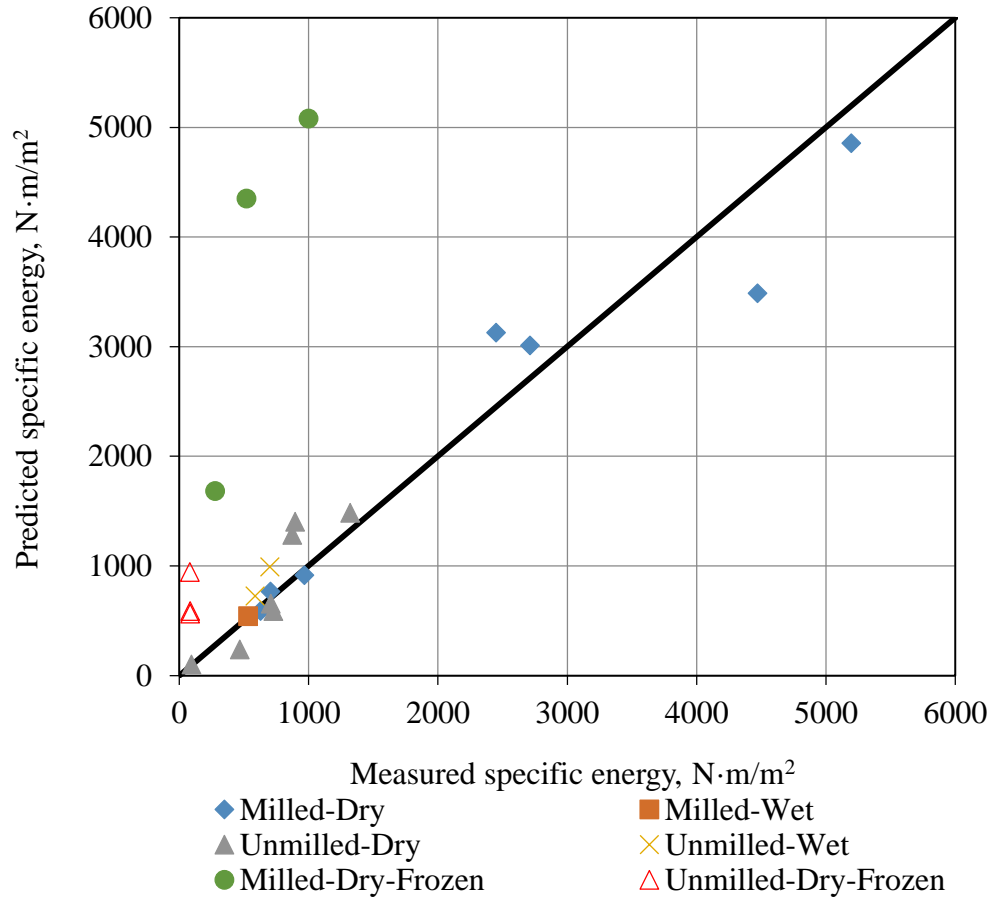
Figure E. 3. Comparison between measured and predicted energy release rate using

Equation (E.1) with coefficient of Sets 1-3 from Table E.2.

BIBLIOGRAPHY

AASHTO T 342-11. *Standard Method of Test for Determining Dynamic Modulus of Hot-Mix Asphalt Concrete Mixtures*.

ABAQUS (2011). *ABAQUS Theory Manual* (6.11).

ACPA American Concrete Pavement Association (2012). Retrieved September 17, 2012, from http://www.pavement.com/Concrete_Pavement/Technical/Fundamentals/Overlays_of_Asphalt_Pavement.asp

Aggelis, D.G. and Shiotani, T. (2007). Repair Evaluation of Concrete Cracks using Surface and Through-transmission Wave Measurements, *Cement and Concrete Composites*, Vol. 29, No. 9, pp700-711.

Alfano, M., Furgiuele, F., Leonardi, A., Maletta, C., and Paulino, G. H. (2007). Cohesive zone modeling of mode I fracture in adhesive bonded joints. *Key Engineering Materials*, No. 348-349, pg. 13-16.

Alfano, M., F. Furgiuele, Leonardi, A., Maletta, C. and Paulino, G. H. (2009). Mode I fracture of adhesive joints using tailored cohesive zone models. *International Journal of Fracture*, Vol. 157, No. 1-2, pg.193-204.

Al-Hunaidi, M. O. (1996). Nondestructive Evaluation of Pavements using Spectral Analysis of Surface Waves in the Frequency Wave-Number Domain, *Journal of Nondestructive Evaluation*, Vol. 15, No. 2, pp71-82.

Al-Qadi, I. L., Carpenter, S. H., Leng, Z, Ozer, H. and Trepanier, J. S. (2008). *Tack Coat Optimization for HMA Overlays: Laboratory Testing*. Research Report FHWA-ICT-08-023, Illinois Center for Transportation.

Alleyne, D. N. and Cawley, P. (1992). The Interaction of Lamb Waves with Defects, *Ultrasonics, Ferroelectrics and Frequency Control, IEEE Transactions on*, Vol.39, No.3, pp381-397.

ASTM C469. *Standard Test Method for Static Modulus of Elasticity and Poisson's Ratio of Concrete in Compression*. Retrieved from www.astm.org, 2012.

ASTM D1195/D1195M-09. *Standard Test Method for Repetitive Static Plate Load Tests of Soils and Flexible Pavement Components, for Use in Evaluation and Design of Airport and Highway Pavements*. Retrieved from www.astm.org, 2009

ASTM-E965-96. *Standard Test Method for Measuring Pavement Macrotexture Depth Using a Volumetric Technique*. Retrieved from www.astm.org, 2012.

Bazant, Z.P. and Becq-Giraudon E. (2002). Statistical prediction of fracture parameters of concrete and implications for choice of testing standard, *Cement and Concrete Research*, Vol. 32, pg. 529-556.

Bouden, T., Djerfi, F., Dib, S. and Nibouche, M. (2012). Hilbert Huang Transform for Enchancing the Impact Echo Method of Non Destructive Testing. *Journal of Automation and Systems Engineering*, Vol. 6, No. 4, pp172-184.

Brühwiler, E. and Wittmann, F. H. (1990). The wedge splitting test, a new method of performing stable fracture mechanics tests. *Engineering Fracture Mechanics*, Vol. 35, No. 1-3, pg. 117-125.

Carino, N. J. (2001). The impact-echo method: an overview. *Proceedings of the 2001 Structures Congress & Exposition*, American Society of Civil Engineers, Washington, D.C.

Chabot, A., Balay, J.M., Pouteau, B. and De Larrard, F. (2008). FABAC accelerated loading test of bond between cement overlay and asphalt layers. *Pavement Cracking* − Al-Qadi, Scarpas & Loizos (eds).

Cheng, C., and Sansalone, M. (1993). The Impact-echo Response of Concrete Plates Containing Delaminations-Numerical, Experimental and Field Studies. *RILEM Journal. Materials and Structures*, Vol. 26, pp.274–285.

Cole, L.W. and Mohsen, J.P.(1993). Ultrathin Overlays on Asphalt. Presented at the TAC Annual Conference, Ottawa, ON, Canada.

Cole, L.W., Mack, J. W. and Packard, R. G. (1998). Whitetopping and ultra-thin whitetopping the US experience. 8th International Symposium on Concrete Roads, 1998.

Delatte, N. and Sehdev, A. (2003). Mechanical properties and durability of BCO and UTW concrete, Paper presented for the 82th TRB annual meeting Washington D.C., January, 2003.

Feraren, P. and Jensen, H. M. (2004). Cohesive zone modeling of interface fracture near flaws in adhesive joints. *Engineering Fracture Mechanics*, Vol. 71, No., 15, pg. 2125-2142.

Gibson, A. and Popovics, J. (2005). Lamb Wave Basis for Impact-Echo Method Analysis, *Journal of Engineering Mechanics*, Vol. 131, No. 4, pp438-443.

Grove, J. D., Engle, E. J., and Skinner, B. J. (1996). *Bond Enhancement Techniques for PCC Whitetopping*. Final Report for Iowa Highway Research Board Project HR-341, page16-20.

Gucunski, N. (1998). *Development of a Design Guide for Ultra Thin Whitetopping (UTW)*. FHWA report 2001-018.

Guinea, G.V., Planas, J. and Elices, M. (1994). A general bilinear fitting for the softening curve of concrete. *Materials and Structures*, Vol. 27, pg. 99–105.

Guo, N. and Cawley, P. (1993). The Interaction of Lamb Waves with Delaminations in Composite Laminates, *Journal of the Acoustic Society of America*, Vol. 94, pp2240-2246

Heitzman, M., Maser, K, Tran, N. H. Brown, Bell, R. H., Holland, S., Ceylan, H., Belli, K. and Hiltunen, D. (2013). *Nondestructive Testing to Identify Delaminations between HMA Layers, Volume 3: Controlled Evaluation Reports.* Transportation Research Board's second Strategic Highway Research Program: Report S2-R06D-RR-1, Washington, D.C.

Hillerborg, A., Modeer, M., and Petersson, P. E., (1976). Analysis of crack formation and crack growth in concrete by means of fracture mechanics and finite elements. *Cement and. Concrete. Research*, Vol. 6, No. 6, pg. 773–781.

Hurlebaus, S., Niethammer, M., Jacobs, L. J. and Valle, C. (2001). Automated Methodology to Locate Notches with Lamb Waves. *Acoustics Research Letters Online*, Vol. 2, pp97-102.

In, Chi-Won (2013). *Defect Characterization in Heterogeneous Civil Materials Using Ultrasound*. PhD dissertation, Georgia Institute of Technology.

Kim, H., Wagoner, M. P., and Buttlar, W. G. (2008). Simulation of fracture behavior in asphalt concrete using a heterogeneous cohesive zone discrete element model. *Journal of Materials in Civil Engineering*, Vol. 20, No. 8, pg. 552-563.

Koh, Y.L, Chiu, W.K and Rajic, N. (2002). Effects of Local Stiffness Changes and Delamination on Lamb Wave Transmission using Surface-mounted Piezoelectric Transducers, *Composite Structures*, Vol. 57, No. 1–4, pp 437-443.

Kohl, C., Krause, M., Maierhofer, C., and Wöstmann, J. (2005). 2D- and 3D-visualisation of NDT-data using data fusion technique. Journal of Materials and Structures, Vol. 38, No. 38, pp 817-826.

Lehmann, E. L. (1986). *Testing Statistical Hypothesis*. 2nd edition. New York: Wiley.

Li, Z. and Vandenbossche, J.M. (2013). Redefining the Failure Mode for Thin and Ultra-thin Whitetopping with a 1.8-x1.8-m (6-x6-ft) Joint Spacing. Proceedings of 92nd Transportation Research Board Meeting, Washington, D.C.

Li, S., Thouless, M. D., Waas, A.M., Schroeder, J.A., and Zavattieri, P.D. (2005). Use of mode-I cohesive-zone models to describe the fracture of an adhesively-bonded polymer-matrix composite. *Composites Science and Technology*, Vol. 65, No. 2, pg. 281-293.

Lin, Y., Sansalone, M. and Carino, N. J. (1990). Finite Element Studies of the Impact-echo Response of Plates containing Thin Layers and Voids, *Journal of Nondestructive Evaluation*, Vol. 9, No. 1, pp27-47.

Maierhofer, C. (2003). Nondestructive Evaluation of Concrete Infrastructure with Ground Penetrating Radar. *Journal of Materials in Civil Engineering,* Vol. 15, No. 3, pg. 287–297.

MATLAB and Statistics Toolbox Release 2013a, The MathWorks, Inc., Natick, Massachusetts, United States.

Medina, R. and Garrido, M. (2007). Improving impact-echo method by using cross-spectral density, *Journal of Sound and Vibration*, Vol. 304, No. 3–5, pp 769-778.

Mohammed, I. and K. M. Liechti (2000). Cohesive zone modeling of crack nucleation at bimaterial corners. *Journal of the Mechanics and Physics of Solids*, Vol. 48, No.4, pg. 735-764.

Mu, F. and Vandenbossche, J.M. (2011) Temperature Effects on Overlay Bond Characteristics and the Overlay Response to Dynamic Loads for Bonded PCC Overlays Placed on Asphalt Pavements, 7th International DUT-Workshop on Design and Performance of Sustainable and Durable Concrete Pavements, Spain.

Mu, F., Vandenbossche, J.M. and Janssen, D. J. (2013). Quantifying the node I energy release rate for interface fracture of Portland cement concrete bonded to asphalt. American Concrete Institute Spring Convention, 2013.

Munoz, D. 2009. *Finite Element Modeling of Nondestructive Test Methods Used for Detection of Delamination in Hot Mix Asphalt Pavements*. MS thesis, University of Texas at El Paso.

Nelson, P. K. and Rasmussen, R. O. (2002). Delamination stresses at the interface of bonded concrete overlays. Proceedings of 81st Transportation Research Board Meeting, Washington, D.C.

Ng, C. T. and Veidt, M. (2011). Scattering of the Fundamental Anti-symmetric Lamb Wave at Delaminations in Composite Laminates, *Journal of the Acoustic Society of America*, Vol. 129, No.3, pp1288-1296.

Park, K., Paulino, G. H., and Roesler, J. (2010). Cohesive fracture model for functionally graded fiber reinforced concrete. *Cement and Concrete Research*, Vol. 40, No. 6, pg. 956-965.

Penny W. D. (2009). *Signal Processing Course, chapter 7*. University College London. http://www.fil.ion.ucl.ac.uk/~wpenny/course/course.html

Pouteau, B., Balay, J.M., Chabot, A. and De-Larard, F. (2004). Faitue test and mechanical study of adhesion between concrete and asphalt. 9th International Symposium on Concrete Road, Istanbul, April 2004.

Rasmussen, R.O. and Rozycki, D.K. (2004). *Thin and Untra-Thin Whitetopping, NCHRP Synthesis of Highway Practice 338*, National Cooperative Highway Research Program, National Research Council, Washington, D.C, 2004.

Rose, J. L., Pilarski, A., and Huang, Y. (1990). Surface Wave Utility in Composite Material Characterization, *Research in Nondestructive Evaluation*, Vol. 1, No. 4, pp247-265

Roesler, J., Bordelon, A., Ioannides, A., Beyer, M. and Wang, D. (2008). *Design and Concrete Material Requirements for Ultra-Thin Whitetopping*. Report ICT-08-016. Illinois Center for Transportation.

Sansalone, M. and Carino, N. J. (1989). Detecting Delaminations in Concrete Slabs with and without Overlays using the Impact-echo Method. *ACI Materials Journal*, V.86, No. 2, pp175-184.

Schubert, F. and Köhler, B. (2008). Ten Lectures on Impact-Echo. *Journal of Nondestructive Evaluation*, Vol. 27, No. 1-3, pp5-21.

Song, S. H., Paulino, G. H., and Buttlar, W. G. (2008). Influence of the cohesive zone model shape parameter on asphalt concrete fracture behavior. AIP Conference.

Su, Z., Ye, L., and Lu, Y. (2006). Guided Lamb Waves for Identification of Damage in Composite Structures: A review, *Journal of Sound and Vibration*, Vol. 295, No. 3–5, pp753-780.

Tarr, S. M., M. Sheehan and P. A. Okamoto. (1998). *Guidelines for the Thickness Design of Bonded Whitetopping Pavement in the State of Colorado*. Report No. CDOT-DTD-R-98-10. Colorado Department of Transportation, Denver, CO.

Tschegg, E., Rotter, H., Roelfstra, P., Bourgund, U., and Jussel, P. (1995). Fracture-mechanical behavior of aggregate-cement matrix interfaces. *Journal of Materials in Civil Engineering*, Vol. 7, No. 4, pg. 199-203.

Tschegg, E. K., Jamek, M. and Lugmayr, R. (2011). Fatigue crack growth in asphalt and asphalt-interfaces. *Engineering Fracture Mechanics*, Vo.78, No. 6, pg. 1044-1054.

Tvergaard, V. and Hutchinson J. W. (1992). The relation between crack-growth resistance and fracture process parameters in elastic plastic solids. *Journal of the Mechanics and Physics of Solids*, Vol. 40, No. 6, pg. 1377-1397.

Ural, A., Krishnan, V. R. and Papoulia (2009). A cohesive zone model for fatigue crack growth allowing for crack retardation, *International Journal of Solids and Structures*, Vol. 46, No. 11-12, pg. 2453-2462.

Vandenbossche, J. M. and Fagerness, A. J. (2002). Performance, analysis, and repair of ultrathin and thin whitetopping at Minnesota road research facility. *Transportation Research Record, Journal of Transportation Research Board, National Research Council*, Washington, DC. Vol.1809, pg. 191–198.

Vandenbossche, J. M. (2005). Best practices for the design and repair of thin and ultra-thin whitetopping based on Mn/ROAD findings. International Conference on Best Practices for Ultrathin and Thin Whitetoppings Proceedings, Denver, CO.

Walter, R., Østergaard, L., Olesen, J. F., and Stang, H. (2005). Wedge splitting test for a steel-concrete interface. *Engineering Fracture Mechanics*, Vol. 72, No. 17, pg. 2565-2583.

Wu, C. L, S. M. Tarr, T. M. Refai, M. A. Nagi and M. J. Sheehan. (1999). *Development of Ultra-Thin Whitetopping Design Procedure.* PCA Research and Development, Serial No. 2124, Portland Cement Association, Skokie, IL.

Xie; Z., Zhang; Y. and Wu, H.F. (2012). Automated Data Fusion and Visualization for Impact-Echo Testing of Concrete Structures, *Sensors Journal, IEEE*, Vol.12, No.12, pp3446-3453.

Yeh, P. and Liu, P. (2008). Application of the Wavelet Transform and the Enhanced Fourier Spectrum in the Impact Echo Test, *NDT & E International*, Vol. 41, No. 5, pp. 382-394.

Zhang, Y., Wei, X. Tsai, Y., Zhu, J., Fetrat, F. A. and Gucunski, N. (2012). Multisensor Data Fusion for Impact-echo Testing of Concrete Structures, *Smart Materials and Structures*, Vol. 21, No. 7.

Zhu, J. and Popovics, J. (2007). Imaging Concrete Structures Using Air-Coupled Impact-Echo, *Journal of Engineering Mechanics*, Vol. 33, No. 6, pp. 628-640.